1-1-2011

Single Vibration Mode Standing Wave Tubular Piezoelectric Ultrasonic Motor

Soonho Park
Ryerson University

Single Vibration Mode Standing Wave Tubular Piezoelectric Ultrasonic Motor

by

Soonho Park

Bachelor of Engineering, Ryerson University, 2009

A thesis

presented to Ryerson University

in partial fulfillment of the

requirements for the degree of

Master of Applied Science

in the program of

Mechanical Engineering

Toronto, Ontario, Canada, 2011

Author’s declaration

I hereby declare that I am the sole author of this thesis.

I authorize Ryerson University to lend this thesis or dissertation to other institutions or individuals for the purpose of scholarly research.

_____

Soonho Park

I further authorize Ryerson University to reproduce this thesis by photocopying or by other means, in total or in part, at the request of other institutions or individuals for the purpose of scholarly research.

_____

Soonho Park

Abstract

SINGLE VIBRATION MODE STANDING WAVE TUBULAR PIEZOELECTRIC ULTRASONIC MOTOR

Soonho Park, Master of Applied Science, Mechanical Engineering, Ryerson University, 2011

The objective of this thesis is to report the single vibration mode standing wave tubular piezoelectric ultrasonic motors developed. Piezoelectric motors are driven by reverse piezoelectric effects which converts an input of ultrasonic frequency of electrical energy into an output of mechanical movement. There are many advantages of piezoelectric ultrasonic motors compared to electromagnetic motors such as simple structure, high energy density, and high torque at low speed. Three prototypes are designed and fabricated. Two motors are fabricated using PZT cylindrical tube; one with PZT teeth and the other with metal teeth. A third motor using brass tube with PZT plates attached is fabricated. After design and fabrication of three prototypes, the performances of the motors are tested using a test apparatus for speed and torque.

Acknowledgements

I would like to thank:

- God for always giving me wisdom and courage
- Dr. Siyuan He, my supervisor, for his insight and guidance for this project
- Devin Ostrom and Joseph Amankrah, technical officers at Ryerson University, for fabricating parts for prototypes and test apparatus
- Dr. Y. Chen and Dr. S. Ghinet from NRC for their help with the frequency response measurements
- Paul Chiarot, Postdoctoral Researcher, for a collaborated work to publish a paper in IEEE Ultrasonics, Ferroelectrics, and Frequency Control
- James Chong, Naser Haghbin, Zewdu Hailu, Terry Xue, and Fan Chao for being great friends at Ryerson University during graduate school
- Anthony Chiu, John Chang, and Wen Li for setting examples for being successful graduate students a year ahead
- Eunkyung Choi, my fiancé, for love and support throughout my school years
- My family for encouragements and support

Table of Contents

List of Figures

List of Tables

Nomenclature

{T}	Stress matrix
{S}	Strain matrix
{D}	Electric field constant
{E}	Electric charge density displacement
$[S^E]$	Elastic compliance
[d]	Direct piezoelectric strain coefficient
$[d^t]$	Reverse piezoelectric strain coefficient
$[\varepsilon^T]$	Dielectric permittivity
w	Displacement in the radial direction (m)
E	Young's modulus (GPA)
G	Transverse modulus (GPA)
ρ	Density (kg/m3)
I	Polar moment of inertia of area (m4)
A	Cross sectional area (m2)
L	Length of the stator (m)
κ	Adjustment coefficient for Timoshenko beam theory
C_i	Constants
α_i	Frequency parameters
ω_i	Natural vibration frequencies (rad/s)
W_i	Mode shapes (m)
ω_1	Fundamental resonance frequencies (rad/s)
W_1	Bending mode shapes (m)
u	Axial displacement of the stator (m)
r	Arbitrary distance in radial direction (m)
R_r	Radius of the rotor (m)
f_1	Resonance Frequency (Hz)
s_e	Strain induced by external force
s_p	Strain induced by electric field

E_r	Electric field (V/m)
V	Voltage Applied (V)
r	Radial distance from the centre of the tube (m)
α	Aspect ratio
t	Thickness of the tube (m)
R_o	Outer radius of the tube (m)
R_i	Inner radius of the tube (m)
S_1	Axial components of strain
T_1	Axial components of stress (MPa)
a	Radius of curvature of the axis of the tube in xz plane
b	Radius of curvature of the axis of the tube in yz plane
c	Strain in axial direction
V_x	Voltage applied on the two quadrants in the x direction (V)
V_y	Voltage applied on the two quadrants in the y direction (V)
V_z	Voltage applied on the inner electrode (V)
d_{31}	Piezoelectric strain/charge constant (v/m)
d_{33}	Piezoelectric strain/charge constant (v/m)
k_{31}	Piezoelectric Coupling Factor
k_{33}	Piezoelectric Coupling Factor
S^E_{11}	Compliance Elastic Modulus (m2 /N)
S^E_{33}	Compliance Elastic Modulus (m2 /N)
ρ	Density (kg/m3)
Y	Yield Strength (MPa)
ν	Poisson's ratio

Chapter 1. Introduction

1.1 Piezoelectricity

The term piezoelectricity comes from Greek reference meaning electricity by pressure. This phenomenon is first discovered by the brothers of J. Curie and P. Curie in 1880 [1]. When piezoelectric crystals are polarized, positive and negative charges appear on the surfaces of the polarized crystals as they are compressed. When pressure is applied on the piezoelectric materials, a charge density appears on the surface which generates an electric field. This leads to a flow of free charges. The generation of an electric field under stress is called direct piezoelectric effect while reverse piezoelectric effect refers to deformation of piezoelectric materials under application of an electric field. Figure 1.1 shows the direct and reverse piezoelectric effects.

Some of the natural materials that exhibit piezoelectric effect are quarts, tourmaline, and Rochelle salt. However, the piezoelectric effect in those natural materials is very small in magnitude and improved properties in polycrystalline ferroelectric ceramic materials such as barium titanate and lead zirconate titanate (PZT) have been developed [3]. Among the developed materials, PZT is the most widely used materials for actuator applications.

There are two piezoelectric equations that express the characteristics of piezoelectric ceramics [4]. The relationship between stress and strain, T and S, can be expressed in the first equation and the relationship between the constant electric field and electric charge density

displacement, E and D, can be expressed in the second equation. Variable s^E is the elastic compliance at constant electric field, d and d^t are the piezoelectric strain coefficients for direct and reverse effects, and ε^T is the dielectric permittivity.

$$\{S\} = [S^E]\{T\} + [d^t]\{E\} \tag{1.1}$$

$$\{D\} = [d]\{T\} + [\varepsilon^T]\{E\} \tag{1.2}$$

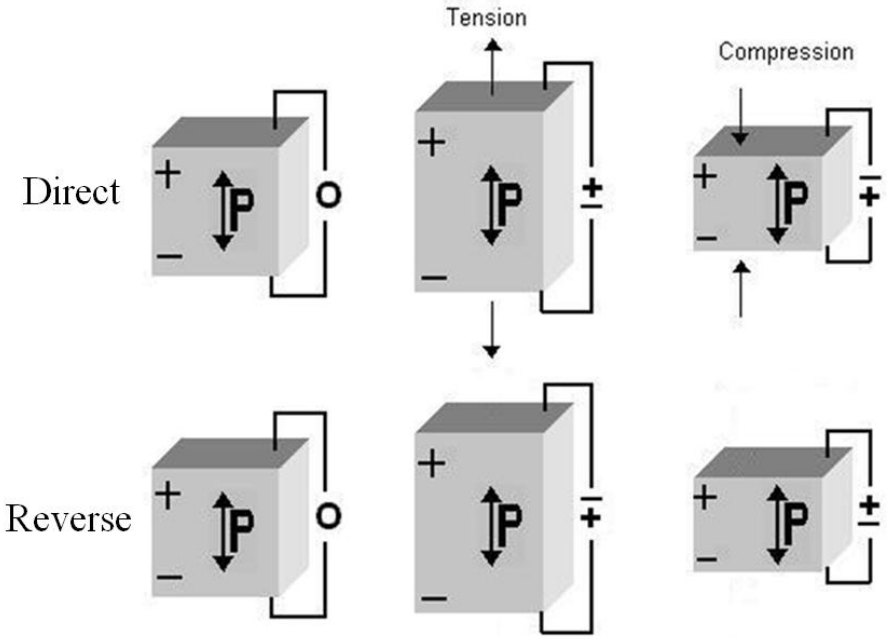

Figure 1.1 - Direct and reverse piezoelectric effect [2].

1.2 Background history of ultrasonic motors

An ultrasonic motor uses mechanical vibration in the ultrasonic range as its driving source for actuation [5]. Vibrations in the range of frequencies above 20 kHz are called the ultrasonic range vibration. This range is higher than the sound wave range that human ears can detect. When an electric field at a frequency in ultrasonic range is applied onto the piezoelectric

ceramics as the mechanical vibration source, the piezoelectric ceramics can either expand or contract according to the direction of electric field and poling direction of the piezoelectric material. While the amplitude of the vibration is in the order of micrometers, utilizing resonance effect to amplify the vibration amplitude can lead to a motor movement. Especially when the vibration frequency is in ultrasonic range, high speed of movement is possible due to the high frequency.

The first ultrasonic motor using piezoelectric materials is designed in 1948 by A. L. W. Williams et al. [6]. He has received patents on various piezoelectric motor designs for converting poly-phase electric potentials to mechanical movement using piezoelectric phenomena. One of the designs from his patent is a rod type piezoelectric ultrasonic motor with a cylindrical rod of piezoelectric crystal which is cut into three sections with individual electrodes on curved outer surfaces, as shown in Figure 1.2. The three sections of piezoelectric ceramic expand or contract in longitudinal direction depending on the electric potential applied while common central electrode is grounded. With one end of the motor fixed, the free end gyrates in a circular path in a plane normal to the longitudinal direction. The free gyrating end is capped with a shaft and a gear set to convert the gyrating movement into a rotation of the shaft.

Since 1969, Soviet Union also has started research in the field of ultrasonic motors in the Research Center ‘Vibrotechnika’ at Leningrad Politechnical Institute, Russia, Kaunas University of Technology, Lithuania, and Kiev Politechnical Institute, Ukraine [7]. In 1973, they have developed a bimodal mode coupled reversible ultrasonic motor. V. V. Lavrinenko from Kiev Politechnical Institute and A. A. Yerofeev from Leningrad Politechnical Institute has worked on developing rotary ultrasonic motors and their applications for automation.

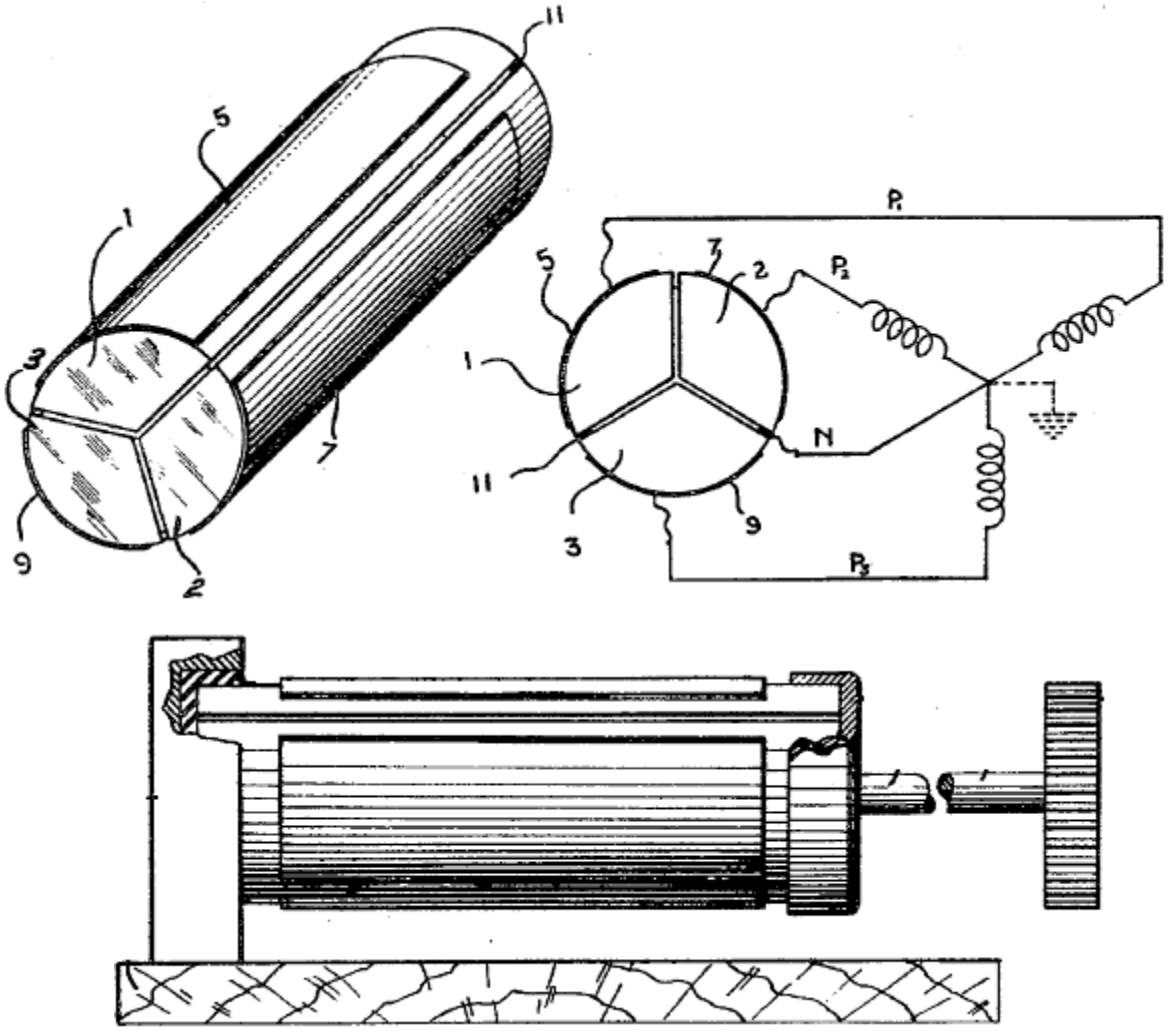

Figure 1.2 - Piezoelectric motor design by A. L. W. Williams et al. in 1948 [6].

H. V. Barth of IBM has proposed an ultrasonic motor in 1973 [8]. This motor design consists of a horn design pressed unto a rotor. The piezoelectric element is used to vibrate the horn which is in contact with the rotor. The movement of the rotor is generated by the friction between the vibrating horn and the rotor. There are two vibrators for each horn for controlling the rotation direction of the rotor which can rotate in clockwise direction when the

vibrator on the left is used. It rotates in counter-clockwise rotation when the vibrator on the right is used. The ultrasonic motor design is shown in Figure 1.3.

T. Sashida has designed a 'woodpecker' type ultrasonic motor in 1982 [9]. This piezoelectric motor is one of the first standing-wave type motor designed. The tip portion which is connected to a piezoelectric driver generates a flat elliptical movement. The simplified motor design is shown in Figure 1.4. The operating frequency of this motor is 27.8 kHz and it generates a torque of 0.25 Nm with a mechanical power output of 50 W when an electrical power input of 90 W is applied [8].

In 1983, T. Sashida has designed a ring type piezoelectric ultrasonic motor [10]. This is one of the first travelling-wave type motor designed. An elastic body bonded onto a thin piezoelectric ring is put in contact with a ring type slider. The PZT material is used for the piezoelectric ring which is divided into 16 poled regions with positive and negative poling directions. A prototype of an outer diameter of 60 mm, an inner diameter of 45 mm, and thickness of 2.5 mm brass ring bonded to a thickness of 0.5 mm PZT ring is designed. The working frequency of this motor is 44 kHz. The structure of Sashida's motor is shown in Figure 1.5.

S. Ueha has designed a rotary ultrasonic motor in 1988 employing two piezoelectric elements in the stator [11, 12]. The motor design consists of a torsional vibrator and three multi-layered piezoelectric actuators. Utilizing the frictional force, the torsional vibrator moves the rotor while the multi-layered piezoelectric actuators control the frictional force. By controlling

the frictional force of the three actuators, the speed of rotation of the rotor can be controlled. The motor design is shown in Figure 1.6.

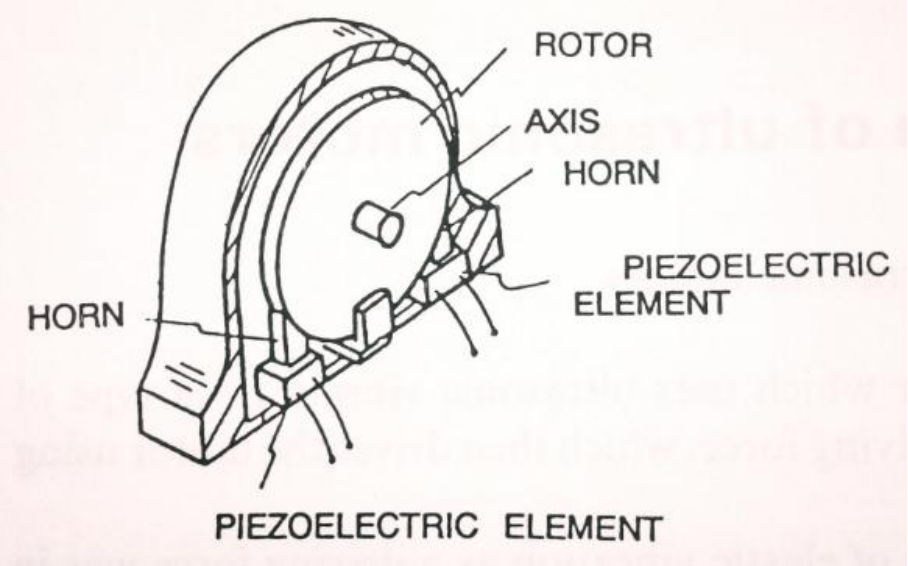

Figure 1.3 - Piezoelectric motor design by H. V. Barth in 1973 [8].

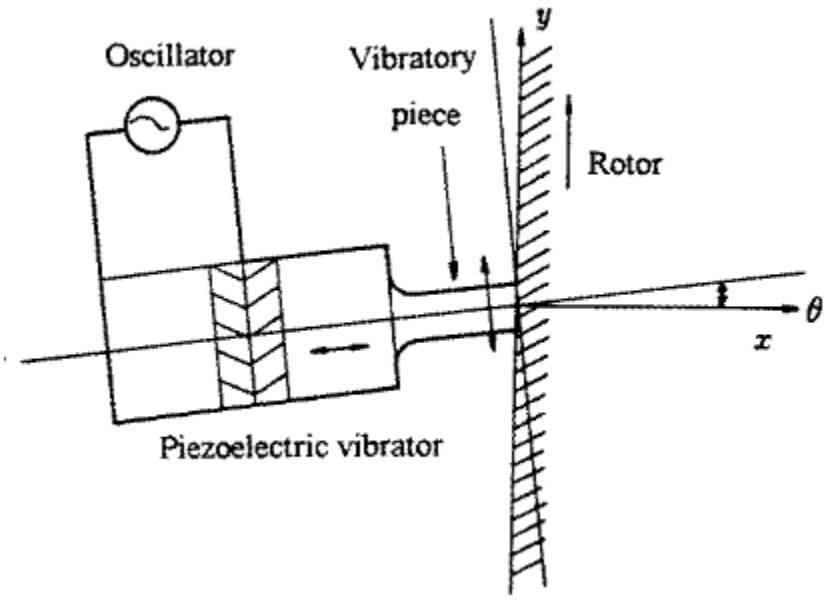

Figure 1.4 - Piezoelectric motor design by T. Sashida in 1982 [9].

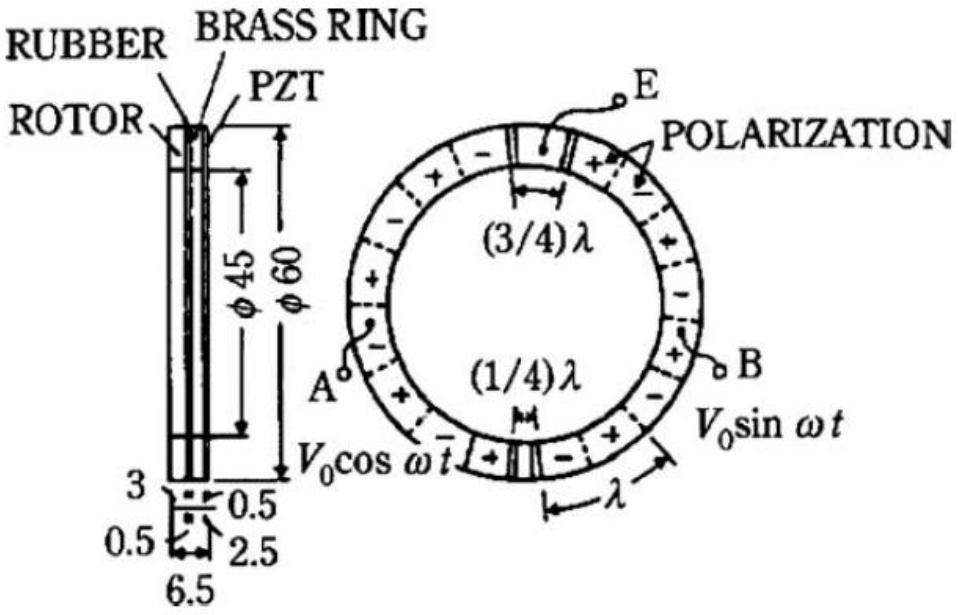

Figure 1.5 - Piezoelectric motor design by T. Sashida in 1983 [10].

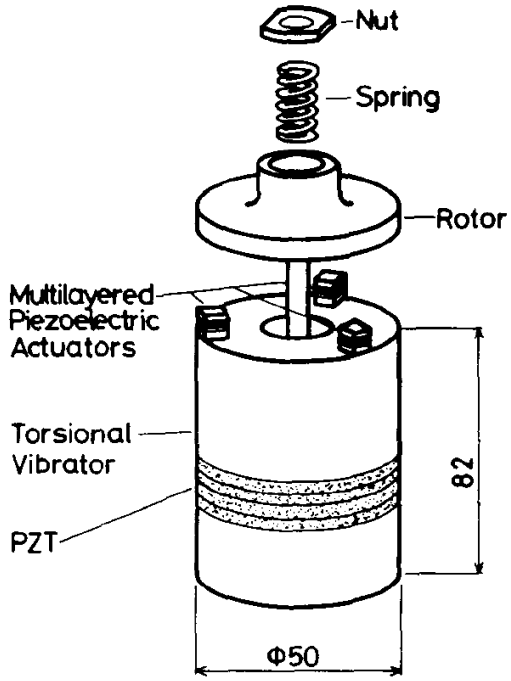

Figure 1.6 - Piezoelectric motor design by S. Ueha in 1988 [11, 12].

1.3 Advantages of piezoelectric ultrasonic motors

Piezoelectric ultrasonic motors have many advantages over conventional electromagnetic actuators. Following is a list of the features of the piezoelectric ultrasonic motors [8].

- An electromagnetic motor has a high efficiency at a high speed but low torque, but the ultrasonic motor has a high efficiency at a low speed and high torque;
- Control at start and stop is accurate since the inertia of the moving piece is low;
- Direct drive is possible since gear is not needed due to large torque;
- Precision positioning is possible due to no backlash since speed-reduction gears are not used;
- Friction force between the contact surface provides holding force at power-off state;
- High flexibility in choosing the shape of the motor due to simple rotor design and a vibration mode can be chosen depending on the stator shape;
- An option of designing a linear or rotary motor;
- Low noise due to gearless design;
- No danger of interference due to electromagnetic induction;
- Magnetic field is not used;
- Simple structure due to the absence of magnetic coils;

The energy density of different types of motors can also be compared [13]. Electro-magnetic actuators are known for their high energy density of 4×10^5 J/m^3. Small size electromagnetic motors up to centimeter-sized motors are fabricated without difficulty. However, as the size gets smaller, having magnetic coils become a serious disadvantage as it complicates

the structure as well as causes a problem of magnetic interference. Electrostatic actuators have small energy density of 4 x 10 J/m^3. However, considering Paschen's Law which increases the maximum electrical field with a smaller gap, the energy density is recalculated to be 2 x 10^5 J/m^3 which is in the same order as the energy density of electromagnetic actuators. For piezoelectric ultrasonic motors, PZT material is the most commonly used. PZT material can be distinguished as hard-type PZT and soft-type PZT depending on the additives of doping. Hard-type PZT has an energy density of 4 x 10^5 J/m^3 while the soft-type PZT has an energy density of 8.5 x 10^3 J/m^3. When energy densities of hard-type PZT motors and electromagnetic motors are similar, small size piezoelectric motors have advantages over electromagnetic motors in terms of simple structure since magnetic coils are not required.

1.4 Types of piezoelectric ultrasonic motors

1.4.1 Ultrasonic motor type categorization

Since the first invention of the piezoelectric ultrasonic motors, many different types of ultrasonic motors have been developed and reported. The structure and principle of operation using the reverse piezoelectric effect being relatively simple, there has been a rapid development of different shapes and applications of different types of motors. The ultrasonic motors can be categorized in many different ways, such as categorizing by the principle of operation, actuation direction, materials used, size, or geometry. In this thesis, the ultrasonic motors are categorized by the geometrical shape of the designs. Simply the ultrasonic motors can be identified as non-tubular type and tubular type. Non-tubular type motors include disk type, ring type, single layer type, and stack type. Among them the ultrasonic motors can be categorized by the excitation

mode into longitudinal mode, shear mode, and multi-mode. Tubular motors can be categorized into travelling wave type and standing wave type. There has been much development in travelling wave type and many literatures are found compared to standing wave type motors.

1.4.2 Non-tubular type ultrasonic motors

1.4.2.1 Disk type ultrasonic motors

Takehiro et al. report two disk type motors in 1992 and 1996 [14, 15]. He uses a steel disk of 60 mm diameter and 1.8 mm thickness for a stator design where piezoceramics in different shapes are bonded to. The principle of operation of his designs is using two degenerate bending vibration of the metal disk. Utilizing the bending vibration of the disk, the projective teeth placed in between the rotor and the stator rotates the rotor with frictional force. Figure 1.7 and Figure 1.8 show the concept and design of the disk type motor.

Nakamura et al. report a disk type ultrasonic motor in 1991 [16]. This motor design uses a hybrid transducer using two disks of piezoelectric elements for generating two vibration components independently. One is used as a torsional vibrator for generating the driving power while the other is a multilayered piezoelectric actuator for controlling the frictional force. The dimensions of the PZT disks used are 20 mm in diameter and 4 mm in thickness. At a working frequency of 24.5 kHz and the applied voltage of 250 V, the output power is about 2W with an efficiency of 21%. The motor configuration is shown in Figure 1.9.

Carotenuto et al. report a Langevin structure piezoelectric motor design using two piezoelectric disks in 2004 [17]. A bolted Langevin structure is used as a stator for excitation of flexural vibration with two piezoelectric disks placed in between two cylindrical inertial masses.

The piezoelectric disk is divided into four sectors and sinusoidal electrical signals with a phase difference of 90 ° are applied accordingly. The working frequency of this motor is at 77.1 kHz which is the third flexural vibration mode. With the maximum applied voltage of 350 V, the motor performs at a maximum speed of more than 2000 RPM and a maximum torque of more than 10 μNm. The configuration of the motor is shown in Figure 1.10.

Jun et al. report a piezoelectric linear motor using a disk type unimorph stator with a piezoelectric layer and a conductive layer in 2008 [18]. The diameter of the disk is 10.8 mm with a 3 mm inner hole and the thickness of 0.42 mm for both the piezoelectric layer and the metal layer. A moving shaft using a glass rod is placed in the hole of the stator. A linear motion of the glass rod is activated when a saw-tooth electric field is applied. A bi-directional linear motion of the shaft is enabled by the switching the direction of the applied electric field. The working frequency of the motor is 36.5 kHz. At an applied voltage of 80 V, the linear motor achieves about 4 mm/s of velocity. The configuration of the motor is shown in Figure 1.11.

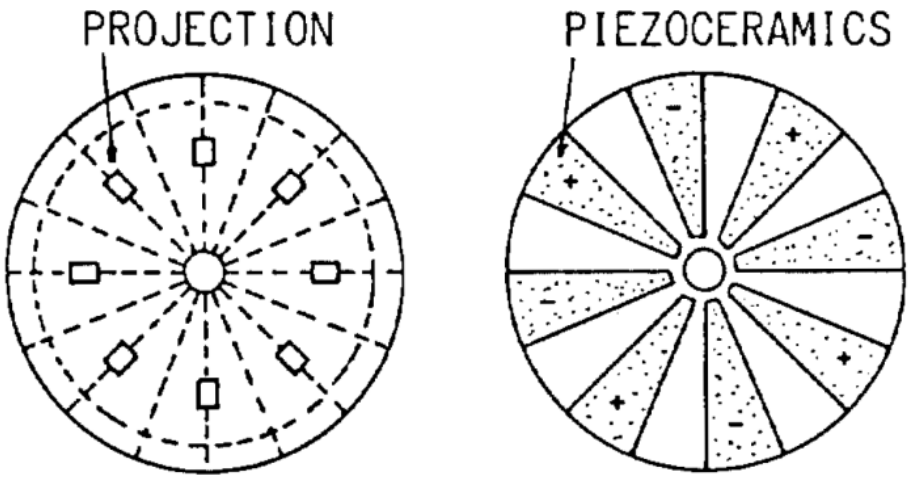

Figure 1.7 - Disk type motor configuration by Takehiro [14].

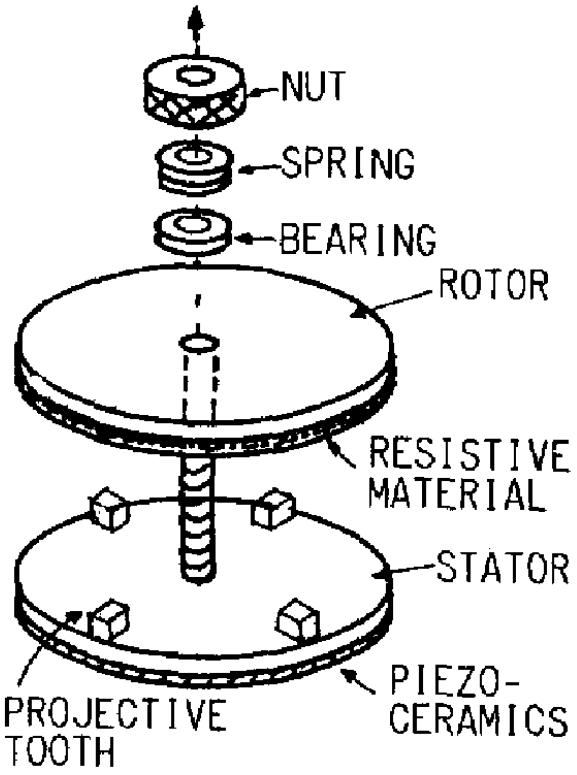

Figure 1.8 - Disk type motor assembly by Takehiro [15].

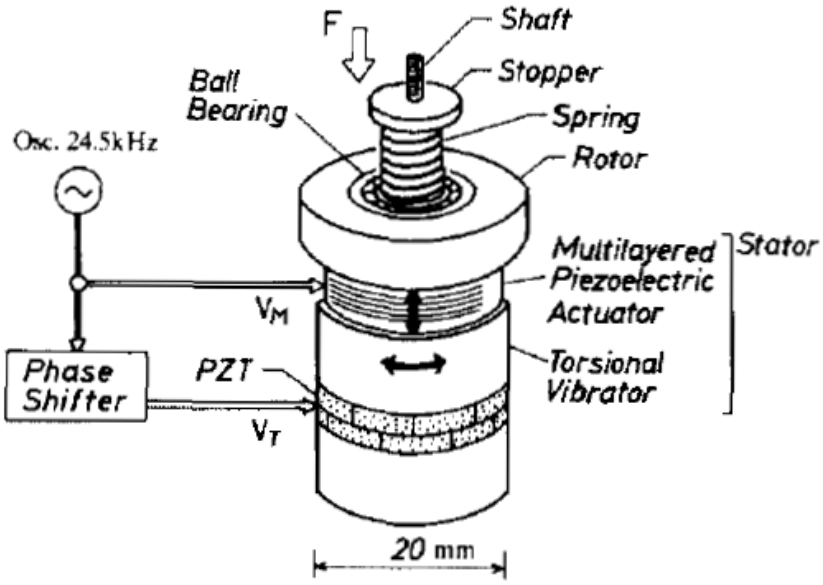

Figure 1.9 - Disk type motor configuration by Nakamura [16].

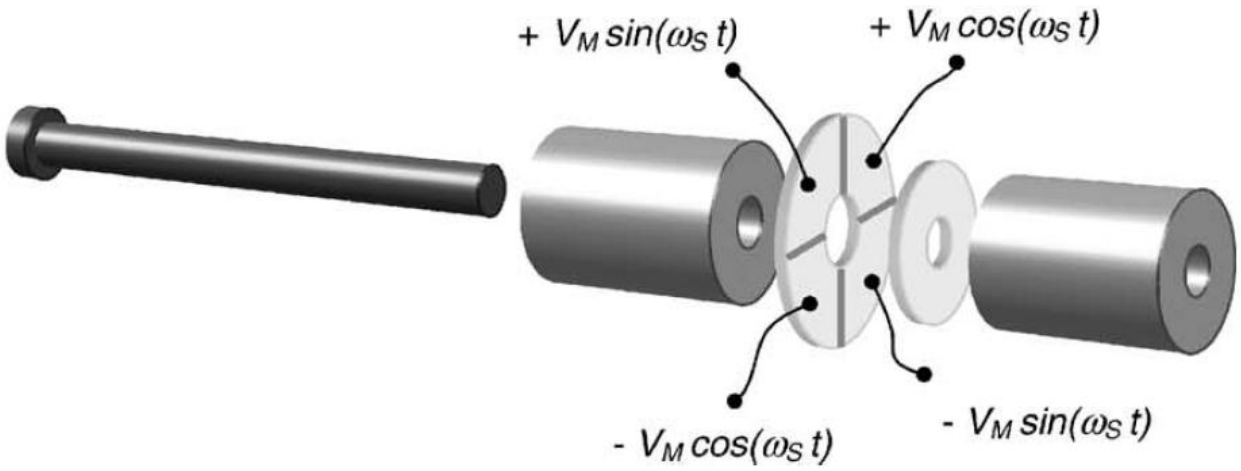

Figure 1.10 - Langevin structure motor configuration by Carotenuto [17].

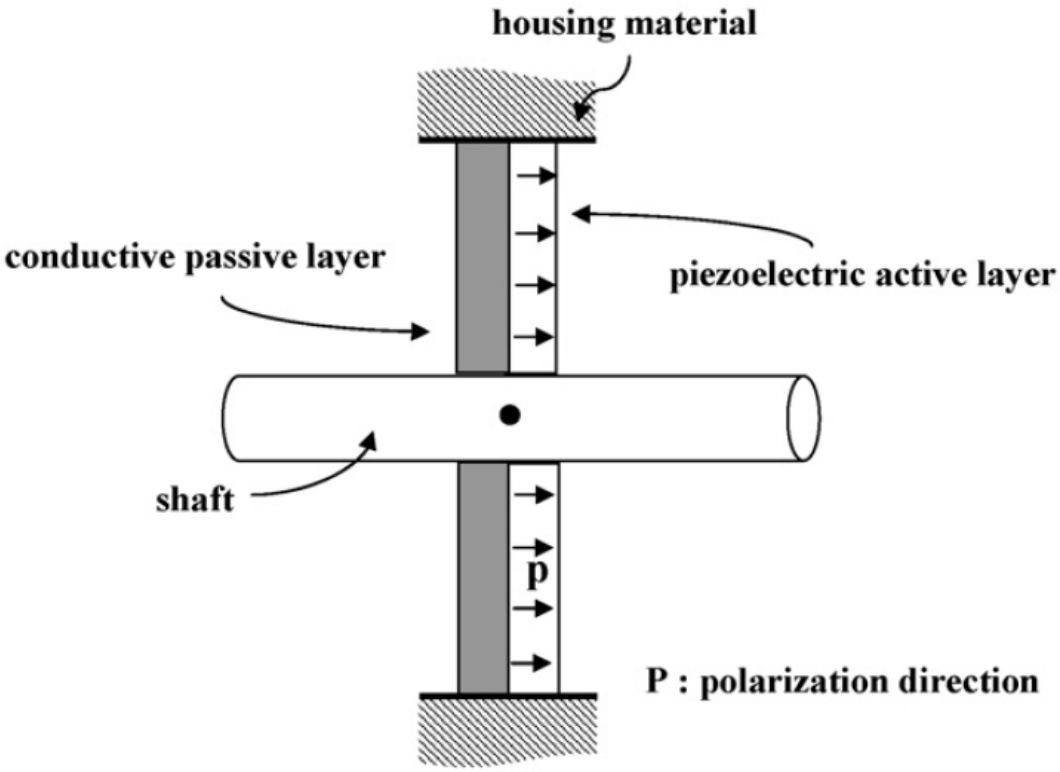

Figure 1.11 - Linear motor using disk type unimorph stator by Jun [18].

1.4.2.2 Ring type ultrasonic motors

Kurosawa and Ueha report a circular ultrasonic motor using a ring type transducer in 1991 [19]. A steel ring with 60 mm in outer diameter, 50 mm in inner diameter, and 2.6 mm in thickness is bonded to a PZT ring with same diameters with 1 mm in thickness. A traveling wave of second-order is excited on the PZT ring by dividing the electrode on the outer surface into eight segments. A single phase of sinusoidal electrical signal at a resonant frequency of 53.8 kHz is applied at every other divided segment, leaving four segments grounded. The configuration of the motor is shown in Figure 1.12.

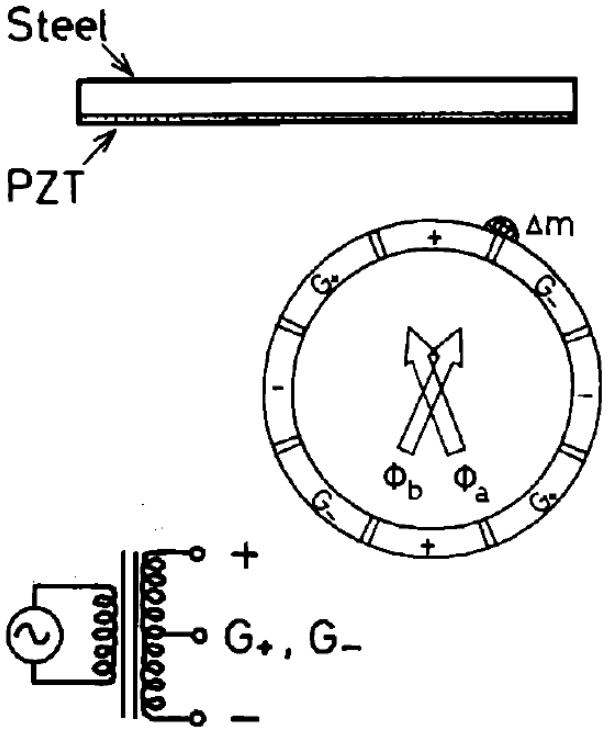

Figure 1.12 - Ring type transducer by Kurosawa and Ueha [19].

1.4.2.3 Single layer type ultrasonic motor

Zhai et al. report a linear ultrasonic motor using a single layer piezoelectric ceramic [20]. An elastic beam made of aluminum with projection teeth bonded to the actuator made of a single-layer piezoelectric ceramic is used as the stator vibrator. High friction material of carbon fibre reinforced plastic is used for the projection teeth. The dimension of the aluminum piece is 49.0 mm x 7.9 mm with a thickness of 3.0 mm where two pieces of piezoelectric ceramics of 11 mm x 7.9 mm with a thickness of 0.5 mm are bonded in the middle section. Two sinusoidal signals are separately applied to two piezoelectric ceramic pieces at different phase differences such as 40 °, 80 °, and 90 ° at a resonant frequency of 52.65 kHz to measure the linear motor speed. A stabilized speed of 52 cm/s is achieved. The configuration of this motor is shown in Figure 1.13.

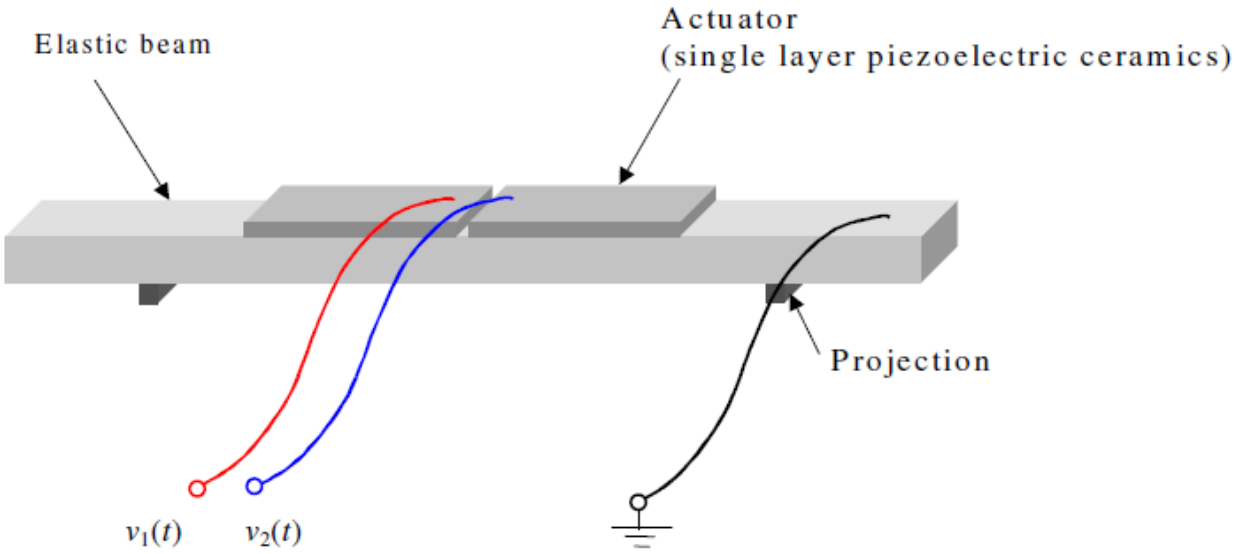

Figure 1.13 - Single-layer type ultrasonic motor by Zhai [20].

1.4.2.4 Longitudinal mode excitation type ultrasonic motors

Fleischer et al. report an ultrasonic piezoelectric motor with longitudinal oscillation in 1989 [21]. A rod shaped resonator vibrates in a longitudinal oscillation which is transformed into a continuous motion of the rotor with an arrangement of a drum. Superposition of two orthogonal moving components can produce a rotating motion of the tip of the resonator. A driving voltage of 350 V at the resonating frequency of 35 kHz is applied to achieve a rotation speed of more than 200 RPM. The concept of this type of motor is shown in Figure 1.14.

Petit et al. report a piezoelectric motor using longitudinal actuators using travelling wave in 1998 [22]. An elastic metallic ring with 12 piezoelectric rods attached is put in contact with a rotor. Two-phase sinusoidal signals with a phase difference of 90 ° are required for oscillating two standing waves on the PZT rods in longitudinal direction. A flexural progressive travelling wave is generated on the metallic ring surface which is transformed into a rotary motion of a rotor pressed on. The direction of rotation can be reversed by exciting the travelling wave in the opposite direction. PZT rods of 6.35 mm in diameter and 15 mm in length are placed on the metal ring. A maximum torque of 0.8 Nm and a no-load speed of 120 RPM are obtained. The construction of the motor is shown in Figure 1.15.

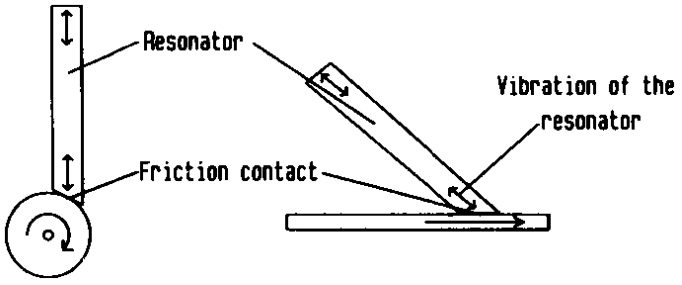

Figure 1.14 - Longitudinal excitation mode type motor by Fleischer [21].

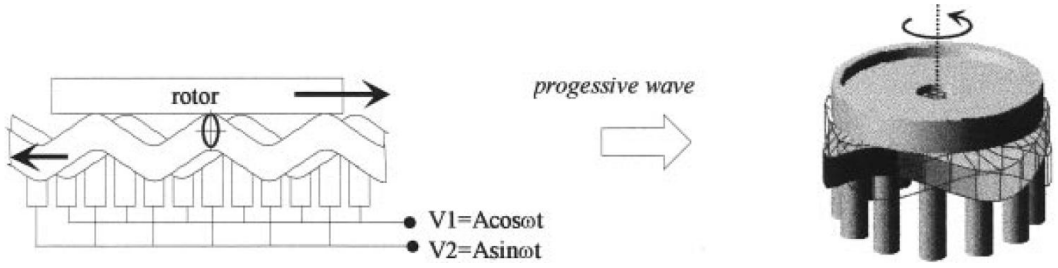

Figure 1.15 - Longitudinal oscillation PZT rods type motor by Petit [22].

1.4.2.5 Stack type ultrasonic motors

Yao et al. report a stack type longitudinal-bending mode piezoelectric ultrasonic motor using a multilayer of piezoelectric ceramics in 2001 [23]. A stack of ring shaped PZT ceramics with a diameter of 3 mm with a hole in the middle are put together as a stator of the motor. Since the disks are stacked, the bending vibrations of each piece are combined to a longitudinal vibration of the overall stator. Bidirectional rotation is possible with a change in driving frequency. Maximum starting torque of 127.5 μNm is observed and a 1070 RPM is reached at applied voltage of 80 V. The motor design is shown in Figure 1.16.

Nakamura et al. report a hybrid transducer type ultrasonic motor design with stack of PZT plates in 1993 [24]. The stator of the motor consists of two stacks of PZT layers; one for longitudinal vibration and the other for a torsional vibration. A rotor is pressed onto the stator using a spring with a preload. Two individual signal sources are required for actuation of the two stacks of PZT layers. Bidirectional rotation is achieved with two sources having a phase difference of 90 ° for one direction and 180 ° for the other direction. Configuration of the motor is shown in Figure 1.17.

Liu et al. report a cylindrical ultrasonic motor using stacked PZT plates as bending vibration transducer in 2011 [25]. The stator consists of a cylinder where a contact between the rotor and stator is made and a bending vibration transducer where four pieces of PZT plates are used. By exciting a bending vibration of the transducer, the cylinder can also vibrate in bending mode. Two cone shaped rotors are in contact to the teeth of the cylinder which generate a rotating motion of the rotors. With an exciting voltage of 200 V, a no-load speed of 165 RPM and maximum torque of 0.45 Nm are observed. The prototype design is shown in Figure 1.18.

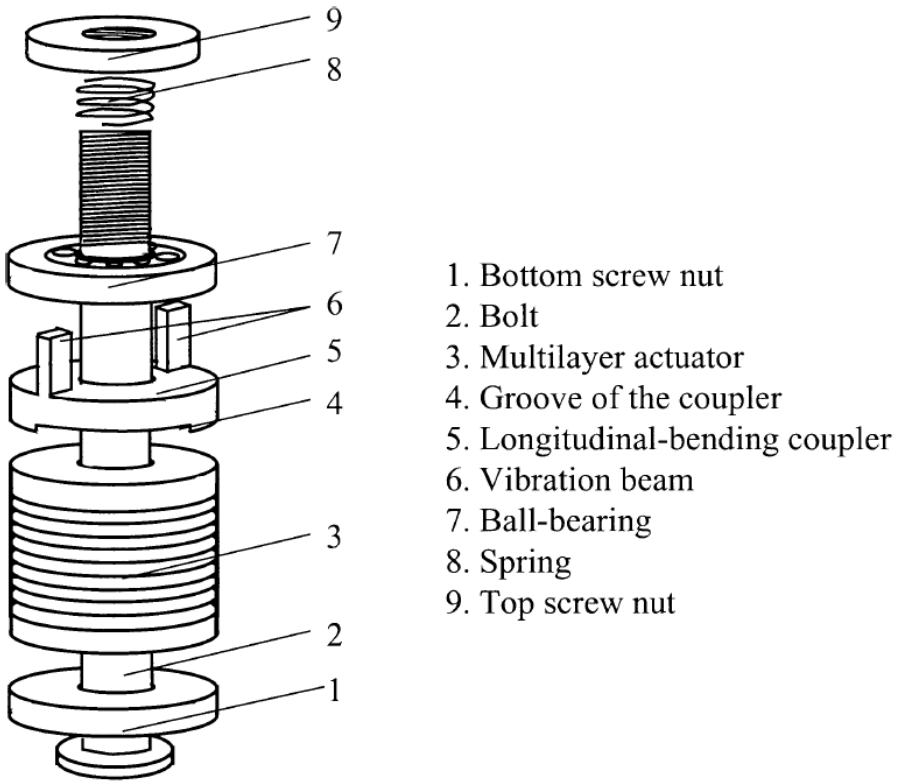

Figure 1.16 - Stacked PZT ring motor design by Yao [23].

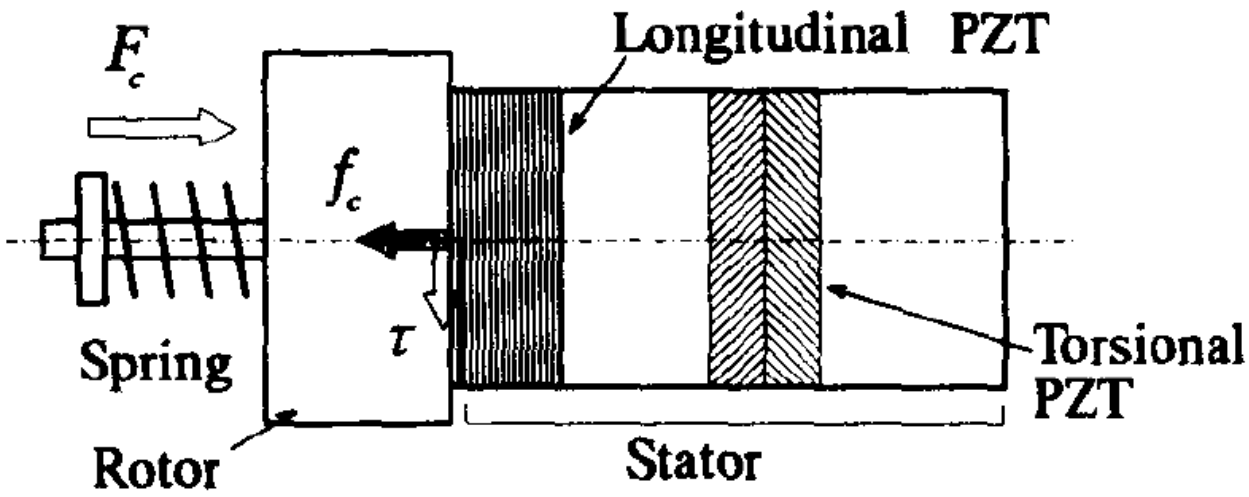

Figure 1.17 - Stack type motor design by Nakamura [24].

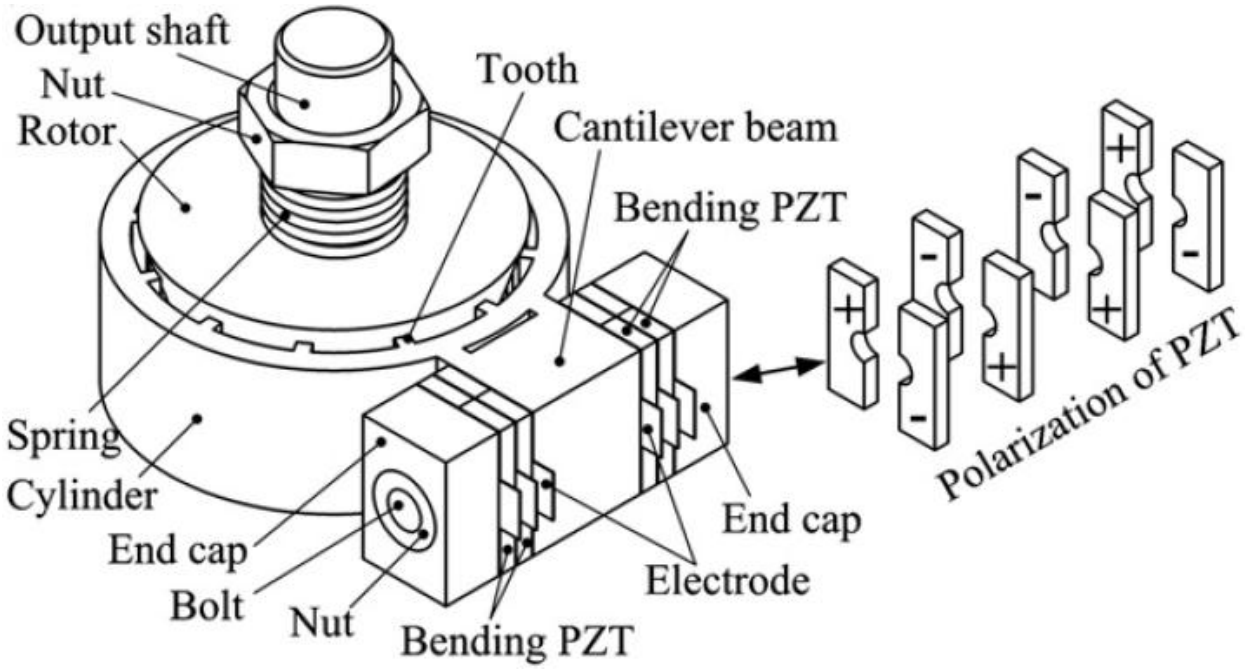

Figure 1.18 - Stacked cylindrical motor design by Liu [25].

1.4.2.6 Shear mode excitation type ultrasonic motors

Aoyagi et al. report a shear mode type piezoelectric actuator in 1996 [26]. A torsional vibrator with four piezoelectric ceramics sandwiched inside along the axial direction is designed for high power ultrasonic motor design. Two arch shaped metal blocks are placed around the piezoelectric ceramics. The poling directions of the piezoelectric ceramics are in opposite direction in order to enable a shear mode excitation. The motor configuration is shown in Figure 1.19.

Glazounov et al. report a torsional actuator using mechanical amplification of a piezoelectric shear strain in 2000 [27]. An even number of piezoelectric ceramic segments are bonded with conductive epoxy to form a tube shaped actuator. The gap between the segments acts as electrodes where electric fields are applied. The polarization direction of adjacent segments alternates along the length direction. When electric fields are applied, the segments exhibit coherent shear deformations which are combined to an angular displacement. The dimension of the tube is 127 mm of outer diameter, 96 mm of inner diameter, and 635 mm of length. The configuration of the tube design is shown in Figure 1.20.

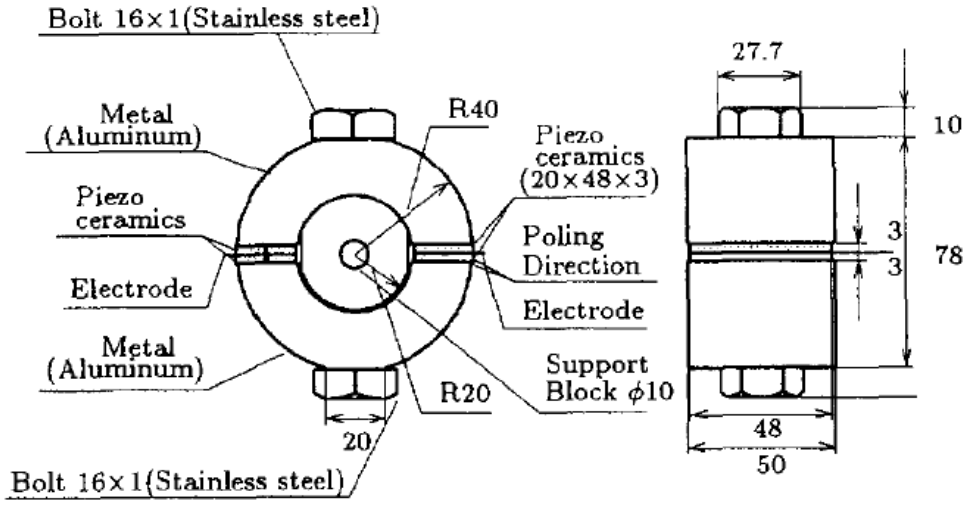

Figure 1.19 - Shear mode ultrasonic motor prototype by Aoyagi [26].

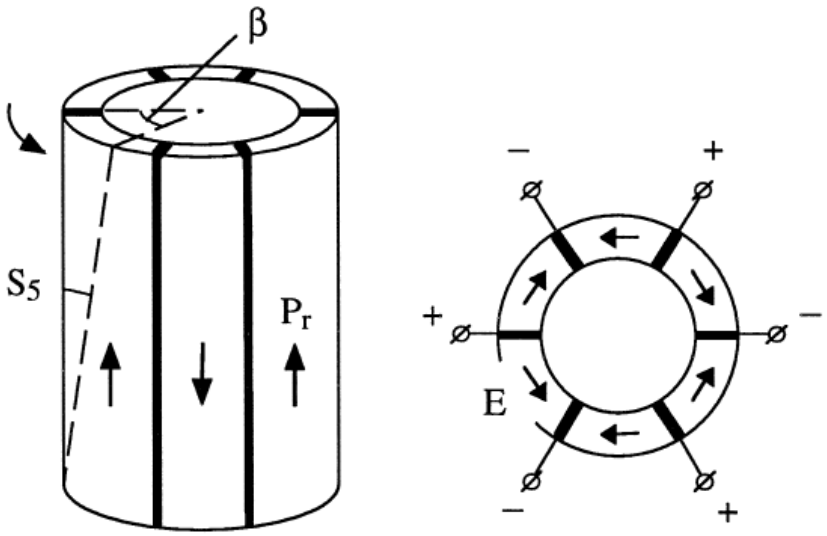

Figure 1.20 - Shear mode tube design by Glazounov [27].

1.4.2.7 Multi-mode excitation type ultrasonic motors

Briot et al. introduce different types of multi-mode excitation type ultrasonic motors in 1993 [28]. Two piezoelectric elements are used for independently exciting two different

vibrations. There are thickness-shearing modes, longitudinal-torsional modes, and orthogonal-longitudinal modes.

Tsujino et al. report a longitudinal-torsional vibration mode ultrasonic rotary motor in 1992 [29]. The longitudinal-torsional stator consists of three parts. The longitudinally vibrating cylinder part is driven by the longitudinal vibration system. At the end of the cylinder, an array of thin metal rods are put together to form a cylinder. The metal rods are bent about 45 ° at the longitudinal vibration node. The bent rods convert the longitudinal vibration into a diagonal direction vibration, which is the torsional vibration. Two prototypes of 40 mm diameter tube and 50 mm diameter tube are designed. The motor design is shown in Figure 1.21.

Ohnishi et al. report a longitudinal-torsional composite resonance vibration mode ultrasonic motor in 1993 [30]. Two piezoelectric ceramic blocks are used for individually oscillating a longitudinal vibration mode in one and torsional vibration mode in the other. A simultaneous oscillation of two modes in the stator is possible using two sources of sinusoidal electric fields. From the longitudinal oscillation period, the stator extends and compresses. When it extends, the stator is put into contact with the rotor which generates a rotation motion with the torsional vibration mode from the stator. A prototype motor with 20 mm diameter is observed to have a maximum rotation speed of 450 RPM when 88 V is applied at 30.5 kHz. The ultrasonic motor construction is shown in Figure 1.22.

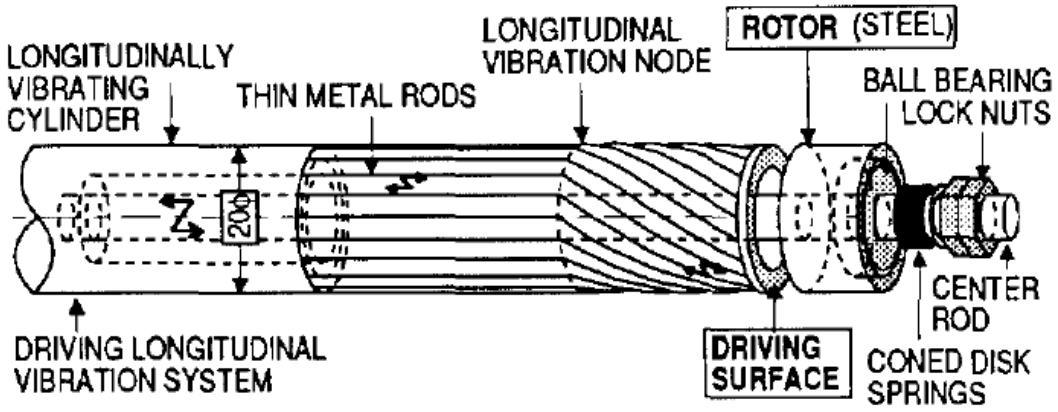

Figure 1.21 - Longitudinal-torsional mode ultrasonic motor design by Tsujino [29].

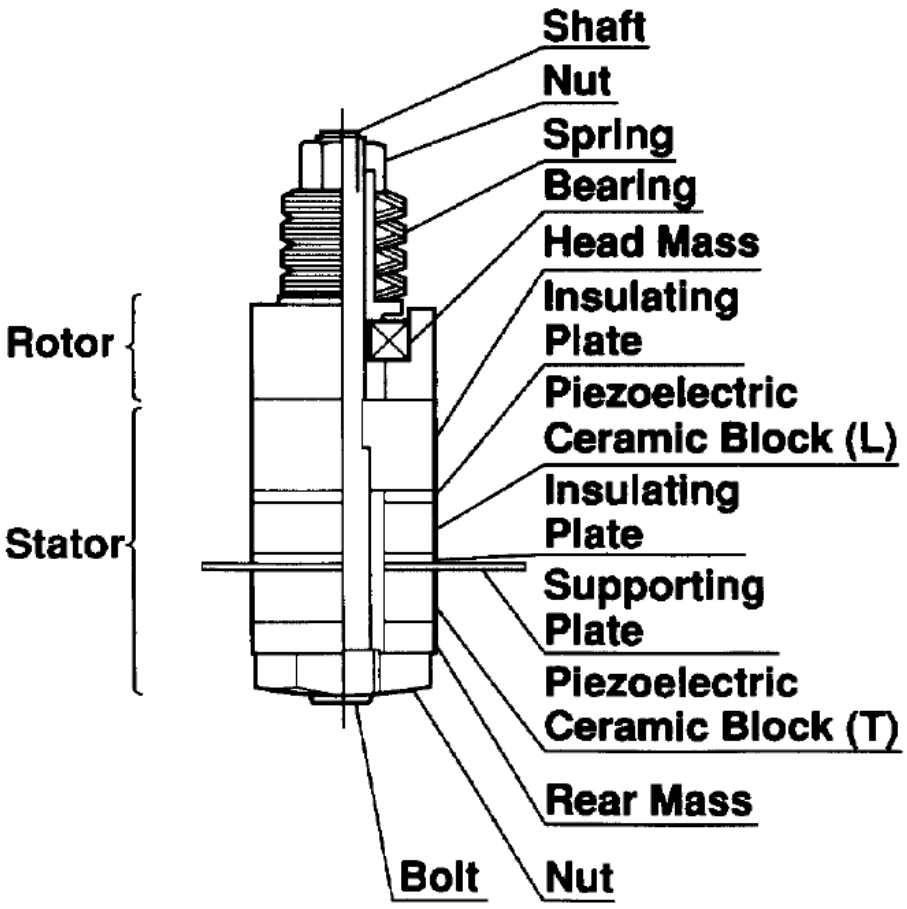

Figure 1.22 - Longitudinal-torsional mode motor construction by Ohnishi [30].

1.4.3 Tubular type ultrasonic motors

1.4.3.1 Travelling wave type motors

There are many literatures describing tubular travelling wave type ultrasonic motors. Hagood IV et al. illustrate a principle of operation for travelling wave type in Figure 1.23 for generation of mechanical motion from the amplification and repetition of deformations of piezoceramics [31]. These motors can be further categorized into three sections; bulk PZT tube motor, metal tube motor with thin film deposition of PZT, metal tube motor with bonded PZT pieces. Most travelling wave type tubular ultrasonic motors work with similar principle of operation. They require two sources of sinusoidal to excite two orthogonal bending modes which are combined to excite a travelling wave on the outer surface or at the tip of the tube. This is called vibration mode coupling which require a precise manufacturing and calibration technique since the two frequencies of bending modes should be very close to each other.

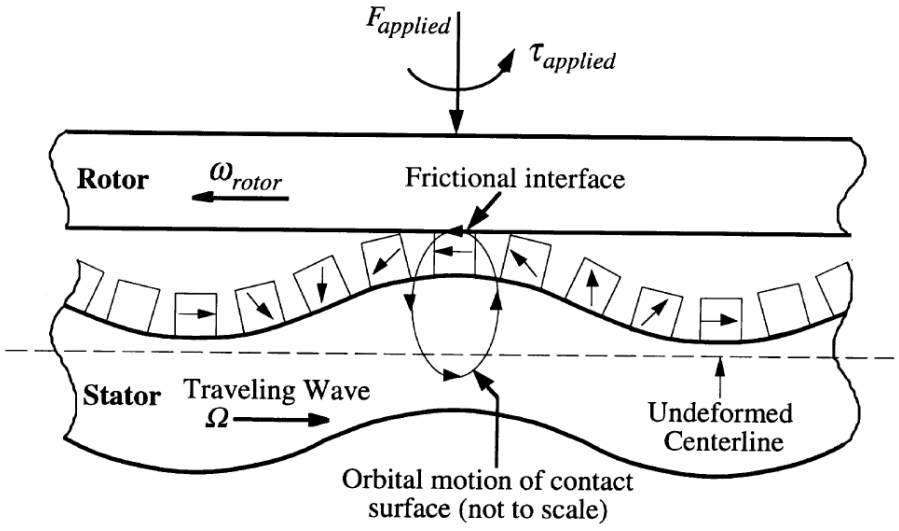

Figure 1.23 - Rotating motion generated by travelling wave [31].

1.4.3.1.1 Bulk PZT tube type motors

Dong et al. report a bulk PZT tube design in 2003 [32]. A diameter of 1.5 mm with 7 mm in length of bulk PZT tube is used for construction of the motor. Outer surface electrode is divided into four segments which are driven with two sources of sinusoidal signals for generating wobbling motion at its ends which are in contact with the rotors. At a resonant frequency of 67 kHz with amplitude of 66 V, the motor rotation speed is observed to be about 1800 RPM with maximum torque of 20 μNm. The motor design is shown in Figure 1.24. Zhang et al. also report a bulk PZT tube with similar operating principle in 2006 [33]. The dimensions of the bulk PZT tube are am outer diameter of 1.0 mm, inner diameter of 0.6 mm, and length of 5.0 mm. At a resonant frequency of 58 kHz with amplitude of 110 V, the motor performs at 3000 RPM and at a maximum torque of 7.8 μNm. The motor design is shown in Figure 1.25.

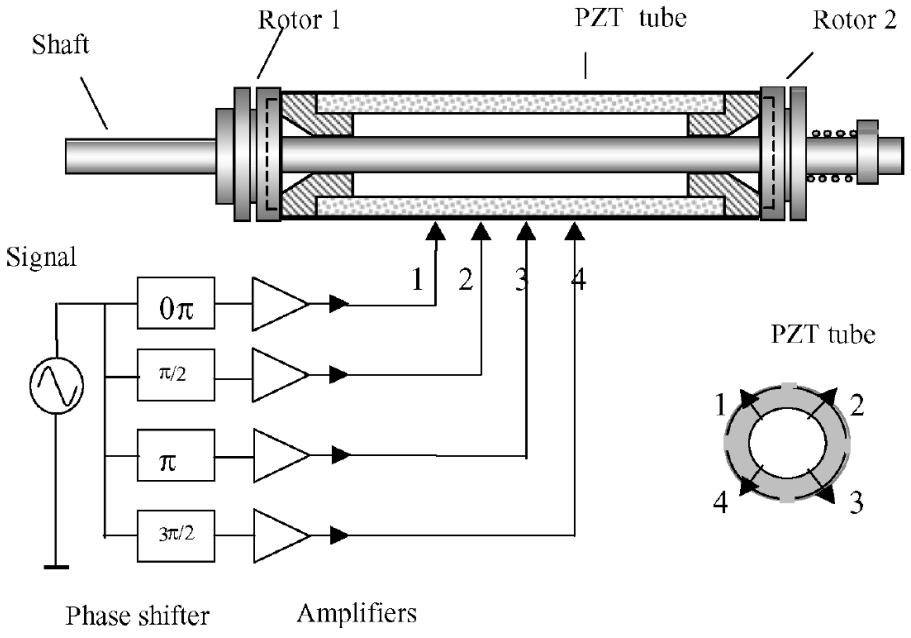

Figure 1.24 - Bulk PZT tube travelling wave type motor by Dong [32].

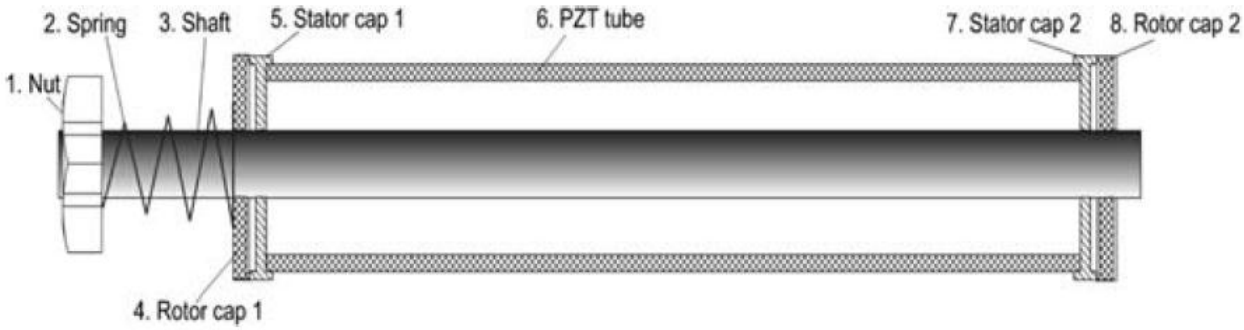

Figure 1.25 - Bulk PZT tube travelling wave type motor by Zhang [33].

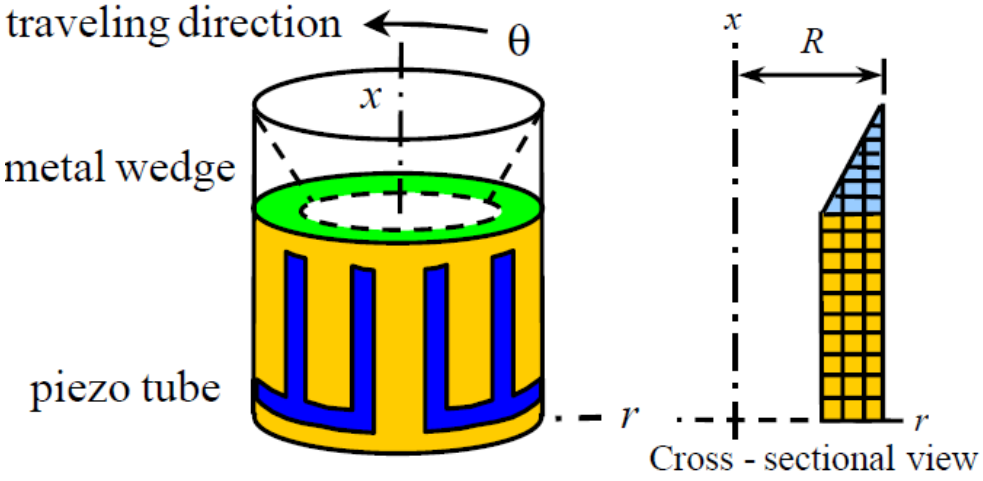

Figure 1.26 - Bulk PZT tube travelling wave type motor by Yin [34].

1.4.3.2.2 Metal tube with a thin film deposition of PZT motor

Morita et al. report a travelling wave tubular type motor using a cylindrical titanium tube with PZT thin film deposited on the outer surface [35], [36]. The dimensions of the titanium tube is 2.4 mm in diameter, 10 mm in length, and 0.25 mm in thickness with a thickness of 9 μm of PZT film deposited. Advantage of using titanium tube is higher durability compared to bulk

PZT tube motor. The principle of operation is same as the bulk PZT type motor, combining two standing waves into a travelling wave. With a driving voltage of 15 V at a resonant frequency of 109.6 kHz, the motor has a maximum speed of 880 RPM and an output torque of 6.3 μNm. Prototype motor is shown in Figure 1.27.

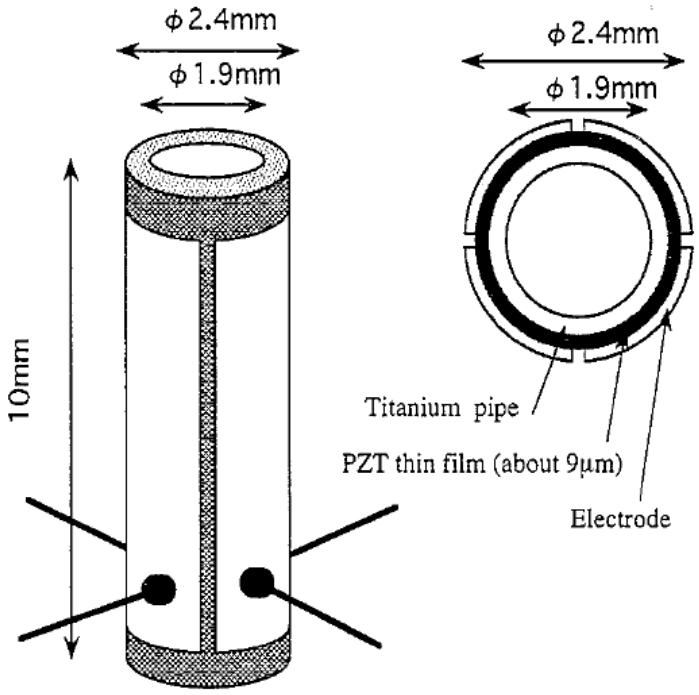

Figure 1.27 - Thin film PZT on metal tube travelling wave type motor by Morita [35].

1.4.3.2.3 Metal tube with bonded PZT pieces motor

Koc et al., Dong et al., and Cagatay et al. report a travelling wave type motor using a metal tube with two pieces of PZT pieces bonded on two sides of the cylindrical tube [37 ~ 39]. Advantage of this motor compared to previous travelling wave type is that a single source of sinusoidal signal can generate two orthogonal bending modes while the other designs require two sources. A brass tube of outer diameter of 1.6 mm and inner diameter of 0.8 mm with length of

6 mm is used and two pieces of PZT plates with dimension of 1 mm x 6 mm x 0.3 mm are bonded on flattened two sides. Between the two pieces of PZT plates, driving one plate with the electrical signal at resonant frequency can couple the two orthogonal bending vibration modes into a travelling wave in a wobble motion. Driving the other PZT plate generates a wobble motion in the other direction, therefore a bidirectional motion is enabled. The rotor can be placed on the middle section of the tube as shown in Figure 1.28, or on the ends of the tube as shown in Figure 1.29. When the rotor is placed on the middle of the tube, the motor has a maximum rotation speed of 70 RPM and a maximum torque of 50 μNm with a resonance frequency of 46 kHz and amplitude of 70 V. When the rotor is placed on the end of the tube, the motor has a maximum rotation speed of 2200 RPM and the maximum torque of 0.87 mNm when it is driven at a resonance frequency of 130 kHz with amplitude of 100 V.

Zhu et al. report a cylindrical ultrasonic motor using a metallic cylinder with four pieces of piezoelectric pieces in 2008 [40]. A cylindrical phosphor bronze cylinder with an outer diameter of 4.8 mm, inner diameter of 3.2 mm, and length of 18 mm is used for the metallic cylinder. Four pieces of rectangular PMN-PT pieces with a dimension of 6 mm x 2.65 mm x 0.5 mm are bonded to the four flattened surfaces of the tube. Two spherical rotors are put in contact to the two ends of the stator. The wobble motion of the stator is driven with two sources of sinusoidal voltage sources. At a driving frequency of 49.4 kHz and amplitude of 100 V, the motor has maximum torque of 2.8 mNm and a maximum rotation speed of about 400 RPM. The motor prototype is shown in Figure 1.30.

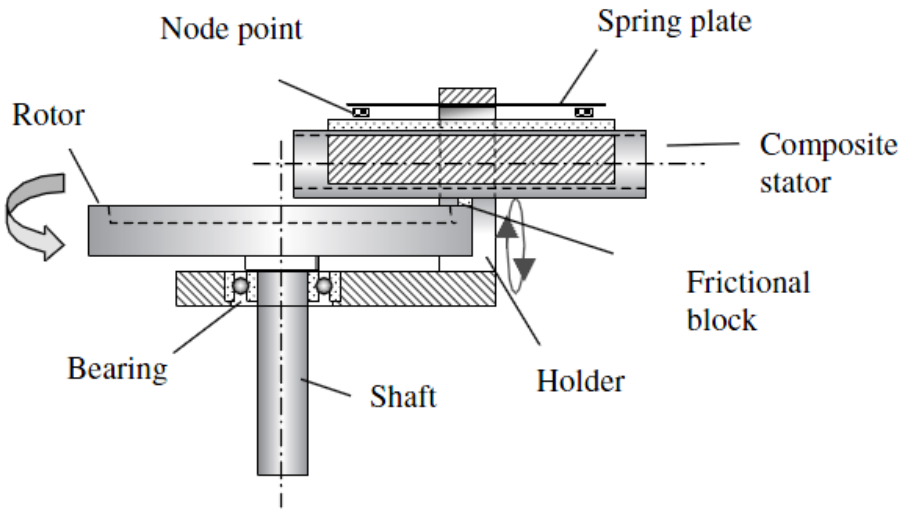

Figure 1.28 - Metal tube with bonded PZT with rotor placed on the middle of the tube [38].

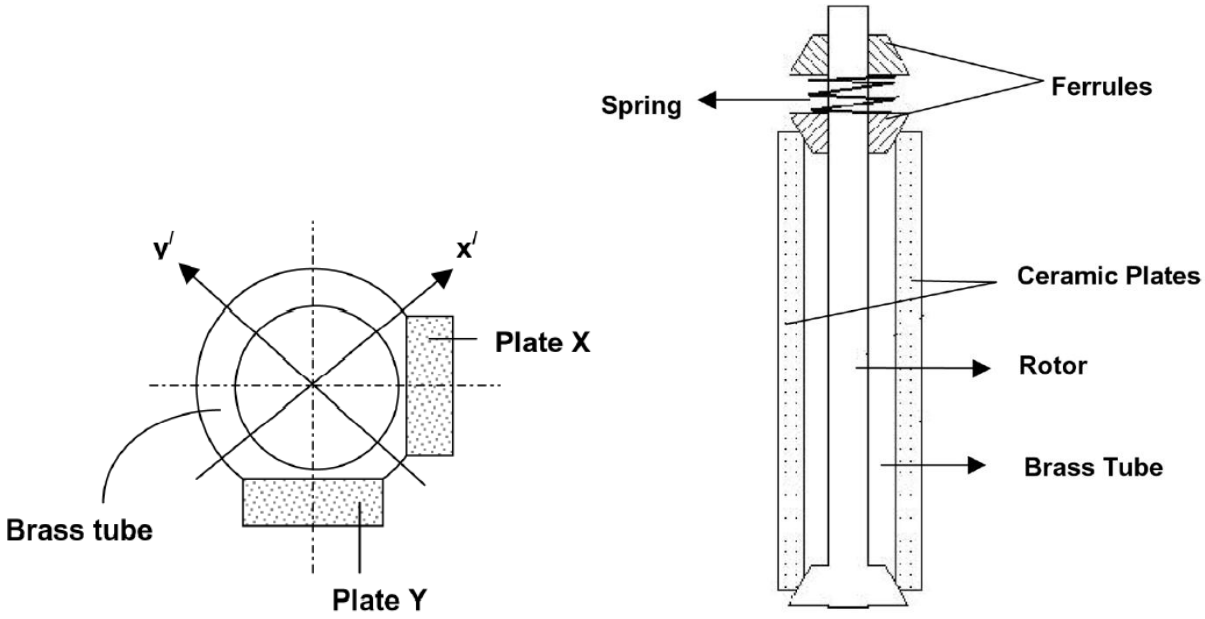

Figure 1.29 - Metal tube with two PZT pieces bonded with rotor placed on the ends of the tube [39].

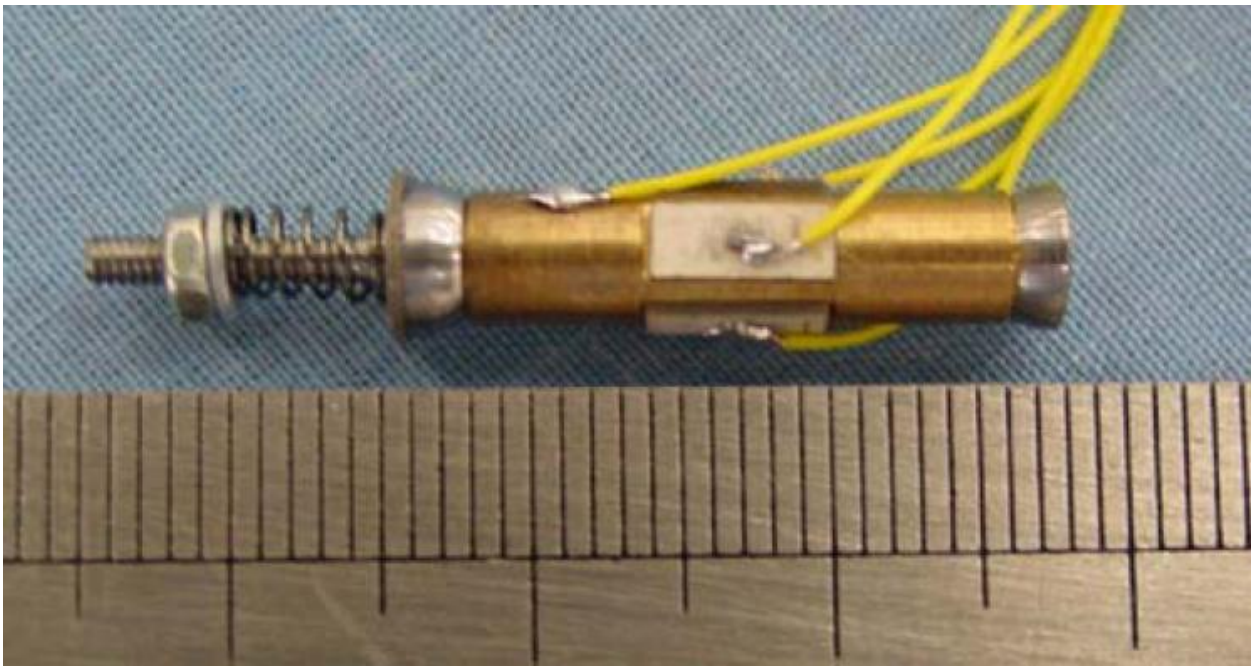

Figure 1.30 - Cylindrical ultrasonic motor prototype by Zhu [40].

1.5 Objective of the Thesis

1.5.1 Problem statement

Tubular type piezoelectric ultrasonic motors have advantages over non-tubular types. Simple structure and accurate control of tubular type motors are well suited for high precision positioning applications. However, most tubular type ultrasonic motors in literatures follow the travelling wave principle of operation. There are some disadvantages with travelling wave type motors. In most cases, this type of motor requires two separate sources of sinusoidal signals to be applied simultaneously for generation of two standing waves. Having two sources can complicate the structure and configuration of the motor setup as well as increases the cost of circuit and control. The two standing waves generated by two signals are coupled with vibration mode coupling to generate a travelling wave. This vibration mode coupling requires a very accurate machining of the tube so that the two bending modes are found at the same frequency range. As the structure of the motor becomes smaller, the tolerance becomes smaller as well and it becomes more difficult to fabricate very accurately. Motors developed in literatures [38, 39] report travelling wave type motors only requiring a single source of sinusoidal signal. However, this design still poses a vibration mode coupling disadvantage. These problems can be solved with a standing wave type motor.

1.5.2 Objective

The objective of this thesis is to develop a novel standing wave type tubular piezoelectric ultrasonic motor driven by a single source of signal and a single vibration mode. The advantages of this design are that it simplifies the configuration since only one source of sinusoidal electrical

input is required and it eliminates the need for vibration coupling. The motor structure is simplified and higher flexibility in design can be achieved since the tolerance of fabrication is increased. In order to meet the objective, the designs and simulations of novel piezoelectric ultrasonic motors are carried out. Prototypes of designs are fabricated and performances are tested using test apparatus. In order to optimize and improve the performance of the prototype in terms of speed and torque, a second iteration of designing and prototyping is carried out.

This thesis is composed of six chapters in total. Followed by abstract, Chapter 1 is an introduction chapter where background information on piezoelectricity and historical background of piezoelectric ultrasonic motors is described. A summary of literature reviews on various types of motors are also reported in this chapter. In the end of the Chater 1, the problem statement and objective of the thesis are stated. Chapter 2 describes two prototypes of ultrasonic motors fabricated and tested. These prototypes are the first iteration of ultrasonic motors fabricated with cylindrical PZT tubes. The principle of operation is described, prototype description follows, motor performance test results are reported, and analytical models from literatures are used to compare the performance results with analytical models. Chapter 3 describes a second iteration of ultrasonic motor prototype which is fabricated with a rectangular brass tube with bonded PZT plates. Principle of operation is described, prototype description follows, and experimental test results are reported. Chapter 4 discusses a novel waveform measurement methods of the piezoelectric ultrasonic motors to distinguish a travelling wave from a standing wave and also to verify that the prototypes vibrate in a standing wave form. Chapter 5 describes applications of piezoelectric ultrasonic motors in literatures. Chapter 6 concludes the thesis with recommended future work.

Chapter 2. PZT Tube Motor Design

2.1 Chapter introduction

In this chapter, two prototypes of piezoelectric ultrasonic motors are reported. The prototypes are standing wave type motors fabricated with cylindrical PZT tubes with four separate electrodes on the outer surface and one common electrode on the inner surface. These two prototypes are the first iteration prototypes which can be further optimized. The motors use a single vibration bending mode of the stator PZT tube for a rotation of the rotor which require only one driving signal. Switching the direction of bending enables bi-directional motion. Since vibration coupling is not required, the fabrication and operation is simplified compared to travelling wave type motors.

First part of this chapter describes the principle of operation of the prototype which explains how a single bending mode is excited and is used for generating a rotating motion of the rotor. Next part reports the prototype description including dimensions of the parts and fabrication methods followed by the experimental testing setup configuration description and motor performance test results. Last part of the chapter introduces three analytical models for static analysis, displacement analysis, and vibrational analysis of the motor performance which is compared to the experimental results. The two prototypes are compared throughout the chapter in parallel.

A journal paper has been published on the two piezoelectric ultrasonic motors described in this chapter. Most of the works and figures are referenced to that publication [41].

2.2 Principle of operation

2.2.1 Tube configuration

The stator of the motor consists of a piezoelectric tube made of PZT material. It has four individual exterior electrodes on four equal quadrants and one common interior electrode. For outer electrodes, electrical signals can be separately applied onto each quadrant. However, adjacent electrodes are paired for actuating purpose. The interior electrode is held at floating potential. When a sinusoidal electrical potential is applied between the paired electrodes, one half of the tube expands while the other half of the tube contracts. This causes the tube to vibrate in the bending mode along orthogonal directions. There are two orthogonal directions the bending vibration can occur and the direction can be controlled by the electrode pairing. The bending mode vibration and electrode pairing is shown in Figure 2.1.

2.2.2 Trajectory of the tube end points

The trajectories of the tube end points of the piezoelectric tube during deflection can explain the principle of operation of the ultrasonic motor. The four quadrants of the tube are labeled as Qu1, Qu2, Qu3, Qu4, and points 1, 2, 3, 4, 5 are selected arbitrarily in Figure 2.2 (a). Note that the axes X, Y, Z, and r_1, r_2, r_3, r_4, r_5, and t_1, t_2, t_3, t_4, t_5 are referenced to the resting position of PZT tube. The trajectories of the five selected points can be analyzed assuming that the tube vibrates in bending mode along X axis. Note that the trajectories are represented in a qualitative manner.

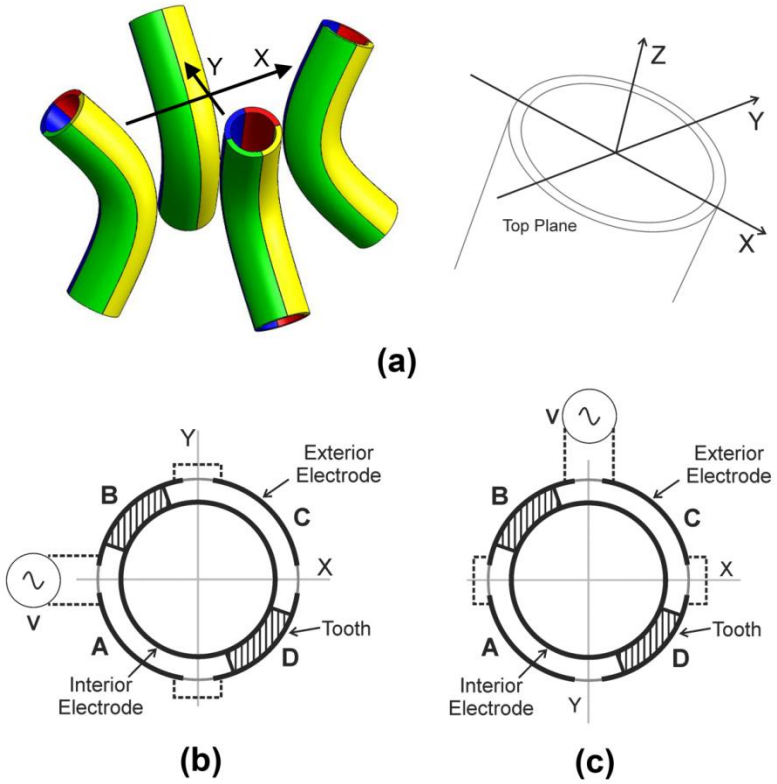

Figure 2.1 - Bending mode vibration of the piezoelectric tube [41]. (a) Two orthogonal bending directions. (b) Electrical pairing for bending along Y and X directions.

Figure 2.2 (b) represents the deflection of the tube along X axis and the five points selected on Qu1. The points in Qu1 move in an arc in planes parallel to the Y-Z plane, diagonally upwards and downwards when the tube bends in the y+ and y- directions respectively. The trajectory is same for moving upward or downward direction. Note that the net movement in Z direction is different for the five points as point 1 has the greatest movement while the point 5 has almost no movement.

Figure 2.2 (c) and (d) represents the radial and tangential components of the trajectory of the selected points. The radial components of the trajectories are diagonal lines in the direction

of upwards and to the center of the tube. The tangential components of the trajectories are in the direction of upwards and to the counter-clockwise direction, from outside point of view. Point 1 shows no motion in tangential direction while point 5 shows no motion in radial direction.

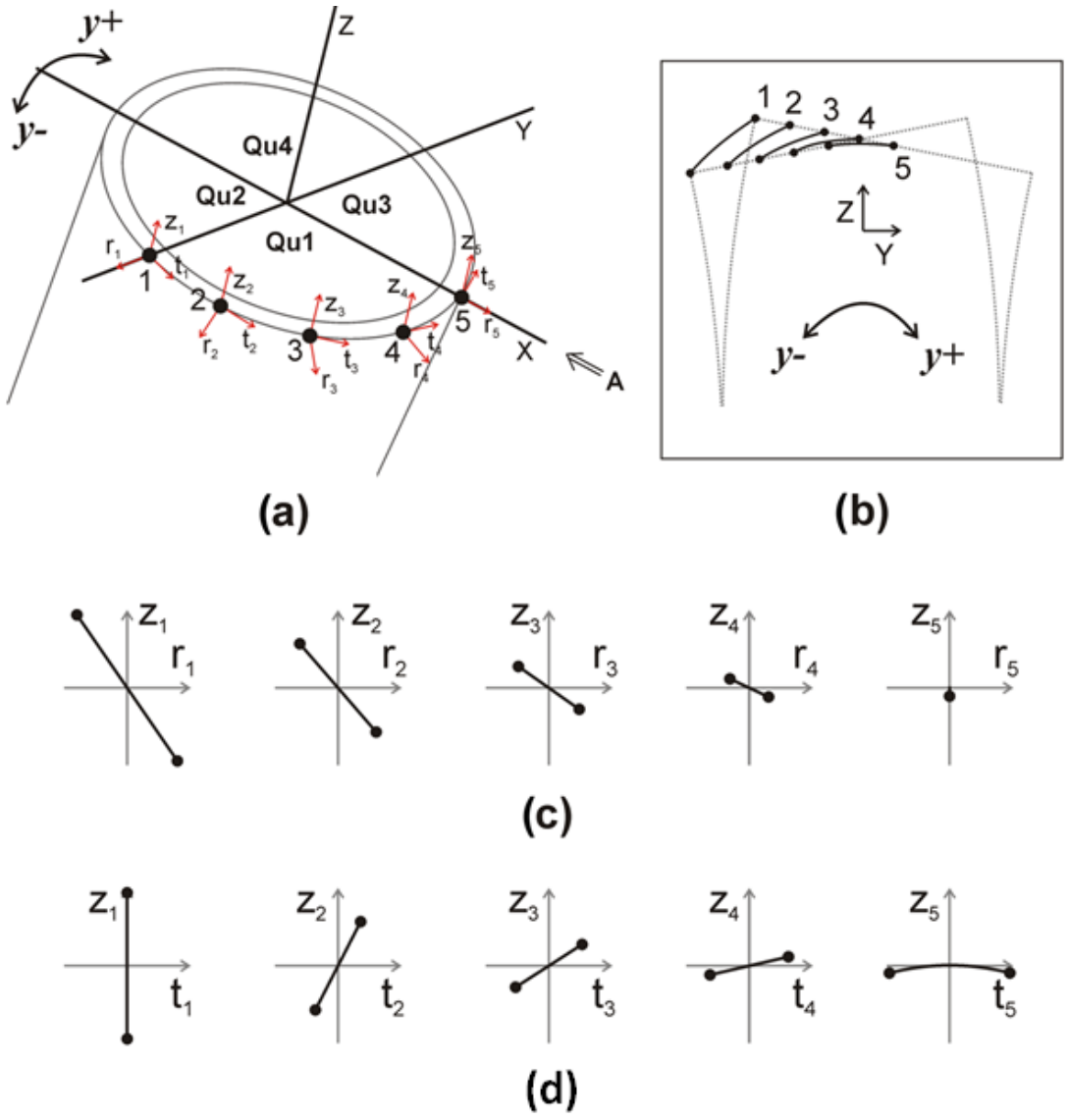

Figure 2.2 - The trajectories of the tube end points during a bending vibration along X axis [41]. (a) Four quadrants and selected five points in Qu1. (b) Trajectories of selected points. (c) Radial components. (d) Tangential components.

This analysis of the trajectory of the endpoints can be done on all quadrants. Assuming that the tube vibrates in bending mode along X axis, the points on Qu1 would be the same as the points on Qu4 while the points on Qu2 and Qu3 would be symmetrically opposite. From this analysis, following conclusions can be made. The radial components of the trajectories of the points on all four quadrants of the end of the tube are in direction of upwards and to the center of the tube. The tangential components of the points in Qu1 and Qu4 are in the direction of upwards and along the counter-clockwise direction while the tangential components of the points in Qu2 and Qu3 are in the direction of upwards and along clockwise direction. The clockwise and counter-clockwise directions are referenced to the viewpoint of the tube from outside.

2.2.3 Rotation driven by diagonal motion

As the diagonal tangential trajectories of the points on Qu1 and Qu4 are in the direction upwards and towards the counter-clockwise direction during the bending vibration of PZT tube along X axis, pressing a rotor onto only the points on these two quadrants can continuously drive the rotor in rotation along counter-clockwise direction. Similarly, a rotor can rotate continuously in clockwise direction when it is pressed on the points on Qu2 and Qu3 only. This is shown in Figure 2.3. The principle of reciprocating diagonal motion for generating a continuous movement is previously reported by [42]. Other ultrasonic motors using the motion of diagonal trajectories are reported by [43], [44].

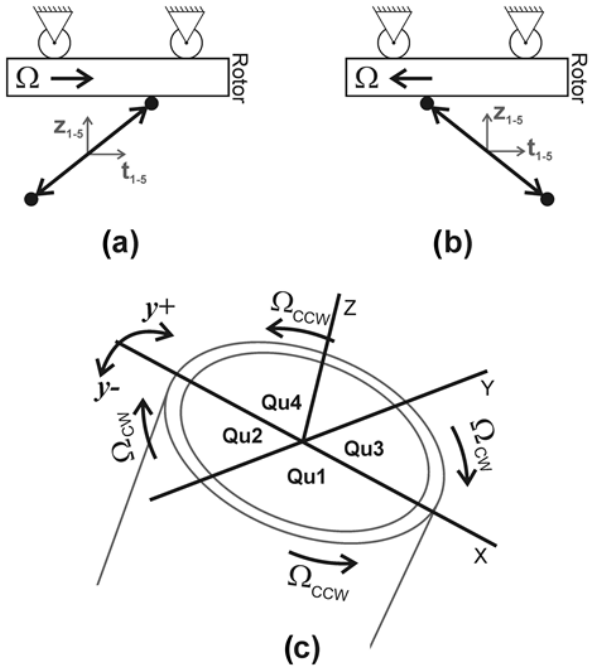

Figure 2.3 - Reciprocating diagonal motion during bending vibration along X axis [41]. (a) CCW direction rotation from points in Qu1 and Qu4. (b) CW direction rotation from points in Qu2 and Qu3. (c) Direction of rotation for each quadrant.

Both the upper and lower ends of the tube have same trajectories due to the symmetry of geometry when the tube vibrates in a first bending mode. The points on the upper and lower ends of the tube have same tangential trajectories on the corresponding quadrants. Therefore, pressing the rotor on corresponding quadrants of the upper and lower ends of the tube can rotate the rotor in the same direction. Teeth designs are required to ensure that the rotors are in contact with only desired points on the end of the tube. One way to realize this is to cut notches on the ends of the tube to form PZT teeth. Another way is to attach metal pieces on the end of the tube to form extended metal teeth. In the case of using metal teeth, the teeth are to be electrically isolated from the outer electrodes of the PZT tube. A spring with a preload is used to press the

rotor on one end of the tube while the other rotor is bonded to the shaft. The two motor designs are shown in Figure 2.4. PZT teeth motor consists of lower and upper rotor, PZT tube with PZT teeth, spring, clamp, and shaft. Metal teeth motor consists of lower and upper rotor, PZT tube with added metal teeth, spring, clamp, and shaft.

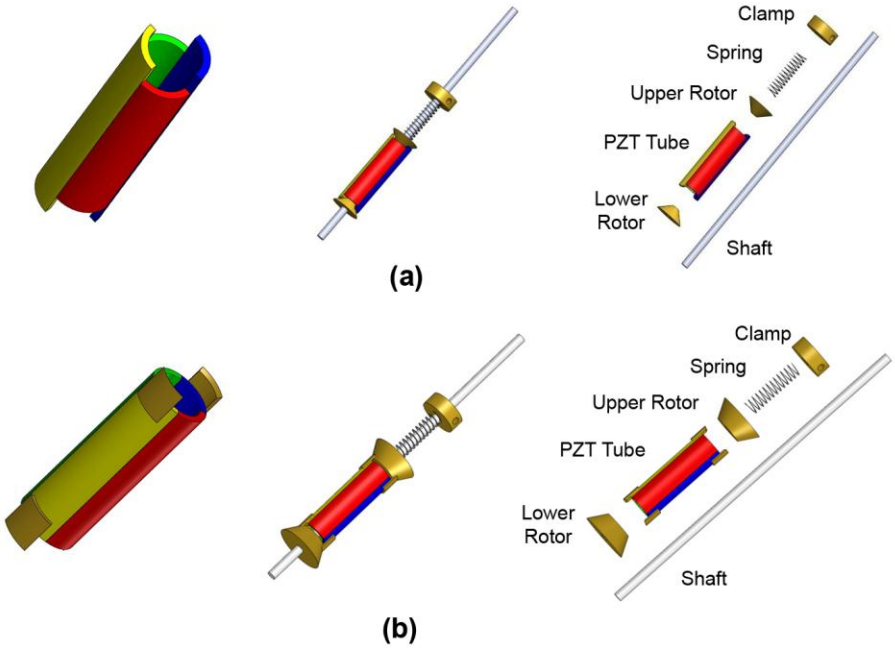

Figure 2.4 - Ultrasonic motor designs with teeth [41]. (a) PZT teeth motor. (b) Metal teeth motor.

2.2.4 Bi-directional rotor rotation

The rotation direction of the rotor can be changed by controlling the bending vibration direction of the PZT tube. The pairing combination of the exterior electrodes determines the bending vibration along X or Y axis. When teeth are placed on quadrants Qu1 and Qu4 so that the rotors are pressed only on those two quadrants, bending vibration along X axis can generate a counter-clockwise rotation but along Y axis can generate a clockwise rotation. The trajectories

of the points on the tube endpoints during bending vibration along Y axis are shown in Figure 2.5. Note that the axes X, Y, Z, and r_1, r_2, r_3, r_4, r_5 and t_1, t_2, t_3, t_4, t_5 are referenced to the resting position of PZT tube.

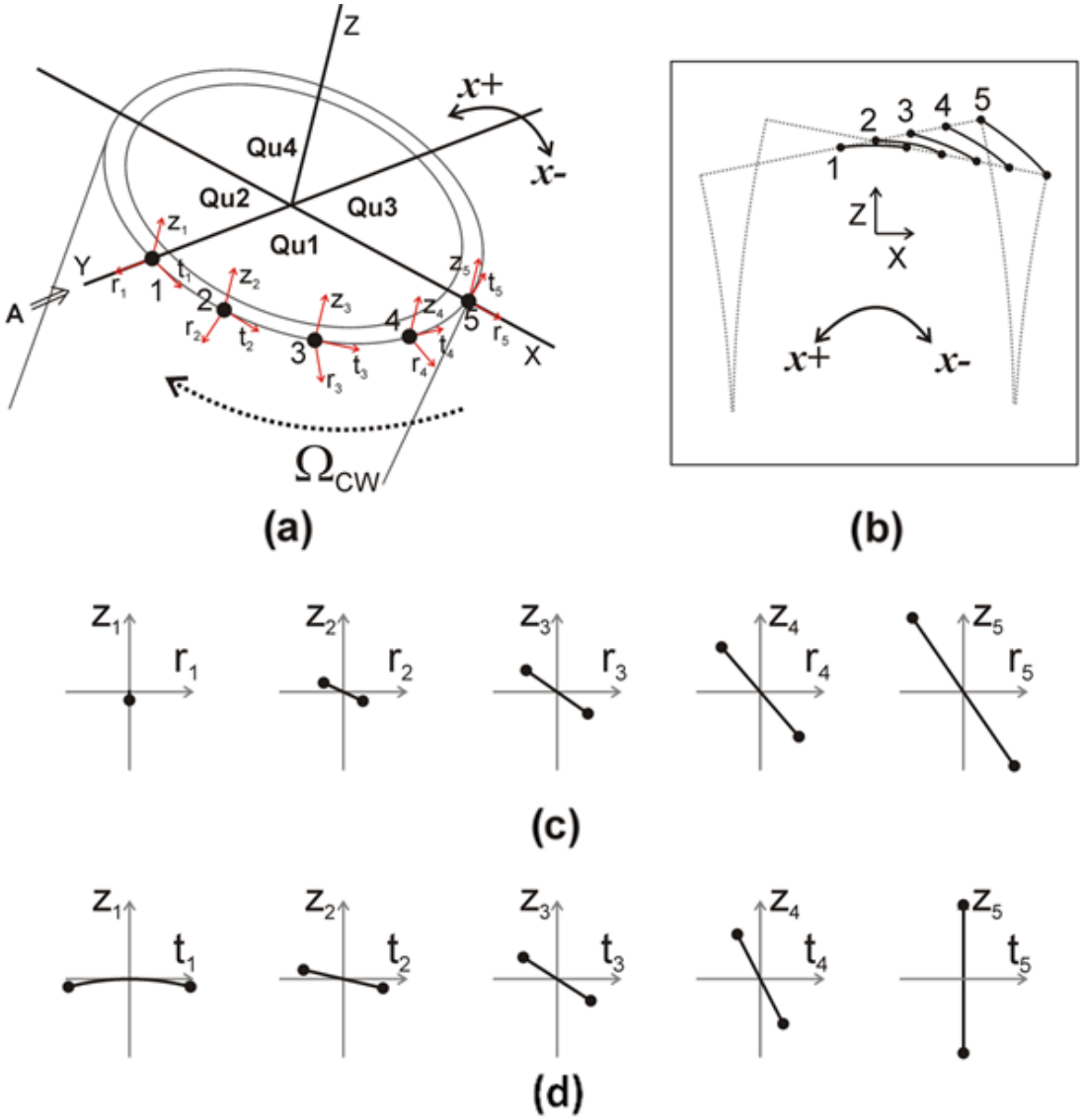

Figure 2.5 – The trajectories of the tube end points during a bending vibration along Y axis [41]. (a) Four quadrants and selected five points in Qu1. (b) Trajectories of selected points. (c) Radial components. (d) Tangential components.

2.3 Prototypes and experimental testing

2.3.1 PZT teeth prototype

2.3.1.1 Prototype description

A prototype of the piezoelectric ultrasonic motor with PZT teeth is shown in Figure 2.6. The PZT tube is from Sensor Technology Limited, BM527. Properties of the PZT used are listed in Table 2.1. The dimensions of the PZT tube are an outer diameter of 6.6 mm, an inner diameter of 5.0 mm, and length of 25.4mm. Two notches are cut on each ends of the tube to form four PZT teeth as shown. Two conical brass rotors are pressed on each end of the tube by a spring with a preload of 0.5 N applied to one rotor on one end while bonding the other rotor to the shaft on the other end. On the outer surface of the PZT tube, four individual electrodes divide the tube in four quadrants while leaving the inner surface of the tube in one continuous electrode. Four wires are soldered onto the outer electrodes and epoxy glue is put on to securely hold the solder.

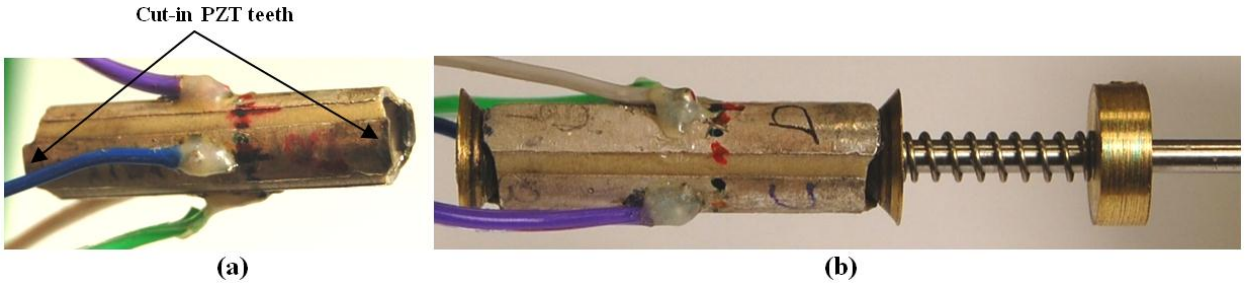

Figure 2.6 - Prototype of the ultrasonic motor with PZT teeth [41]. (a) PZT tube with teeth. (b) Motor assembly.

Table 2.1 - Properties of PZT.

d_{31} (C/N)	k_{31}	Mechanical Quality Factor, Q
2.15E-10	0.37	70

2.3.1.2 Frequency response

The two natural resonant frequencies of bending mode vibrations about the principle axes, L-axis and L'-axis are found using ANSYS. Figure 2.7 shows the simulation result of the two frequencies found at 27.76 kHz and 28.03 kHz. However, it is important to note that the two bending modes found using ANSYS are not the desired mode shapes for the operation of the ultrasonic motor. In order to drive the motor, the bending vibration must be along the X-axis or Y-axis. Pairing of the electrodes AB and DC excites bending vibration along Y-axis while pairing of AD and BC excites bending vibration along X-axis. Although the required bending vibration modes along X-axis or Y-axis are not about the principle axes, they are still the dominant modes due to the small mass and small inertia of the teeth and the driving frequency being not so close to the natural resonant frequency.

A scanning laser vibrometer is used to measure the frequency response of the assembled motor. Three natural resonant frequencies are identified in the range of 15 kHz ~ 40 kHz, as shown in Figure 2.8. The first bending mode vibration frequency measured with the laser scanning vibrometer is at 29.85 kHz which is higher than the ANSYS simulation results of 27.76 kHz and 28.03 kHz. This is due to the increased overall stiffness of the assembly by adding rotors and compressing them with a preloaded spring force.

The working frequency of the assembled ultrasonic motor is determined by testing the performance of the motor. A driving signal in the frequency range of 20 kHz ~ 40 kHz is applied to the paired electrodes (AB and DC, or AD and BC) while the no-load rotating speed is monitored. The frequency at where the speed is at maximum is selected as the working frequency, which is 27.6 kHz.

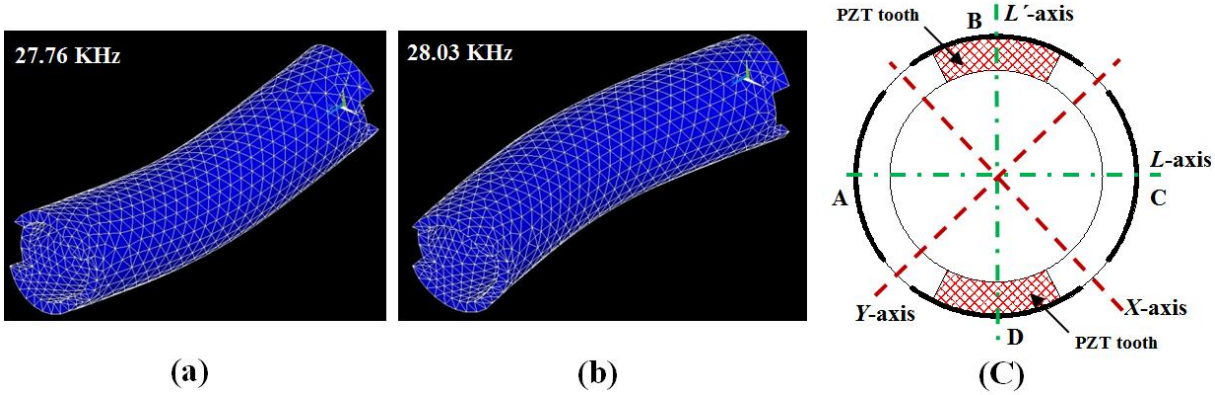

Figure 2.7 - ANSYS results of natural resonant frequencies of bending mode vibrations about the principle axe for PZT teeth motor [41]. (a) First mode at 27.76 kHz. (b) Second mode at 28.03 kHz. (c) Principle axes and (L and L') driving axes for the motor (X and Y).

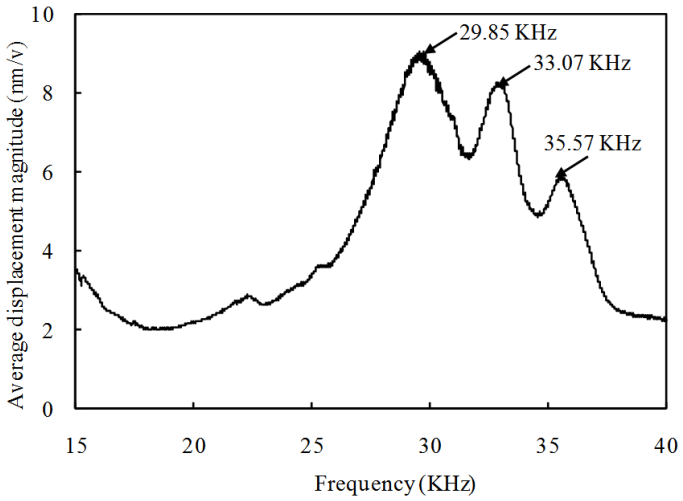

Figure 2.8 - Scanning laser vibrometer measurement of frequency response of the assembled motor [41].

2.3.1.3 Bending mode measurement

In the previous section, it is mentioned that the driving bending mode vibration is along the non-principle axes. It can be verified using a bending mode measurement with a laser scanning vibrometer. The assembled motor is driven with a sinusoidal signal of ±6.25 V at the working frequency of 27.6 kHz while the out-of-plane displacement along the principle axes and non-principle axes are measured. The electrodes AB and CD are paired so that the PZT tube would vibrate in bending mode along the non-principle axis, which is the line between Electrode B and Electrode C. As shown in Figure 2.9, the line of measurement between Electrode C and Electrode D is much greater than that of between Electrode B and Electrode C. This verifies that the bending vibration is along the line between Electrode B and Electrode C. This concludes that at the working frequency of 27.6 KHz, the motor vibrates along non-principle axis.

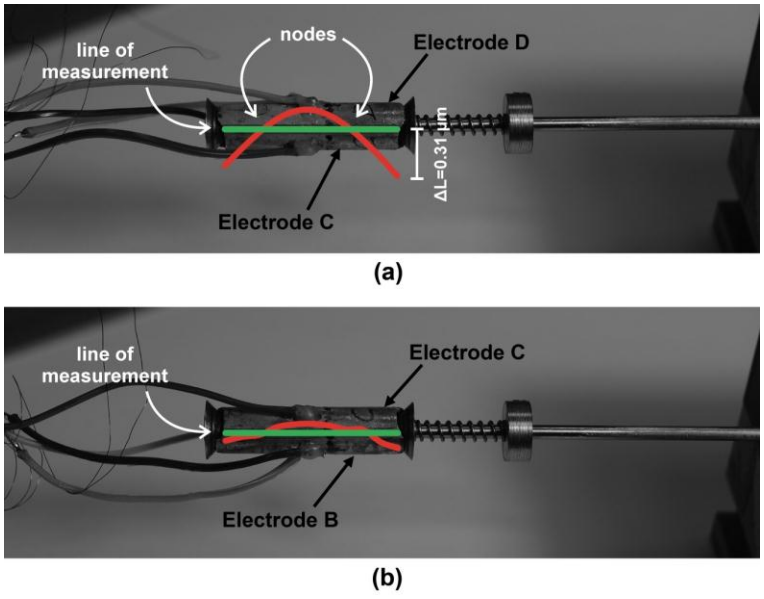

Figure 2.9 - Bending vibration measurement of PZT teeth motor using laser scanner vibrometer [41]. (a) Measurement along the principle axis. (b) Measurement along the non-principle axis.

2.3.1.4 Motor performance

A motor performance testing apparatus is setup as shown in Figure 2.10. A ball bearing is put in a perforated metal plate where the shaft of the assembled motor is put in. A fine string is used to carry weights for load testing of the motor. The motor is suspended with fixing the wires soldered on the outer surface of the PZT tube with tape. At a working frequency of 27.6 kHz and a signal magnitude of ±50 V, the speed and torque is measured. The rotation speed is measured by counting the number of revolutions a flag on the shaft has rotated in a fixed period of time of 10 seconds. A video camera is used to record and play in slow motion when it is too fast to count by eye. Torque is calculated by measuring the weight the motor can carry and the radius of the shaft. Starting from a no-load, a set of weights are added until the motor stops rotating. Bolts and nuts are used as weights which are tied to the string. As the motor pulls up the weights, rotation speed is measured and torque is calculated. The PZT teeth motor performs at a no-load speed 420 RPM with a stall torque of 254.5 μNm in clockwise direction, a no-load speed of 468 RPM with a stall torque of 296.0 μNm in counter-clockwise direction. The applied loads and number of rotations of the shaft measured in 10 seconds period for each step with the calculated speeds and torques are shown in Table 2.2 and Table 2.3 for both clockwise and counter-clockwise directions. The rotation speed versus torque plot is shown in Figure 2.11.

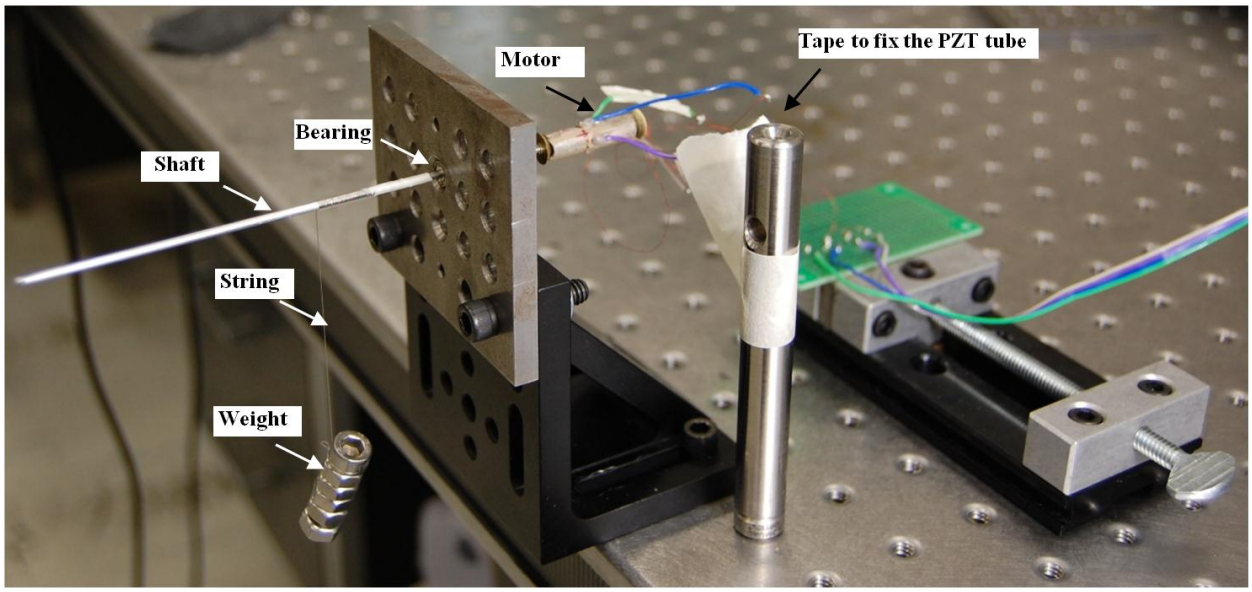

Figure 2.10 - Motor performance testing apparatus [41].

Table 2.2 - PZT teeth motor performance test results in counter-clockwise direction.

Clockwise Direction			
Load (mg)	Number of Rotations	Speed (RPM)	Torque (μNm)
0.000	70	420	0.0
10.054	55	330	98.6
12.149	53	318	119.2
14.263	48	288	139.9
16.468	45	270	161.6
18.608	42	252	182.5
20.763	34	204	203.7
25.938	0	0	254.5

Table 2.3 - PZT teeth motor performance test results in counter-clockwise direction.

Counter-Clockwise Direction			
Load (mg)	Number of Rotations	Speed (RPM)	Torque (μNm)
0.000	78	468	0.0
10.054	59	354	98.6
12.149	53	318	119.2
14.263	49	294	139.9
16.468	43	258	161.6
18.608	41	246	182.5
20.763	39	234	203.7
25.938	30	180	254.5
28.045	23	138	275.1
30.175	0	0	296.0

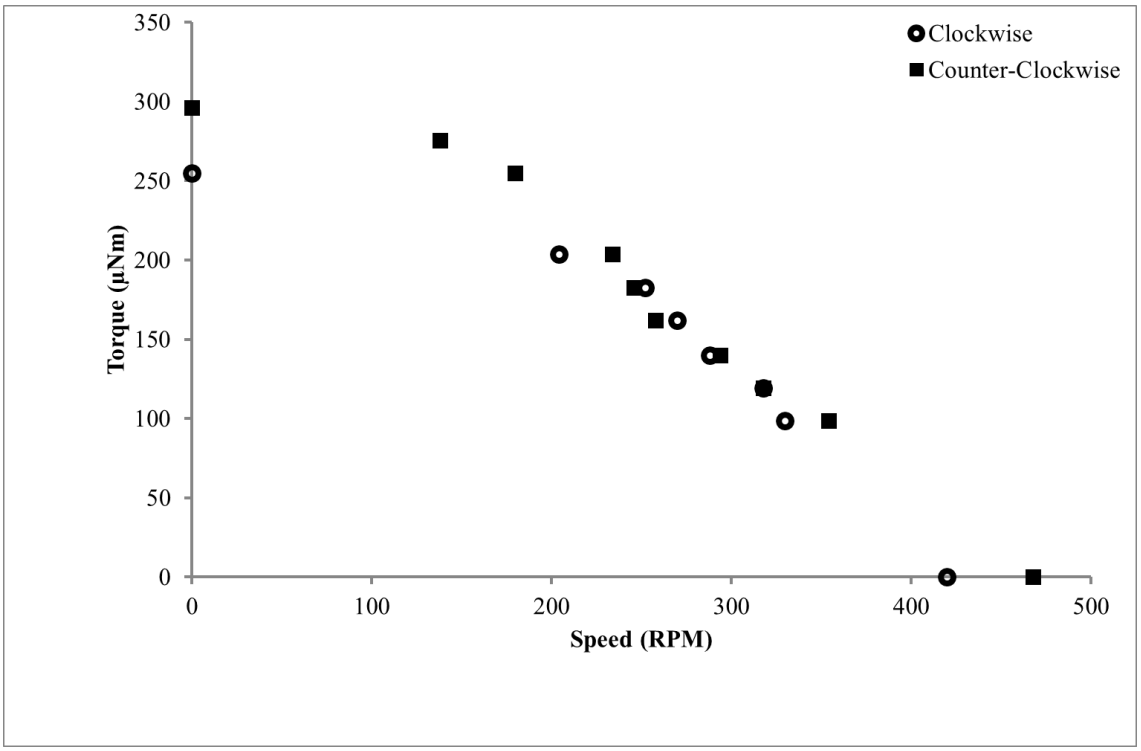

Figure 2.11 - Torque versus rotation speed plot of PZT teeth motor.

2.3.2 Metal teeth motor prototype

2.3.2.1 Prototype description

Instead of cutting notches to make PZT teeth as previous prototype, another prototype of ultrasonic motor with metal teeth attached are fabricated as shown in Figure 2.12. The dimensions and properties of the PZT tubes are the same as the previous prototype. Brass material is used for the metal teeth and they are electrically isolated from the outer surface electrodes by stripping off the electrodes at where the teeth are bonded to. Bigger sizes of rotors are prepared for this prototype as bigger teeth are used. Same pre-compression load of 0.5 N is applied to one of the rotor onto the spring while the other rotor is bonded to the shaft.

Figure 2.12 - Metal teeth motor prototype [41]. (a) PZT tube with four metal teeth. (b) Motor assembly.

2.3.2.2 Frequency response

ANSYS software is used for vibration simulation to find natural resonant frequencies for bending modes. The first and second natural frequencies are 23.77 kHz and 24.56 kHz along the principle axes of L-axis and L'-axis as shown in Figure 2.13. This frequency is compared to the experimental results using the laser scanner vibrometer for a frequency scan in the range of 15 kHz ~ 40 kHz. From the laser scanner vibrometer results, three natural resonant frequencies are

identified as shown in Figure 2.14. The frequencies identified from the experimental method are higher than simulation results due to the preload of spring force which increases the overall stiffness.

Same as PZT teeth motor, the desired frequencies are not along the principle axes, rather along the non-principle axes of X-axis and Y-axis. The actual working frequency for the bending vibration mode shape is determined by a frequency sweep of the motor to find at which frequency the motor has the maximum speed in between 15 kHz ~ 40 kHz. It is determined that the working frequency of the metal teeth motor is 23.5 kHz.

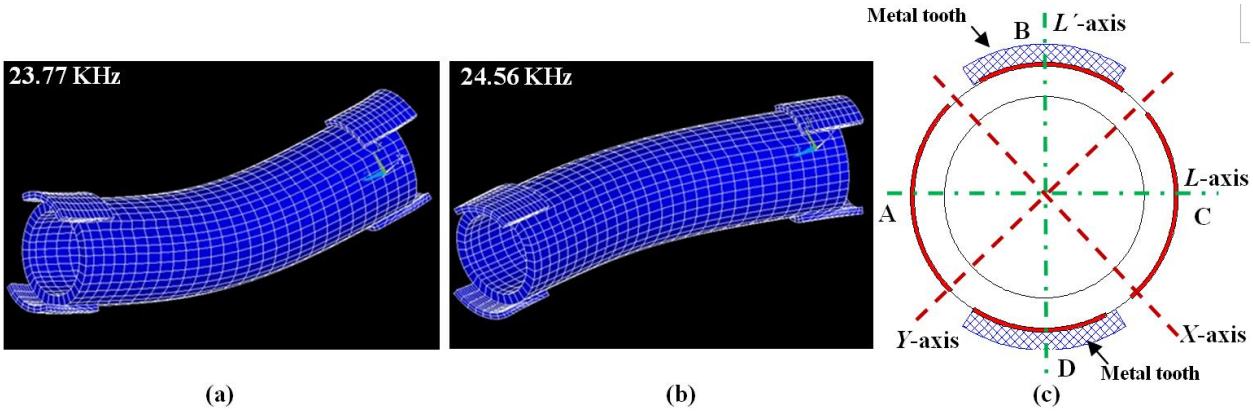

Figure 2.13 - ANSYS results of natural resonant frequencies of bending mode vibrations about the principle axes for metal teeth motor [41]. (a) First mode at 23.77 kHz. (b) Second mode at 24.56 kHz. (c) Principle axes and (L and L') driving axes for the motor (X and Y).

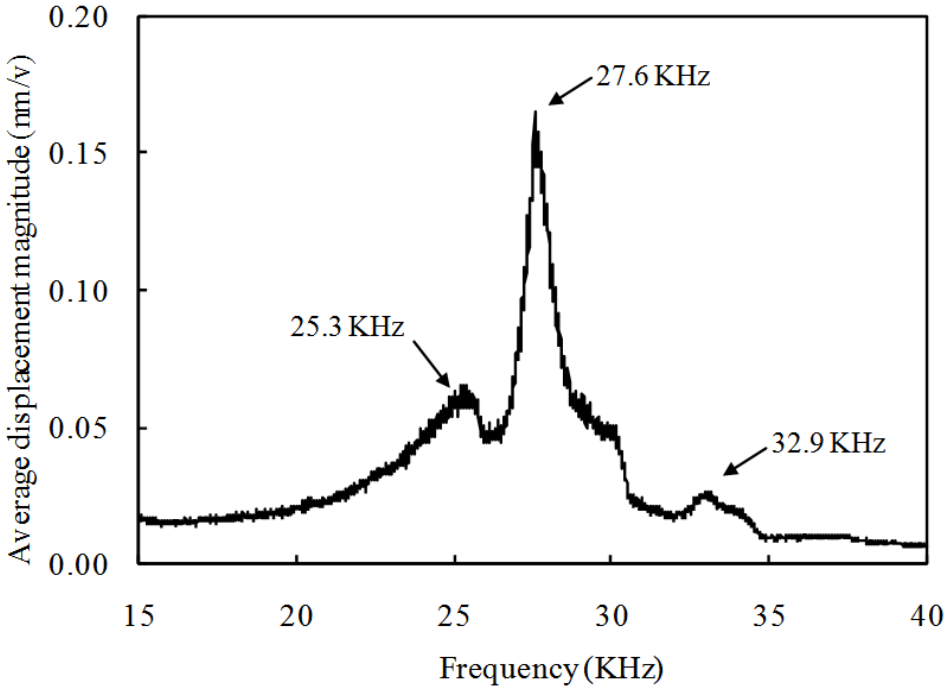

Figure 2.14 - Scanning laser vibrometer measurement of frequency response of the assembled metal teeth motor [41].

2.3.2.3 Bending mode measurement

Same as the PZT teeth motor, the bending mode of the metal teeth motor is measured using the laser scanner vibrometer in order to verify that the vibration is along the non-principle axes. The metal teeth motor is driven with a voltage magnitude of ±6.25V at the working frequency of 23.5 kHz. Similar to the PZT teeth motor, the bending mode measurement shows that the out-of-displacement along the principle axis (line between Electrode B and Electrode C) is much greater than that along the non-principle axis (line between Electrode A and Electrode B) as shown in Figure 2.15. This verifies that the vibration is along the non-principle axis.

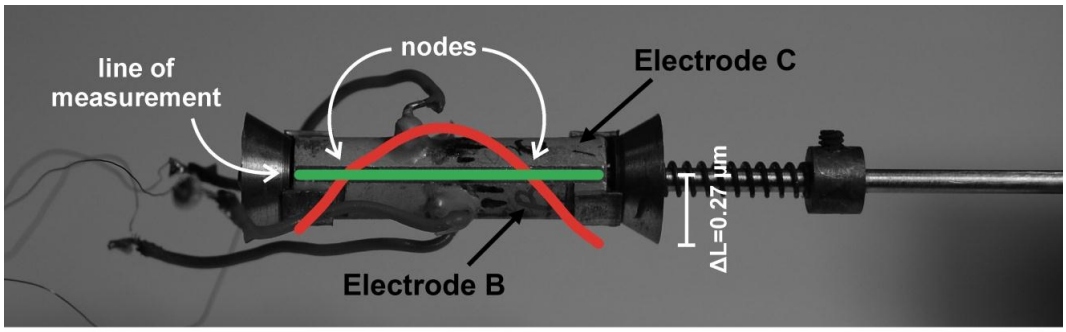

(a)

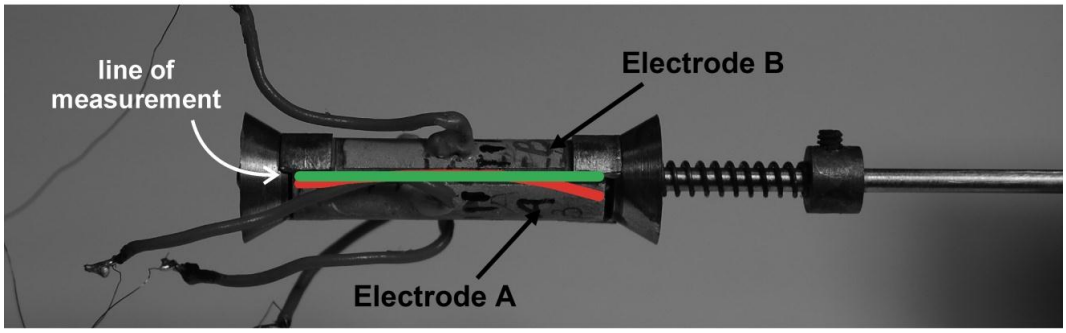

(b)

Figure 2.15 - Bending vibration measurement of metal teeth motor using laser scanner vibrometer [41]. (a) Measurement along the principle axis. (b) Measurement along the non-principle axis.

2.3.2.4 Motor performance

Using the same setup apparatus as the PZT teeth motor, the metal teeth motor prototype performance has been tested. With a driving voltage of ±50 V and at a working frequency of 23.5 kHz, the motor can achieve a no-load speed of 378 RPM and a stall torque of 296.0 μNm in clockwise direction and a no-load speed of 420 RPM and a stall torque of 254.5 μNm. The measurements and calculation results are listed in Table 2.4 and Table 2.5 for both clockwise direction and counter-clockwise direction. The rotation speed versus torque plot is shown in Figure 2.16.

Table 2.4 - Metal teeth motor performance test results in clockwise direction.

Clockwise Direction			
Load (mg)	Number of Rotations	Speed (RPM)	Torque (μNm)
0.000	63	378	0.0
10.054	44	264	98.6
12.149	41	246	119.2
14.263	40	240	139.9
16.468	39	234	161.6
18.608	38	228	182.5
20.763	36	216	203.7
25.938	25	150	254.5
28.045	17	102	275.1
30.175	0	0	296.0

Table 2.5 - Metal teeth motor performance test results in counter-clockwise direction.

Counter-Clockwise Direction			
Load (mg)	Number of Rotations	Speed (RPM)	Torque (μNm)
0.000	70	420	0.0
10.054	53	318	98.6
12.149	50	300	119.2
14.263	48	288	139.9
16.468	46	276	161.6
18.608	45	270	182.5
20.763	43	258	203.7
25.938	0	0	254.5

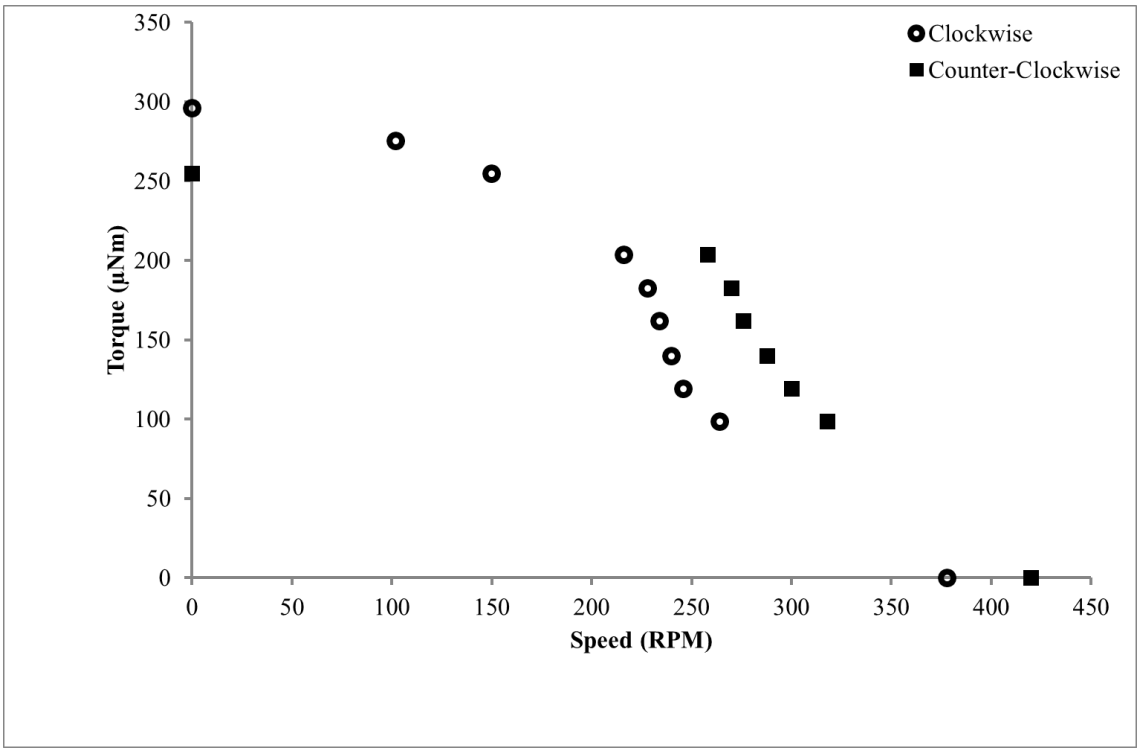

Figure 2.16 - Torque versus rotation speed plot of metal teeth motor.

2.4 Analytical model

2.4.1 Introduction

This section of the chapter reports the analytical modeling of the piezoelectric ultrasonic motors. The analytical models presented in this section are generalized models targeted for piezoelectric cylindrical tubes. The purpose of this section is to find mathematical models and to verify that the models can be applied towards the ultrasonic motor designs presented in this chapter. There are three models introduced in this section. First model is the static analysis which calculates the axial stress for the purpose of analyzing the durability of the motor due to the bending moment. Second model is the displacement analysis which calculates the maximum

deflection of the tip of the piezoelectric cylindrical tube. Third model is the vibrational analysis which uses the results from the displacement analysis and calculates the rotation speed of the motor. The static analysis is from Ma, et al. [45], the displacement analysis model is from Yang and Huang [46], and the vibrational analysis model is from Lu, et al. [47]

2.4.2 Static analysis

In static analysis, the axial stress on the piezoelectric tube caused by the bending moment is analyzed and compared with the yield strength to determine the safe working range of applied voltage until yield occurs. For static analysis, one end of the piezoelectric cylindrical tube is to be clamped on one end while the other end is to remain free of any constraints. When a certain voltage is applied onto the outer surface of the hollow cylinder where electrodes are coated while the inner surface of the hollow cylinder is grounded, the tube is assumed to be subjected to a pure bending. A pure bending is defined that the cross section of the cylindrical actuator perpendicular to its longitudinal axis remains plane and perpendicular to the longitudinal axis after the deformation. A quarter of the tube is shown in Figure 2.17 when the deflection occurs as negative voltage is applied onto the outer surface while inner surface is grounded.

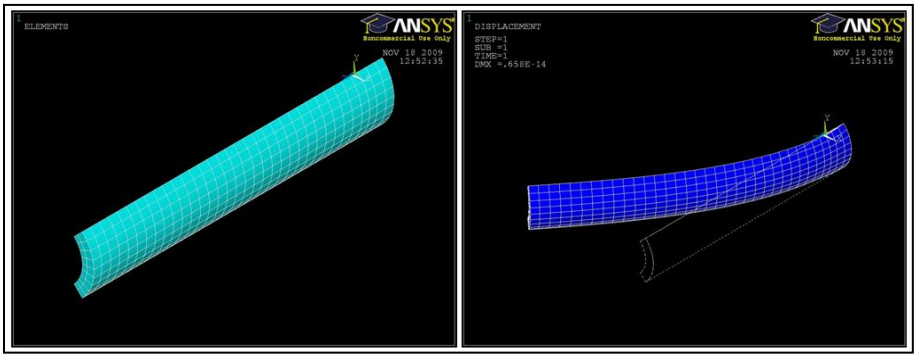

Figure 2.17 - Static deflection of quarter of a PZT tube.

When the tube is subjected to a pure bending, all other components of stress and strain can be neglected except for the axial component of stress T1 and strain S1. This axial component of stress can be represented as maximum tensile or compressive stress with same magnitude depending on the location from the neutral axis. The piezoelectric equation for the axial component of stress and strain is the following where s_{11}^{E} and d_{31} are piezoelectric constants and E_3 is the voltage applied

$$S_1 = s_e + s_p = s_{11}^{E} T_1 + d_{31} E_3 \tag{2.1}$$

Term s_e represents the strain induced by external force and s_p represents strain induced by electric field.

Using thin wall approximation since the thickness of the stator is 1mm and from Gauss' Law, the expression of the electric field at a distance from the centre of the cube can be written

$$E_r = \frac{-V}{r\, ln(1-\propto)} \tag{2.2}$$

$$\propto = \frac{t}{R_o} \tag{2.3}$$

where V is the applied voltage and α is the aspect ratio between the thickness and outer radius of the stator tube. By defining a reference value of electric intensity as following

$$E_{ref} = \frac{V}{t} \tag{2.4}$$

the electric field equation above can be written with respect to the reference value of electric intensity as the following equation

$$E_r = \frac{-tE_{ref}}{r\,ln(1-\propto)} \tag{2.5}$$

where the reference value of electric intensity depends on how the voltage is applied onto the tube.

When the voltage is applied according to the Figure 2.18, the reference value of electric intensity can be represented as the followings.

$$E_{ref}(\theta) = \begin{cases} \frac{V_x}{t}, \theta \in \left[-\frac{\pi}{4}, \frac{\pi}{4}\right] \\ \frac{V_y}{t}, \theta \in \left[\frac{\pi}{4}, \frac{3\pi}{4}\right] \\ \frac{V_{-x}}{t}, \theta \in \left[\frac{3\pi}{4}, \frac{5\pi}{4}\right] \\ \frac{V_{-y}}{t}, \theta \in \left[\frac{5\pi}{4}, \frac{7\pi}{4}\right] \end{cases} \tag{2.6}$$

The piezoelectric axial force and bending moments of the cylindrical piezoelectric tube shown in Figure 2.18 are as follows

$$F_z = \int_0^{2\pi} \int_{R_i}^{R_o} ES_p\, r dr d\theta \tag{2.7}$$

$$M_{xz} = \int_{-\pi/4}^{\pi/4} \int_{R_i}^{R_o} ES_p\, r\cos\theta\, r dr d\theta + \int_{3\pi/4}^{5\pi/4} \int_{R_i}^{R_o} ES_p\, r\cos\theta\, r dr d\theta \tag{2.8}$$

$$M_{yz} = \int_{\pi/4}^{3\pi/4} \int_{R_i}^{R_o} ES_p\, r\sin\theta\, r dr d\theta + \int_{5\pi/4}^{7\pi/4} \int_{R_i}^{R_o} ES_p\, r\sin\theta\, r dr d\theta \tag{2.9}$$

where E is the Young's modulus of piezoelectric material and s_p is the strain induced by electric field. The reference value of electric intensity along the four quadrants can be represented by the following equations.

$$\mathrm{E_{ref\,x}} = \frac{\mathrm{V_{xz}}}{\mathrm{t}} = \frac{\mathrm{V_x - V_{-x}}}{\mathrm{2t}} \tag{2.10}$$

$$E_{ref\,y} = \frac{V_{yz}}{t} = \frac{V_y - V_{-y}}{2t} \tag{2.11}$$

$$E_{ref\,z} = \frac{V_z}{t} = \frac{V_x + V_{-x} + V_y + V_{-y}}{4t} \tag{2.12}$$

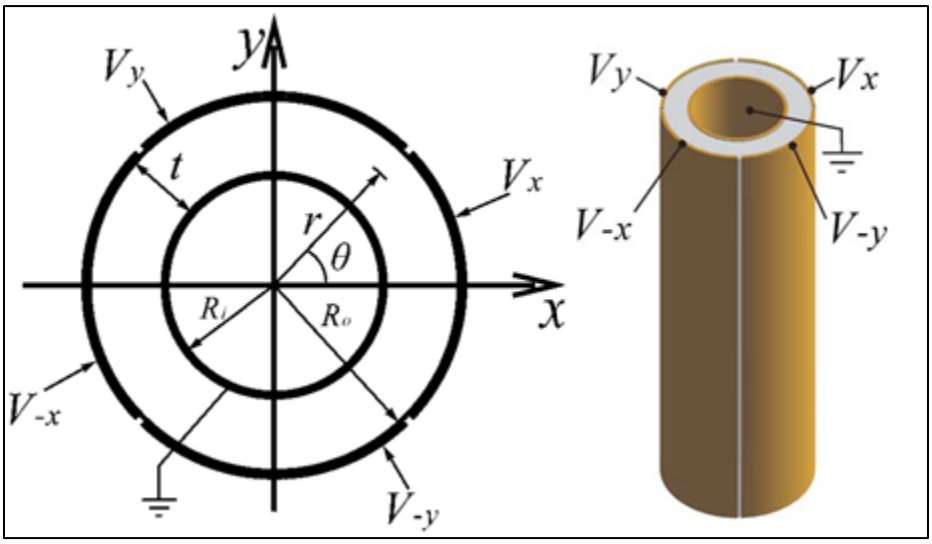

Figure 2.18 - Piezoelectric tube with applied voltages [45].

Substituting the parameters and solving the double integral formula above for the axial force and bending moment equations, the equations become the followings.

$$F_z = -\frac{2\pi(\alpha)^2}{ln(1-\alpha)} E d_{31} E_{ref\,z} {R_o}^2 \tag{2.13}$$

$$M_{xz} = -\frac{\alpha^2(2-\alpha)}{ln(1-\alpha)} \sqrt{2} E d_{31} E_{ref\,x} {R_o}^3 \tag{2.14}$$

$$M_{yz} = -\frac{\alpha^2(2-\alpha)}{ln(1-\alpha)} \sqrt{2} E d_{31} E_{ref\,y} {R_o}^3 \tag{2.15}$$

These equations can be used to calculate the axial force and bending moments of the stator for static analysis. The bending moments can be used to calculate the normal stress when

it the electricity is applied to the electrodes of the stator. When the electrodes in x and y directions are excited at the same magnitude of voltages while the inner electrode is grounded, $E_{ref\,z}$ becomes 0 and $E_{ref\,x}$ is equal to$E_{ref\,y}$. Therefore, the axial force F_z becomes 0 while the magnitude of bending moments in x and y directions are equal to each other, M_{xz}=M_{yz}. When ±50 volt is applied on x and y direction and the opposite side of the electrodes are kept floating while the inner electrodes are grounded, the bending moments are calculated to be the followings.

$$M_{xz} = M_{yz} = 0.0139 \text{ MPa} \tag{2.16}$$

Using the flexural formula, the normal stress can be calculated.

$$\sigma_{N1} = \frac{F_Z}{A} + \frac{M_{xz}y}{I_x} \tag{2.17}$$

$$\sigma_{N2} = \frac{F_Z}{A} + \frac{M_{yz}x}{I_y} \tag{2.18}$$

When same magnitude of voltages are applied onto x any y surfaces and due to the geometry,

$$V_x = V_y \tag{2.19}$$

$$x = y \tag{2.20}$$

then,

$$F_z = 0 \tag{2.21}$$

$$M_{xz} = M_{yz} \tag{2.22}$$

therefore, the equation for finding the normal stress becomes the following.

$$\sigma_N = \frac{M_{xz}y}{I_x} = \frac{M_{yz}x}{I_y} \tag{2.23}$$

The normal stress σ_N on the prototype design is shown in Table 2.6. This value is compared to the yield strength of the PZT to validate the deformation is within the yield limit. The yield strength of a typical PZT material is 250 MPa, however compressive stress should not exceed 20% of that value. Considering the fact that the applied stress in tension should be only approximately 10% of the compressive limit, the tensile stress should not exceed 5 MPa. Comparing the two prototype designs with the limit, the Safety Factor is calculated and shown in Table 2.6.

Table 2.6- Results of static analysis.

σ_N (MPa)	Y x 10% (MPa)	S.F.
0.56	12.5	2.02

For next step, the maximum voltage which will cause yield in PZT tube is calculated. The maximum voltage which will create 5 MPa of tensile strength for the prototype design is 450 V. However it is not recommended to apply such high voltage since the PZT is known to fail due to high electric field before the stress reaches its yield limit.

2.4.3 Displacement analysis

In displacement analysis, the deflections of the piezoelectric cylindrical tube in radial directions are analyzed. The displacement on the tip while the one end is fixed is calculated and to be used in following Vibrational Analysis to calculate the rotation speed of the rotor attached to the piezoelectric stator. A fixed-free boundary condition is assumed for calculation and the teeth design is not included in the modeling. Since the teeth design is not considered, both prototype designs are considered identical and only one model is carried out through the analysis.

The cylindrical beam is placed in vertical direction and the bottom end is clamped to create fixed-free boundary condition as shown in Figure 2.19. The applied voltages on the tube on both PZT teeth motor and metal teeth motor and are listed in Table 2.7.

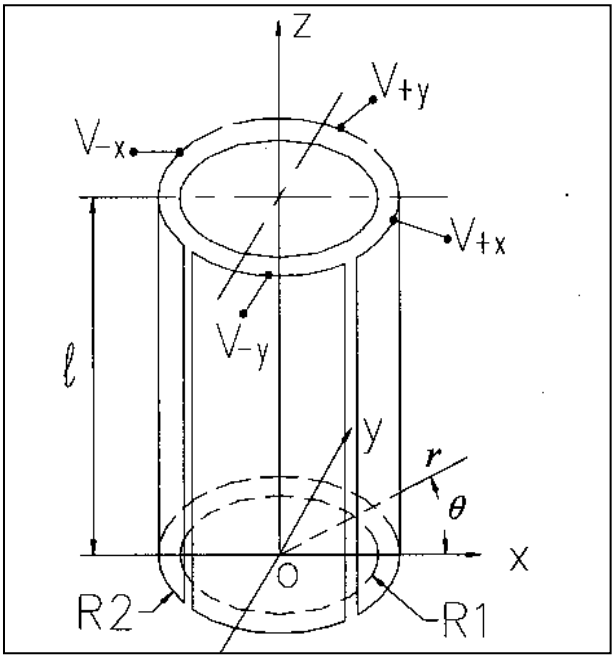

Figure 2.19 - Piezoelectric tube geometry with applied voltages [46].

Table 2.7 - Voltages applied on prototype design.

V_x (V)	V_{-x} (V)	V_y (V)	V_{-y} (V)	V_z (V)
±50	0	±50	0	0

According to the operation of piezoelectric cylindrical tube, all other components of stress and strain other than the axial component of stress T1 and strain S1 can be neglected. Also, according to the theory of elasticity, the stress and strain do not vary along a line parallel to the axial direction, in this case z axis. The displacement of a cross section includes three independent components including the translation displacement in z axis and two rotary displacements along the x and y axis. This can be shown in the equation following which relates the axial component of strain with the radius of curvatures in x and y direction are represented as a and b respectively while c represents the translation in z axis.

$$S_1 = a r \cos\theta + b r \sin\theta + c \tag{2.24}$$

The radius of curvatures a, b and the axial translation c can be determined by the following boundary conditions of the piezoelectric tube which comes from the Static Analysis section; the resultant force and resultants moments at the tip end must be zero. This is shown as the following equations

$$\int_0^{2\pi} \int_{R_i}^{R_o} T_1 r \, dr \, d\theta = 0 \tag{2.25}$$

$$\int_0^{2\pi} \int_{R_i}^{R_0} T_1 r^2 \sin\theta \, dr \, d\theta = 0 \tag{2.26}$$

$$\int_0^{2\pi}\int_{R_i}^{R_o} T_1 r^2 \cos\theta \, dr \, d\theta = 0 \tag{2.27}$$

where, T_1 is axial components of stress and R_o and R_i are outer and inner radius of the tube.

Piezoelectric constitutive equation is

$$S_1 = s_{11}^E T_1 + d_{31} E_3 \tag{2.28}$$

as it is shown in Static Analysis. When the piezoelectric tube is divided uniformly into four quadrants with individual electrodes on each quadrant, the electric field can be represented as

$$E_3(\theta) = \begin{cases} \frac{(V_{+x}+V_z)}{t}, \theta \in \left[-\frac{\pi}{4}, \frac{\pi}{4}\right] \\ \frac{(V_{+y}+V_z)}{t}, \theta \in \left[\frac{\pi}{4}, \frac{3\pi}{4}\right] \\ \frac{(V_{-x}+V_z)}{t}, \theta \in \left[\frac{3\pi}{4}, \frac{5\pi}{4}\right] \\ \frac{(V_{-y}+V_z)}{t}, \theta \in \left[\frac{5\pi}{4}, \frac{7\pi}{4}\right] \end{cases} \tag{2.29}$$

where V_x and V_y are voltages applied on two quadrants in x and y direction respectably, and V_z is the voltage applied on the inner electrode which is grounded in this case.

The equations for calculating the radius of curvature and axial deformation are the following.

$$a = \frac{4\sqrt{2}\left({R_o}^3 - {R_i}^3\right)}{3\pi\left({R_o}^4 - {R_i}^4\right)} \frac{(V_{+x} - V_{-x})}{t} d_{31} \tag{2.30}$$

$$b = \frac{4\sqrt{2}\left({R_o}^3 - {R_i}^3\right)}{3\pi\left({R_o}^4 - {R_i}^4\right)} \frac{(V_{+y} - V_{-y})}{t} d_{31} \tag{2.31}$$

$$c = \frac{d_{31}}{t}\left(\frac{V_{+x} - V_{-x}}{4} + \frac{V_{+y} - V_{-y}}{4} + V_z\right) \tag{2.32}$$

Using the small displacement theory, the deflection on the free end of cantilever is approximately

$$\Delta\zeta = \frac{kL^2}{2} \tag{2.33}$$

where L is the length of the beam and k is the curvature. Using the above equation with radius of curvatures of the stator in x and y direction, the deflection in the x and y direction can be calculated using the following equations.

$$u_x = \frac{aL^2}{2} = \frac{4\sqrt{2}\left({R_o}^3 - {R_i}^3\right)}{3\pi\left({R_o}^4 - {R_i}^4\right)} \frac{(V_{+x} - V_{-x})}{t} \frac{d_{31}L^2}{2} \tag{2.34}$$

$$u_y = \frac{bL^2}{2} = \frac{4\sqrt{2}\left({R_o}^3 - {R_i}^3\right)}{3\pi\left({R_o}^4 - {R_i}^4\right)} \frac{(V_{+y} - V_{-y})}{t} \frac{d_{31}L^2}{2} \tag{2.35}$$

Table 2.8 - Radial displacements of prototype design.

u_x (m)	u_y (m)
3.49e-6	3.49e-6

From the result, the deflection in x and y directions ux and uy are of same values. This is because the applied voltages in x and y directions are the same and due to the symmetrical geometry in x and y direction. The displacement values of each design are used in the following Vibrational Analysis for further analysis.

2.4.4 Vibrational analysis

In vibrational analysis, the kinematics of piezoelectric cylindrical tube stators is studied as the stators are subjected to bending vibration at resonant frequency. Continuing from the displacement analysis, the mode shapes and static deflection values are used to calculate the rotor speed for both designs.

This analysis is based on the working principle of piezoelectric rotary motor combining two fundamental bending modes in order to create traveling wave on the surface of the tube. This is done by applying voltages on the outer surfaces which is divided in four quadrants in 90 ° phase difference. The traveling wave drives the rotor in contact by frictional forces. The prototypes reported in this chapter use only one of the two fundamental bending modes in a standing wave which are combined to a travelling wave in this analysis. The analysis is carried on assuming the performance of the motor is the same for exciting the motor in standing wave or travelling wave since it is actuated at the same frequency and the amplitude of the excitation voltage of the analysis and experimental test are kept the same.

The beam bending model can be represented by Timoshenko beam theory as shown in the equation below where z is the axial direction, w is the displacement in radial direction, E, I, ρ are material properties. The reason for using this instead of Euler Bernoulli beam equation is because the geometry does not satisfy for Euler Bernoulli beam as the ratio between the axial and radial length is less than 10.

$$EI\frac{\partial^4 w}{\partial z^4} + \rho A\frac{\partial^2 w}{\partial t^2} - \rho I\left(1 + \frac{E}{\kappa G}\right)\frac{\partial^4 w}{\partial z^2 \partial t^2} + \frac{\rho^2 I}{\kappa G}\frac{\partial^4 w}{\partial t^2} = 0 \qquad (2.37)$$

$$\frac{L}{h_x} = \frac{L}{h_y} < 10 \tag{2.38}$$

The excitation of the beam is shown in Figure 2.20 below.

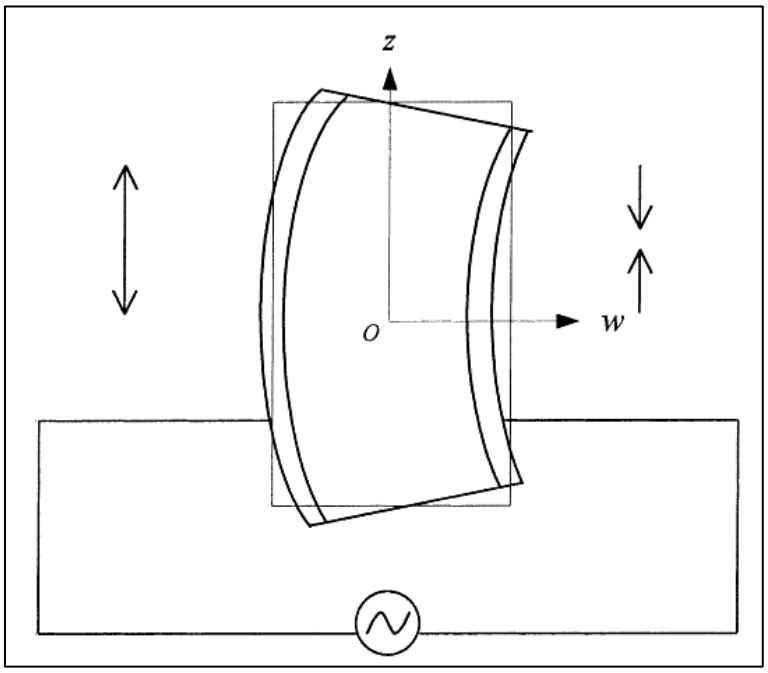

Figure 2.20 - Vibration Model of Piezoelectric Tube with Applied AC Voltage [47].

The geometric boundary conditions for free-free end beam are the followings.

$$\frac{\partial^2 w\left(\pm\frac{L}{2},t\right)}{\partial z^2} = 0 \tag{2.39}$$

$$\frac{\partial^3 w\left(\pm\frac{L}{2},t\right)}{\partial z^3} = 0 \tag{2.40}$$

Using these boundary conditions for solving the natural vibration frequencies ω_i and corresponding mode shapes $W_i(z)$ from eigenvalue solutions are as followings.

$$\omega_i = 2\pi f_i = \left(\frac{\propto_i}{L}\right)^2 \left(\frac{EI}{\rho A}\right)^{1/2} \left[1 - \frac{I}{2A}\left(\frac{\alpha_i}{L}\right)^2 \left(1 + \frac{E}{\kappa G}\right)\right] \quad (2.41)$$

$$W_i(z) = C_i \left(\sin\left(\frac{\propto_i}{2}\right)\cosh\left(\frac{\propto_i}{L}z\right) - \sinh\left(\frac{\propto_i}{2}\right)\cos\left(\frac{\propto_i}{L}z\right)\right) \quad (2.42)$$

For the cylindrical piezoelectric tube motor, the fundamental resonance frequency ω_1 at when the bending mode shape occurs W_1 is determined from the use of ANSYS program to be used in further calculations.

Two bending modes of same resonant frequency can be excited at the same time when the resonant frequency of electrical source is applied at 90˚ phase difference. This will generate two standing fundamental bending vibrations of the stator w_x and w_y. This will lead to generation of a traveling wave on the end surface of the stator in an elliptical trajectory.

Equations for two standing fundamental bending vibrations are the followings.

$$w_x = W_1(z)\cos(\omega_1 t) \quad (2.43)$$

$$w_y = W_1(z)\sin(\omega_1 t) \quad (2.44)$$

Radial and circumferential components of two vibrations are the following equations and the representation is shown in Figure 2.21 below.

$$w_r = w_x \cos\theta + w_y \sin\theta = W_1(z)\cos(\omega_1 t - \theta) \quad (2.45)$$

$$w_\tau = w_y \cos\theta - w_x \sin\theta = W_1(z)\sin(\omega_1 t - \theta) \quad (2.46)$$

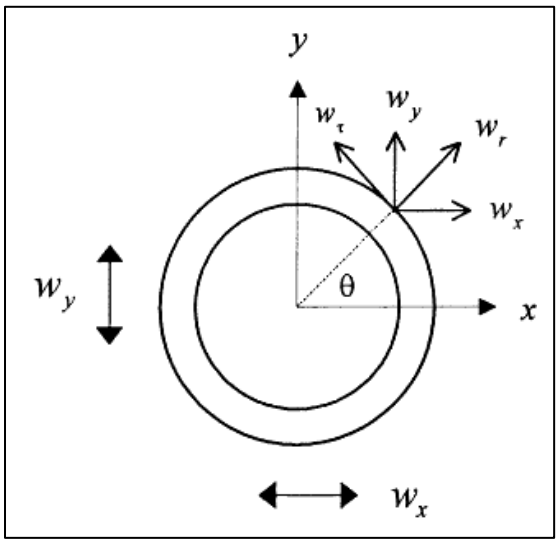

Figure 2.21 - Radial and Tangential Components of Displacements [47].

At an arbitrary point along the surface of the stator has a displacement, u, along the longitudinal direction due to the bending motion of the stator, w_x and w_y. Using superposition of the longitudinal displacement, u_x and u_y, this displacement can be represented by the following equations

$$u_x = -x\frac{\partial w_x}{\partial z} = -xW'_1(z)\cos(\omega_1 t) = -rW'_1(z)\cos\theta\cos(\omega_1 t) \quad (2.47)$$

$$u_y = -y\frac{\partial w_y}{\partial z} = -yW'_1(z)\sin(\omega_1 t) = -rW'_1(z)\sin\theta\sin(\omega_1 t) \quad (2.48)$$

$$u = u_x + u_y = -rW'_1(z)\cos(\omega_1 t - \theta) \quad (2.49)$$

where r is an arbitrary distance in radial direction from the centre of the stator.

Using the equation above, the motion components of point at θ on the end surface of the stator is represented by the following equations.

$$w_r\left(\frac{L}{2},t\right) = w_1\left(\frac{L}{2},t\right)\cos(\omega_1 t - \theta) \tag{2.50}$$

$$w_\tau\left(\frac{L}{2},t\right) = W_1\left(\frac{L}{2}\right)\sin(\omega_1 t - \theta) \tag{2.51}$$

$$u\left(\frac{L}{2},t\right) = -rW'_1\left(\frac{L}{2}\right)\cos(\omega_1 t - \theta) \tag{2.52}$$

Tangential velocity of the point on the end surface of the stator can be found by differentiating the tangential component of displacement.

$$v = \dot{w}_\tau = W_1\left(\frac{L}{2}\right)\omega_1\cos(\omega_1 t - \theta) \tag{2.53}$$

The equation for rotor velocity comes from relating the tangential velocity of the end tip with deflection. Assuming that there is no slipping between the rotor and the stator, the tangential velocity can be calculated by differentiating the tangential displacement at the tip of the end point of the piezoelectric stator. The velocity is at maximum value when, $|\cos(\omega_1 t - \theta)| = 1$. Therefore, the maximum tangential velocity of the contact point can be calculated from the following equation.

$$V = W_1\left(\frac{L}{2}\right)\omega_1 = 2\pi W_1\left(\frac{L}{2}\right)f_1 \tag{2.54}$$

The rotor velocity can be calculated by multiplying the tangential velocity with the rotor radius multiplied by 60 to convert the unit to RPM. The $W(L/2)$ in the below equation is the deflection on the tip of the stator. Assuming that the deflection from the vibration is

approximately same as the deflection from the static conditions, the value can be obtained from Displacement Analysis.

$$V_R = \frac{W\left(\frac{L}{2}\right)}{R_r} f_1 \times 60 \tag{2.55}$$

The rotor velocity of the prototype design is listed in Table 2.9. The value 395.52 RPM is close to the experimental no-load speed of the PZT teeth prototype design which is 378 RPM. Metal teeth prototype design has a no-load speed of 468 RPM. Percentage error of the speed difference between the PZT teeth motor and the analytical model and between the metal teeth motor and the analytical model are 4.4% and 15.5%, respectively. Considering the assumptions and teeth designs, the model can represent a rough estimation of a mathematical model of the piezoelectric ultrasonic motor.

Table 2.9 - Rotor velocity of the ultrasonic motor design.

	V_R (RPM)
Analytical Model	395.52
PZT Teeth Prototype	378
Metal Teeth Prototype	468

Chapter 3. Brass Tube Motor Design

3.1 Chapter introduction

In this chapter, a second iteration of piezoelectric ultrasonic motor is reported. This design is to address some of the issues with the previous designs and to improve on the motor performance in terms of rotation speed and torque. Reducing the overall size is another important factor considered. Same as the previous motor designs, this motor uses a single vibration bending mode of the stator for a rotation of the rotor with only one driving signal. The major difference is that the stator is made of a rectangular hollow brass tube with four pieces of rectangular PZT plates bonded on all four surfaces. Switching from the PZT tube to brass tube increases the durability of the motor as PZT material is known for its brittleness. Also, much higher amplitude of vibration can be achieved with brass tube since brass is much stronger material.

First part of this chapter describes the principle of operation of the second iteration of the prototype which is almost similar to the operating principle of the previous designs. Next part reports the prototype description and testing setup configurations. Last part of the chapter reports the motor performance test results.

3.2 Principle of operation

The standing wave brass-PZT square tube ultrasonic motor consists of two rotors, a shaft and a stator as shown in Figure 3.1. The stator is a brass square tube with four PZT plates

bonded onto its four outside walls. There are two teeth at the opposite corners of each end of the brass tube. Two rotors are pressed against the teeth.

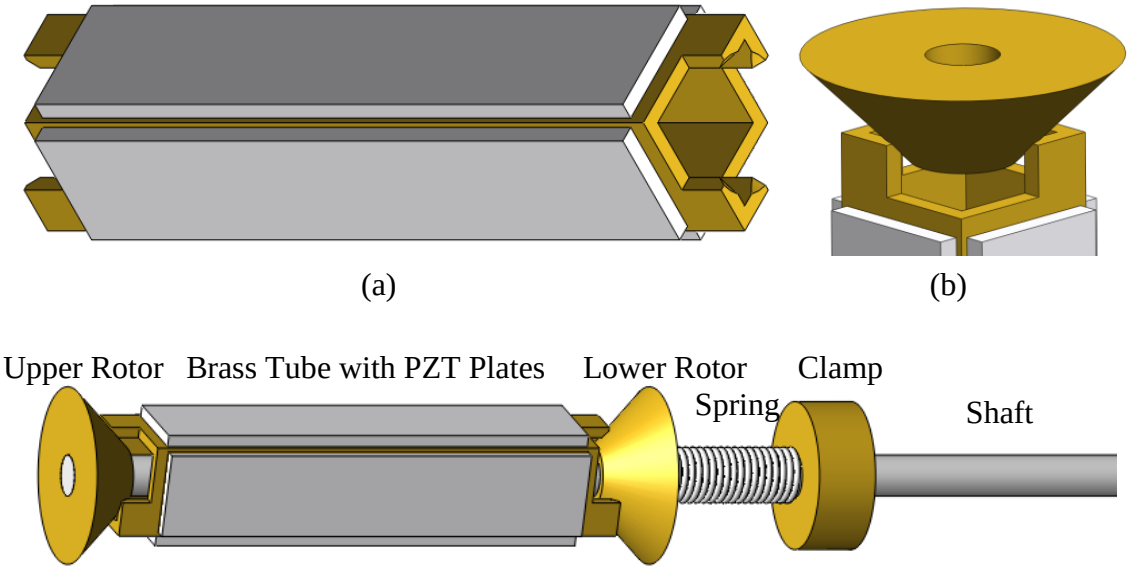

Figure 3.1 - Standing wave brass-PZT square tubular ultrasonic motor. (a) Stator. (b) Rotor. (c) The motor assembly.

The PZT plates are bonded with their polarization directions aligned as shown in Figure 3.2. When a sinusoidal voltage is applied to the PZT plates P_A and P_C as shown in Figure 3.2 (a), one PZT plate expands and the other contracts. Subsequently the brass-PZT square tube vibrates following a bending mode about the X-axis as shown in Figure 3.2 (a). When the voltage is applied to the PZT plates P_B and P_D, the tube vibrates about the Y-axis as shown in Figure 3.2 (b).

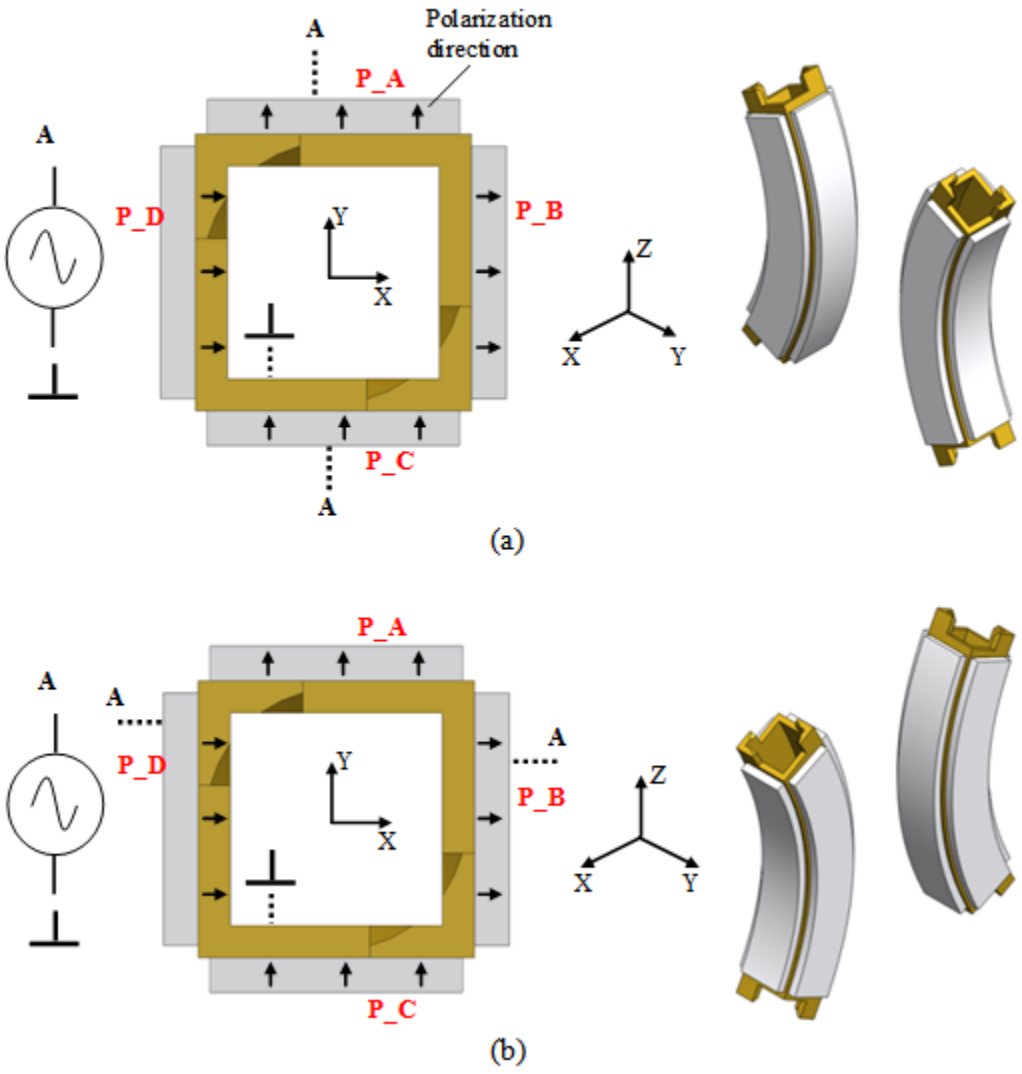

Figure 3.2 - Brass-PZT square tube vibration following a single bending mode. (a) Vibration along X-axis. (b) Vibration along Y-axis.

The trajectories of the tube endpoints formed when the tube vibrates in bending mode can explain the rotation of the motor. When the square tube vibrates along the X-axis, points at the two opposite corners of the tube ends, such as Points 1, 2, 5 and 6 of Figure 3.3, move following reciprocal diagonal trajectories in Z`Y` planes which represent plane parallel to the ZY plane as

shown in Figure 3.3(a). These diagonal trajectories can be decomposed into components in the radial and circumferential planes. For example, the trajectory of Point 2 is decomposed into a diagonal trajectory in the radial plane and circumferential plane. The trajectories in the radial planes do not generate any motion of the rotor because the motion of the rotor along the radial direction is constrained by the tube teeth. The diagonal trajectories in the circumferential planes push the rotor to continuously rotate in counter-clockwise direction.

When the square tube vibrates along the Y-axis as shown in Figure 3.3 (b), the diagonal trajectories of Points 1, 2, 5 and 6 are in planes parallel to the ZX plane which are labeled as Z`X` planes. The trajectories can also be decomposed into diagonal trajectories in radial and circumferential planes. The diagonal trajectories in circumferential planes push the rotor to rotate clockwise. Points at the other two opposite corners such as Points 3, 4, 7 and 8 also generate diagonal trajectories to rotate the rotor, but in the direction opposite to that driven by the Points 1, 2, 5 and 6. Therefore only two opposite corners of the tube end are designed to contact the rotor in order to drive it for continuous rotation in only one direction. Two teeth are formed on the opposite corners of the rectangular brass tube as shown in Figure 3.3. The teeth on both ends of the tube are aligned to push the upper and lower rotors to rotate in the same direction.

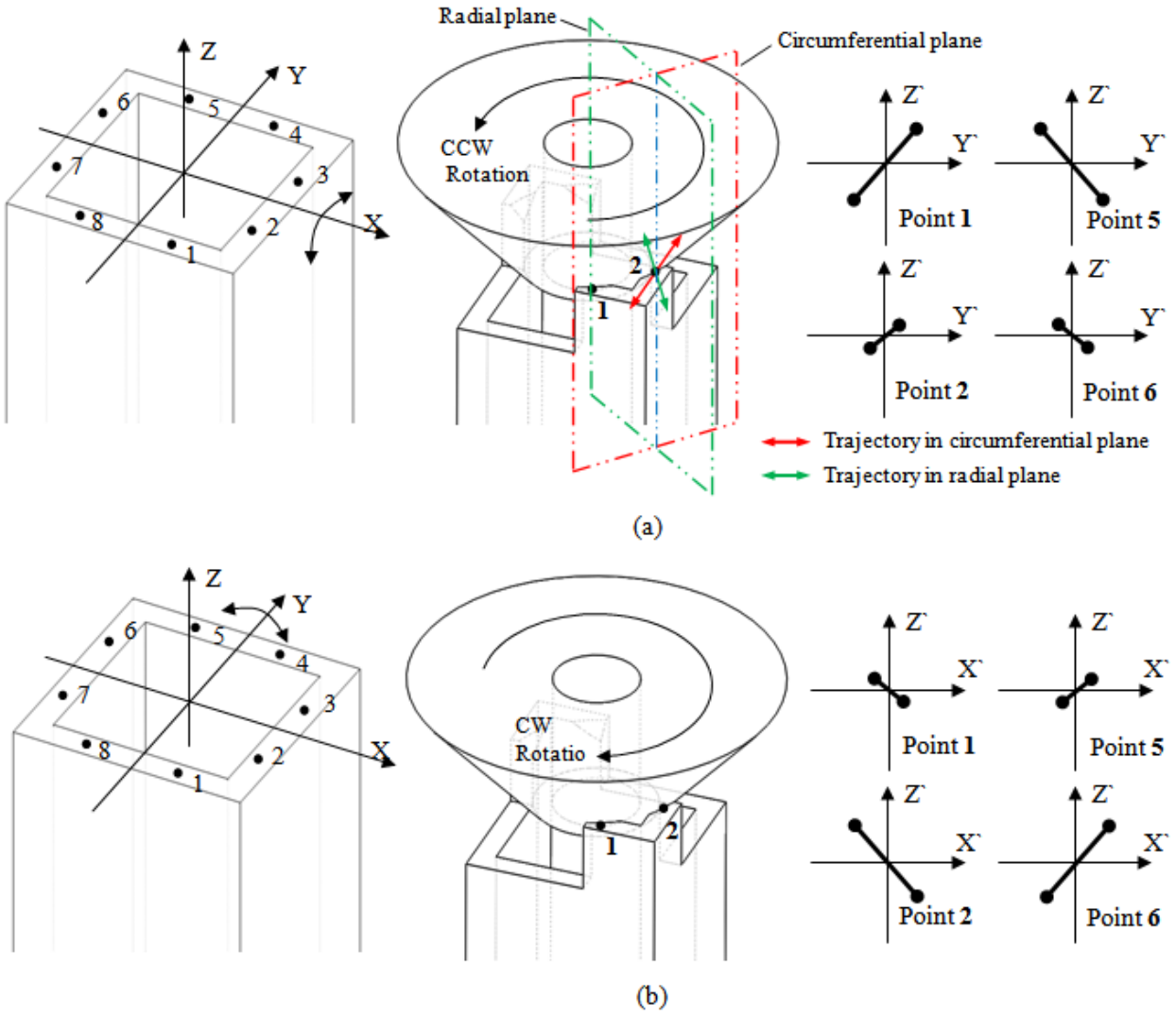

Figure 3.3 - Reciprocal diagonal trajectories are generated to drive the rotors. Trajectories generated when the tube vibrates about X-axis. (b) Trajectories generated when the tube vibrates about Y-axis.

3.3 Brass Tube Motor Prototype

3.3.1 Prototype description

The prototype is shown in Figure 3.4. The dimension of the square brass tube is 3.175 mm x 3.175 mm x 16 mm with wall thickness of 0.37 mm. The teeth are 1 mm high and 1.2 mm wide on each side from the corners. The dimensions of PZT plates are 2.9 mm x 15 mm with thickness of 0.4 mm. Epoxy is used to bond the PZT plates on each side of the brass tube. Two conical brass ring rotors are fabricated to sit on the teeth. The upper rotor is bonded to the shaft and the lower rotor is pressed against the teeth using a spring with a compression force of 0.55 N. The PZT plates are bonded with their polarization directions aligned as shown in Figure 3.2. Properties of the brass and the PZT plates are listed in Table 3.1.

Table 3.1 - Properties of the brass and PZT used in the motor.

	Young's modulus (GPa)	Young's modulus along 33(GPa)	Young's modulus along 11 (GPa)	Density (Kg/m^3)	Poisson's ratio	Piezoelectric Constant d_{31} (pC/N)	Piezoelectric constant d_{31} (pC/N)	Relative dielectric constant	Quality factor	Damping ratio
Brass	115	-	-	8900	0.3	-	-	-	-	0.001
PZT	-	63	76	7700	0.3	-109	300	1500	1500	-

(a)

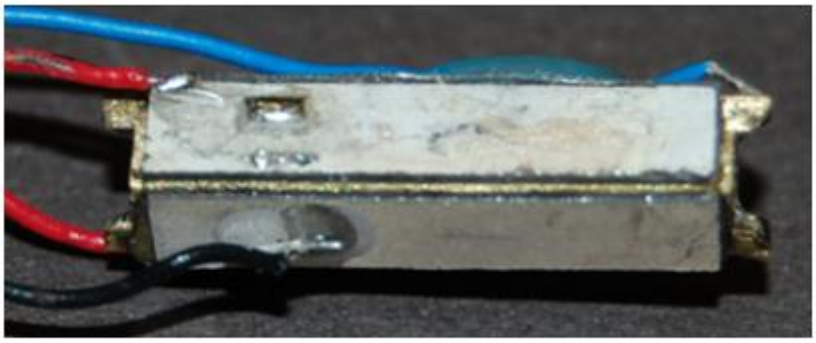

(b)

Figure 3.4 - Prototype of the standing wave brass-PZT square tubular ultrasonic motor. (a) Assembly of the motor. (b) Brass-PZT square tube.

3.3.2 Simulation results

Simulation software package ANSYS is used to simulate the brass-PZT tube. A sinusoidal voltage of 50 V is applied to two opposite PZT plates A and C as shown in Figure 3.5. The simulation results show that the vibrations along the two principal axes are at frequencies of 46790 Hz and 47150 Hz respectively as shown in Figure 3.5 (a) and (b). The vibrations along the non-principal axes are along the PZT plates A and C, which are subjected to voltages with frequencies of 46873 Hz and 47360 Hz, as shown in Figure 3.5 (c) and (d). Vibrations about the

principal axes cannot be used to drive the motor but the vibrations about the non-principal axes are desired for driving the motor as explained in Figure 3.2 and Figure 3.3.

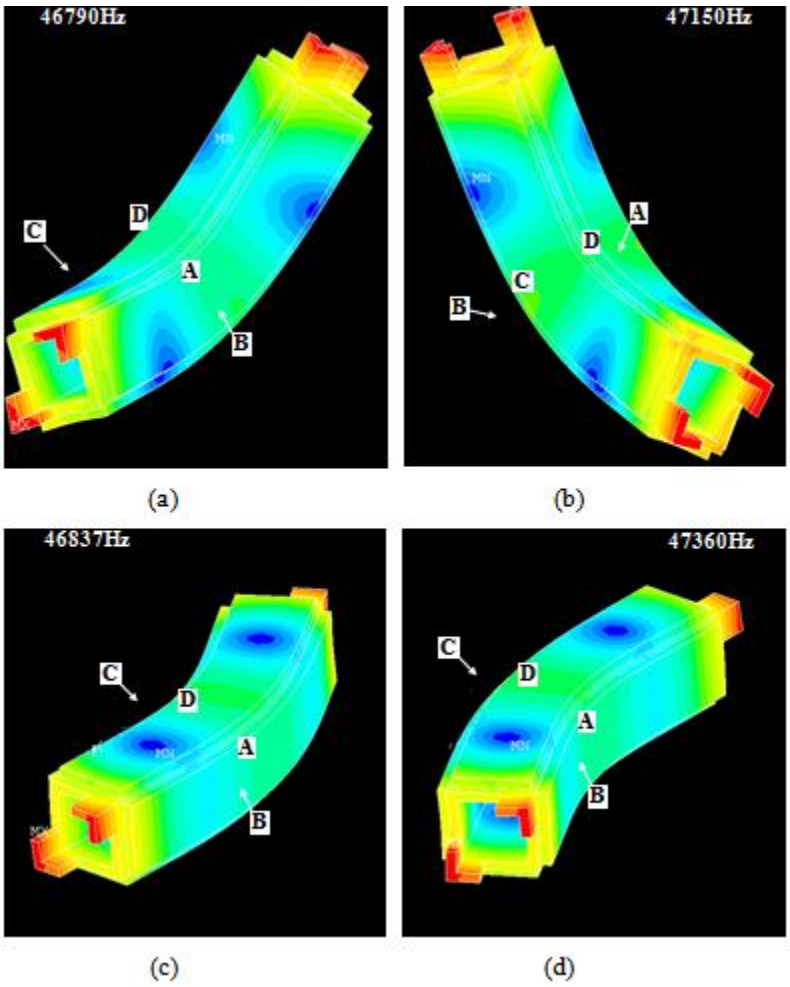

Figure 3.5 - Simulation results. (a) Vibration along principal axis with bending direction along edge between PZT plates A and D. (b) Vibration along principal axis with bending direction along edge between PZT plates C and D. (c) Vibration along non-principal axis with bending direction along PZT plates A and C. (d) Vibration along non-principal axis with bending direction along PZT plates A and C.

When applying the voltage with the frequency of the desired vibration which is about the non-principal axis as shown in Figure 3.5 (c) or (d), not only vibration in Figure 3.5 (c) or (d) would be excited, but the vibration in Figure 3.5 (a) or (b) could also be excited due to their frequencies being close to each other, but the vibration in Figure 3.5 (c) or (d) would be the dominant one.

3.4 Experimental testing

3.4.1 Frequency response

ZYGO optical 3-D profiler is used for frequency response analysis of the prototype. It measures the phase of vibration at a set range of frequencies by measuring the out of plane displacement of the points. Figure 3.6 shows the setup of the prototype in the ZYGO profiler. The prototype is fixed under the microscope by fixing the wires onto the stage and signal generator with amplifier is synchronized with ZYGO profiler for dynamic analysis using DMEMS module. All four sides of the prototype is measured one at a time by placing the measuring side to be perpendicular to the microscope. The prototype is driven with sinusoidal signal by the function generator at amplitude of ±12.5 V with zero offset. The reason for applying lower amplitude than actual driving amplitude is that the ZYGO profiler is able to measure the displacements in micro range accurately, enabling only a small magnitude of vibration to be sufficient for measurement.

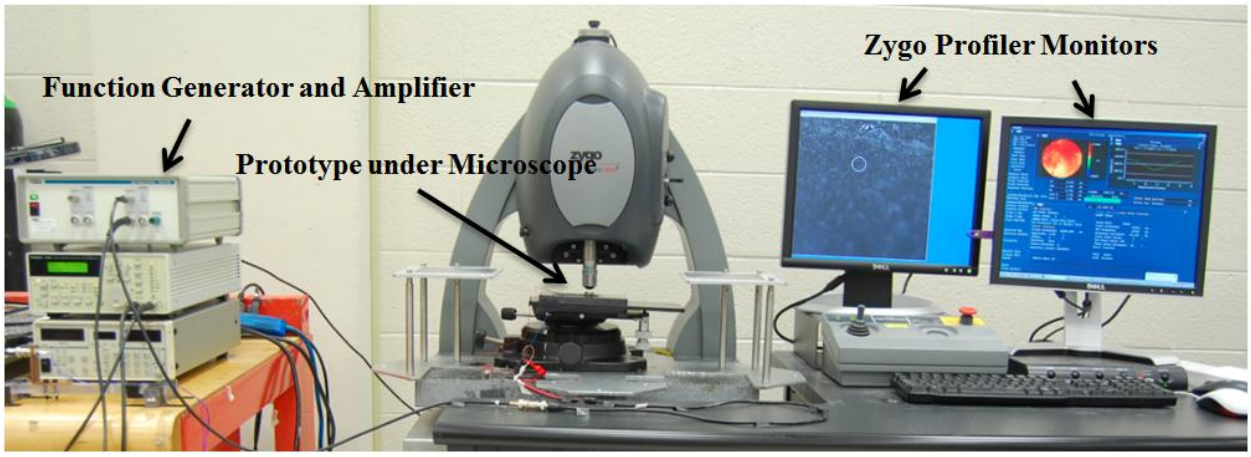

Figure 3.6 - ZYGO 3D Optical Profiler Setup.

The resonant frequencies of bending vibration along both X axis and Y axis are measured. The two PZT plates in X axis are connected with black wires and two plates in Y axis are connected with red wires. By measuring the out of plane displacement of a point on the PZT plate while scanning through a range of frequencies, the resonant frequencies can be found at the frequencies where the displacement is at a peak. The scanning frequency range is set to be between 45.50 kHz to 47.70 kHz with a phase interval of 30 °. The scanning result is shown in Table 3.2. A plot of displacement versus frequency is shown in Figure 3.7. The first resonant bending vibration frequency along X axis and Y axis are measured to be 46.20 kHz and 46.10 kHz, respectively.

Table 3.2 – Frequency sweep to measure out of displacements for both bending vibration along X axis and Y axis.

Bending along Y-Axis		Bending along X-Axis	
Frequency (KHz)	Displacements (nm)	Frequency (KHz)	Displacements (nm)
45.50	610.94	45.50	214.08
45.60	574.47	45.60	194.64
45.70	730.71	45.70	261.74
45.80	807.86	45.80	322.51
45.90	1041.71	45.90	399.84
46.00	1286.96	46.00	621.53
46.10	1915.28	46.10	1376.84
46.20	1875.22	46.20	2739.66
46.30	1802.22	46.30	1565.77
46.40	1789.96	46.40	947.54
46.50	1695.11	46.50	1330.76
46.60	1557.27	46.60	1345.50
46.70	1352.53	46.70	1126.96
46.80	1243.31	46.80	985.20
46.90	1167.55	46.90	889.50
47.00	935.05	47.00	770.72
47.10	1028.80	47.10	600.22
47.20	733.44	47.20	457.40
47.30	642.39	47.30	379.71
47.40	814.54	47.40	286.11
47.50	819.46	47.50	277.21
47.60	682.42	47.60	380.05
47.70	496.35	47.70	175.93

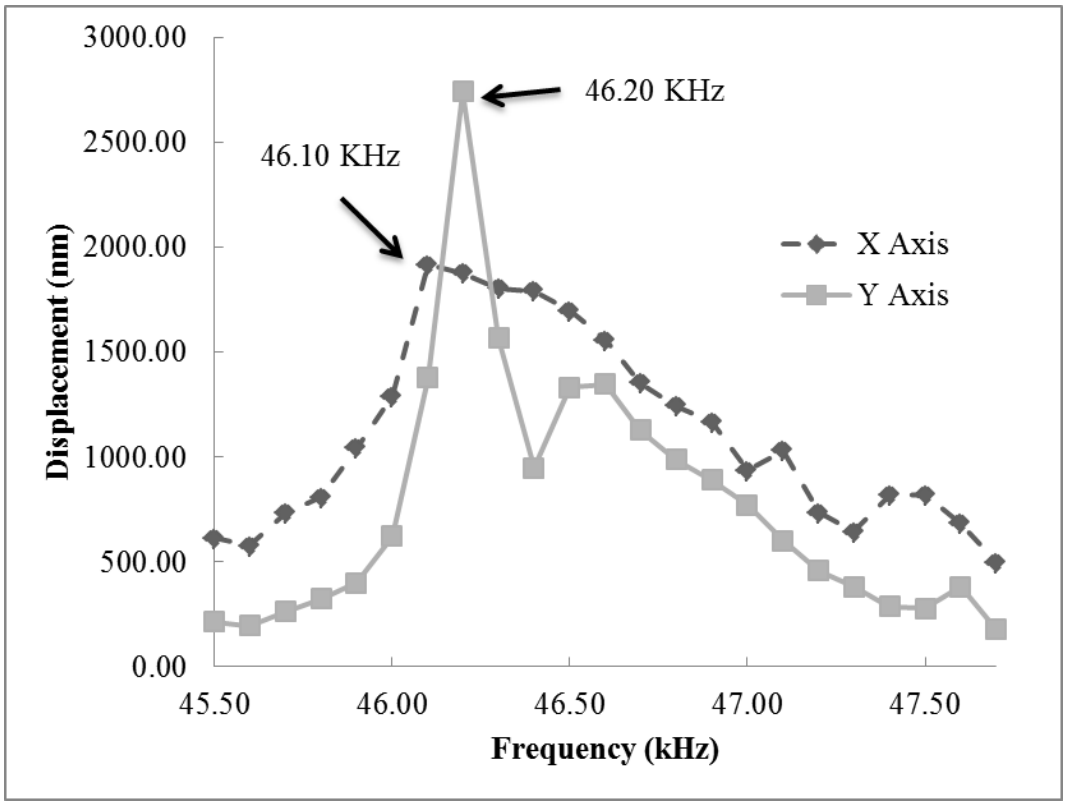

Figure 3.7 - ZYGO profiler measure of resonant frequency of first bending mode.

The slight discrepancy in the value of frequencies for each direction can be due to the slightly non-symmetrical geometry of the tube and the teeth. Since the tube and the teeth are so small, it is very difficult to machine them perfectly symmetrical. However, note that the frequencies of 46.10 kHz and 46.20 kHz are at when the motor performs at best which means the motor can still rotate at a frequency in between two values such as 46.15 kHz. This enables bi-directional rotation of the motor as the signal pairing can be switched from one to the other while keeping the applied frequency the same.

3.3.2 Motor performance

The performance of the prototype is tested using the setup shown in Figure 3.8. The motor shaft is fixed on a plate through two ball bearings. The motor tube is held by fixing the wires connected to the PZT plates. A string with weights is attached to the shaft to measure the torque. A laser, a laser sensor (Position Sensing Detector) and an oscilloscope are used to measure the rotation speed of the motor. A laser beam is sent out from the laser source and reaches to the laser sensor. The laser beam is blocked by a flag attached to the shaft once per revolution. An oscilloscope records the output of the laser sensor. The motor speed can be calculated from the laser sensor output signal recorded on the oscilloscope. The motor is driven at the resonant frequencies found from the previous section, i.e., counter-clockwise direction (brass-PZT tube vibration about X-axis) at 46.10 kHz while clockwise direction ((brass-PZT tube vibration about Y-axis) at 46.20 kHz. The driving voltage magnitude is 50 V. The motor can achieve a no-load speed of 1005.8 RPM in clockwise direction and 1042.2 RPM in counter-clockwise direction. The stall torque of the motor in both directions is 371.134 μNm. The loads applied to the motor, rotation frequencies detected by the laser sensor, calculated speed and torque are listed in Table 3.3. The output powers of the motor in both directions are calculated and listed in Table 3.4. The maximum power is 9.436 mW in clockwise direction and 15.393 mW in counter-clockwise direction. The plots of the speed versus torque and the speed versus power are shown in Figure 3.9.

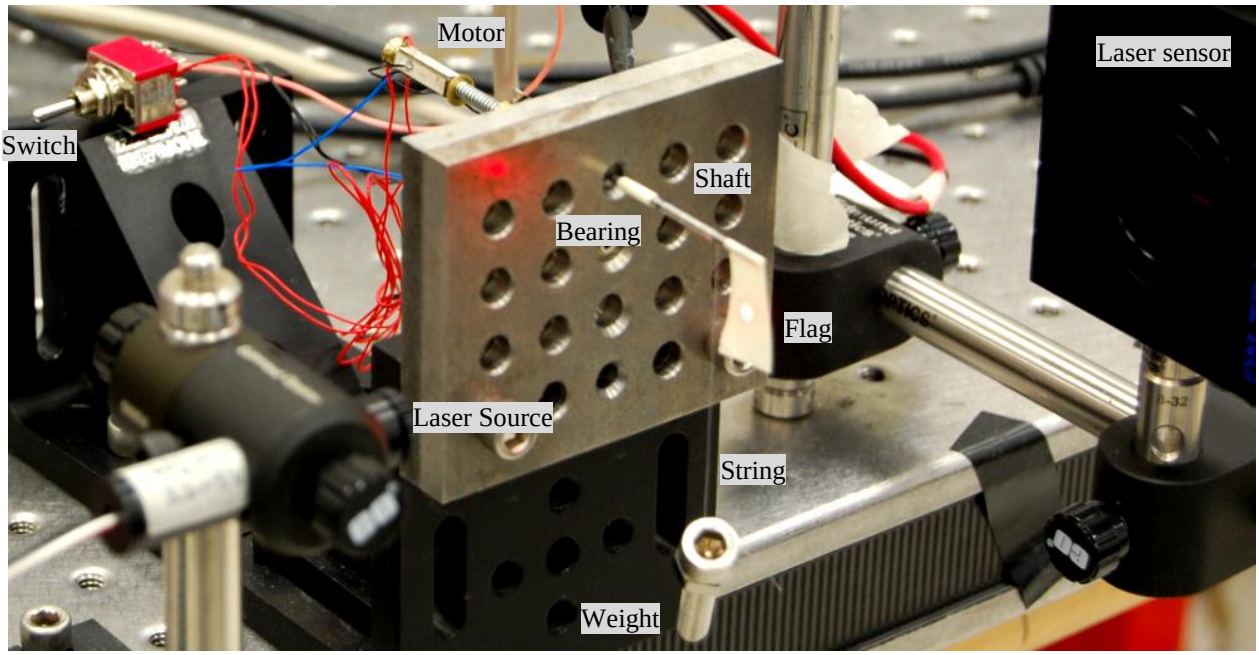

Figure 3.8 - Setup for the motor performance test.

The standing wave brass-PZT square tubular ultrasonic motor presented in this chapter has achieved a much better performance than the standing wave PZT tube ultrasonic motor previously reported in Chapter 3, which includes: higher no-load speed (1042.2 RPM versus 468 RPM), higher stall torque (370 μNm versus 296 μNm), higher output power (16 mW versus 5 mW), and smaller size (3.975 mm x 3.975 mm x 16 mm versus 6.6 mm in diameter x 25.4 mm). The improved performance has been obtained due to the brass-PZT composite tube structure instead of the PZT tube is utilized.

Table 3.3 - Speed and torque calculation table for both clockwise and counter-clockwise direction.

Clockwise Direction								
Load (g)	Rotation Frequency (Hz)			Speed (RPM)			Average Speed (RPM)	Torque (μNm)
0.000	16.670	17.090	16.530	1000.200	1025.400	991.800	1005.800	0.000
10.078	9.709	10.310	10.530	582.540	618.600	631.800	610.980	69.206
20.740	9.346	8.772	8.130	560.760	526.320	487.800	524.960	142.422
30.154	7.463	7.092	6.803	447.780	425.520	408.180	427.160	207.068
41.643	6.369	4.386	5.000	382.140	263.160	300.000	315.100	285.962
54.046	0.000	0.000	0.000	0.000	0.000	0.000	0.000	371.134

Counter-Clockwise Direction								
Load (g)	Rotation Frequency (Hz)			Speed (RPM)			Average Speed (RPM)	Torque (μNm)
0.000	16.390	17.540	18.180	983.400	1052.400	1090.800	1042.200	0.000
10.078	14.930	13.510	13.160	895.800	810.600	789.600	832.000	69.206
20.740	11.760	11.490	11.490	705.600	689.400	689.400	694.800	142.422
30.154	10.310	9.709	9.434	618.600	582.540	566.040	589.060	207.068
41.643	9.709	8.850	7.143	582.540	531.000	428.580	514.040	285.962
54.046	0.000	0.000	0.000	0.000	0.000	0.000	0.000	371.134

Table 3.4 - Speed and output power table for both clockwise and counter-clockwise direction.

Counter-Clockwise Direction		Clockwise Direction	
Speed (RPM)	Power (mW)	Speed (RPM)	Power (mW)
1042.200	0.000	1005.800	0.000
832.000	6.030	610.980	4.428
694.800	10.362	524.960	7.829
589.060	12.773	427.160	9.263
514.040	15.393	315.100	9.436
0.000	0.000	0.000	0.000

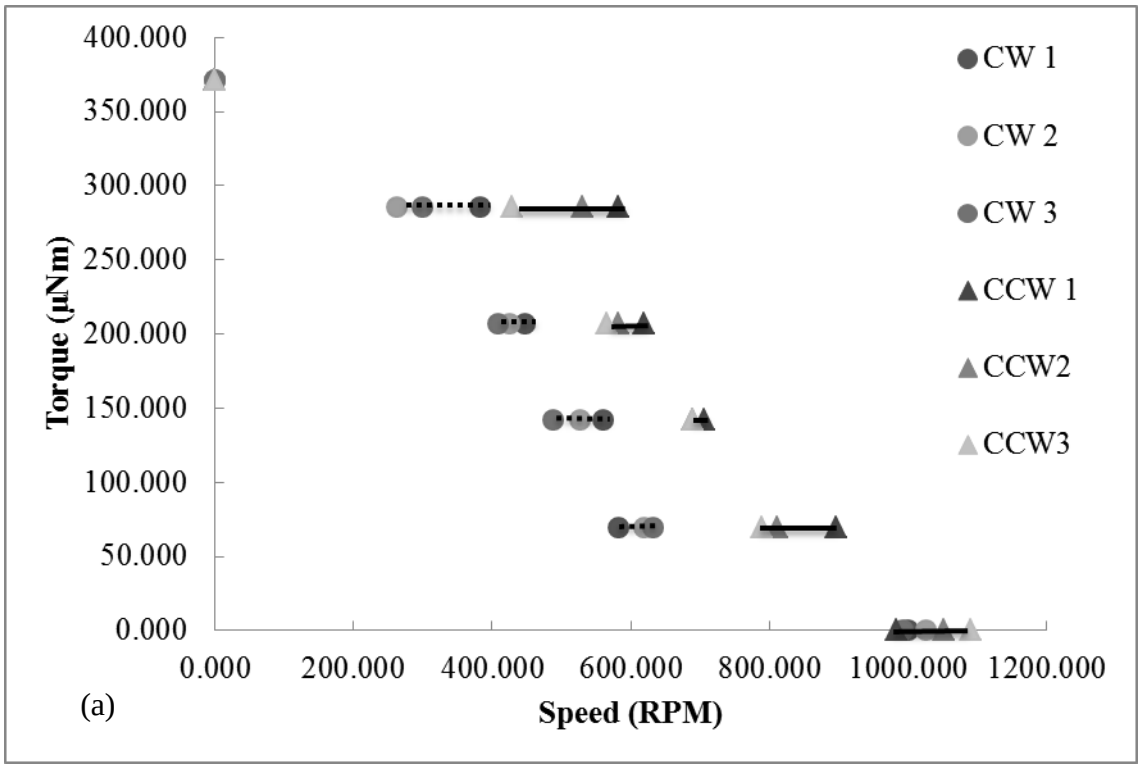

(a)

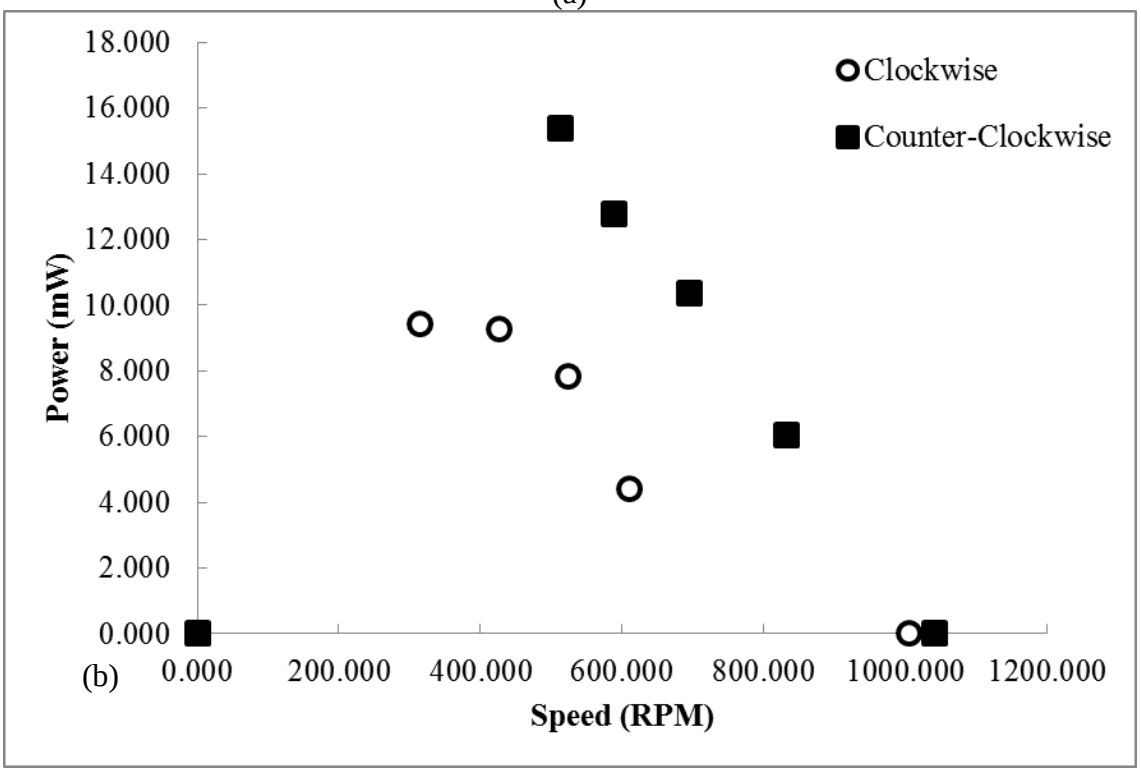

(b)

Figure 3.9 - Performance of the motor. (a) Torque versus speed. (b) Power versus speed.

Chapter 4. Waveform Measurement

4.1 Chapter introduction

This chapter is dedicated for verifying that the novel piezoelectric ultrasonic motor prototypes reported in this thesis are in fact standing wave type motors. Tube type ultrasonic motors can be identified as standing wave type or travelling wave type. A PZT cylindrical tube can be excited with either in a standing waveform or a travelling waveform. In this chapter, a simple PZT tube is selected for an example to be excited with both a standing wave and a travelling wave vibration mode. A novel method of detecting whether it is excited with a standing wave or travelling wave is described. Then the prototype motors are put into test to verify if they are vibrating in a standing waveform. The testing setup and measurements results are reported. Example designs and basic operating principles of both travelling wave type motors and standing wave type motors are discussed in Chapter 1.

4.2 PZT cylindrical tube vibration test

4.2.1 Sample tube and testing apparatus

A PZT tube is used to demonstrate the measurements of standing wave and traveling wave using the dynamic 3D profiler (ZYGO Newview 6300 DMEMS). The electrode on the outside wall of the PZT tube is divided into four sections A, B, C and D as shown in Figure 4.1. Standing wave is excited when one driving signal is applied while travelling wave is excited when two driving signals with $90°$ phase difference are applied. The out-of-plane displacements

at 12 locations marked on the outside wall of the PZT tube are measured with the phase relative to the driving singal.

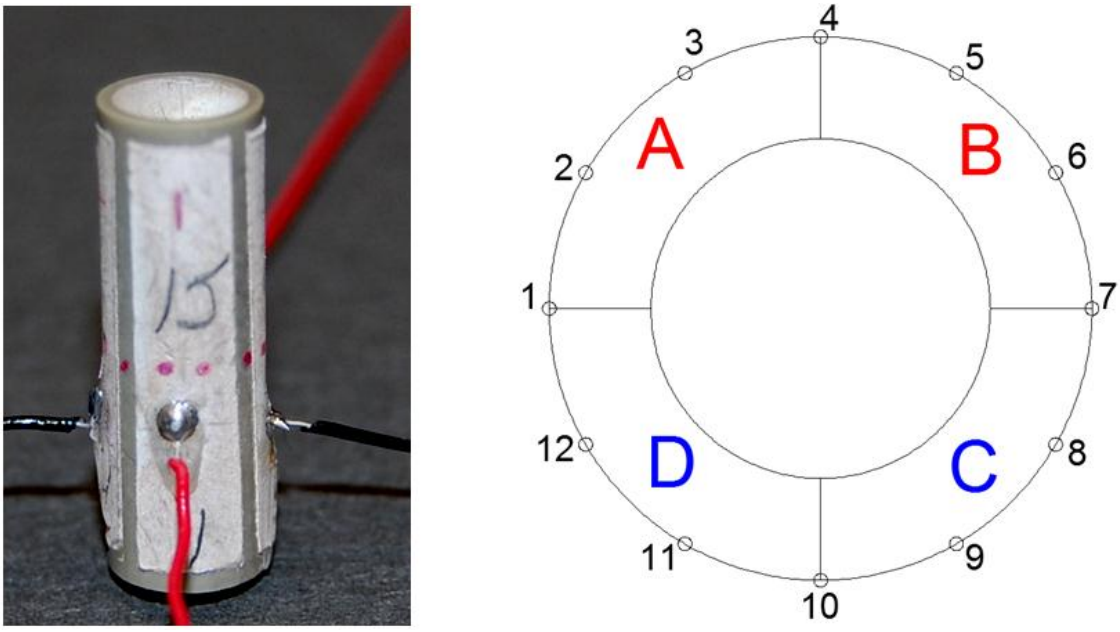

Figure 4.1 - PZT tube is used for measuring the standing/traveling waves. Red dots representing measuring locations on the outside wall of the PZT tube.

The testing apparatus is setup as shown in Figure 4.2 and Figure 4.3. The PZT tube is placed under the microscope of the optical profiler and the microscope scans the surface of the marked points of the tube. The tube is not firmly clamped on the stage since it is to be freely vibrating with the electrodes connected to the outer surface. The tube is suspended on the stage with four wires clamped on the stage with weights. Since the weight of the PZT tube is light enough and the vibration amplitude is in microns range, clamping the wires are enough for the testing purpose.

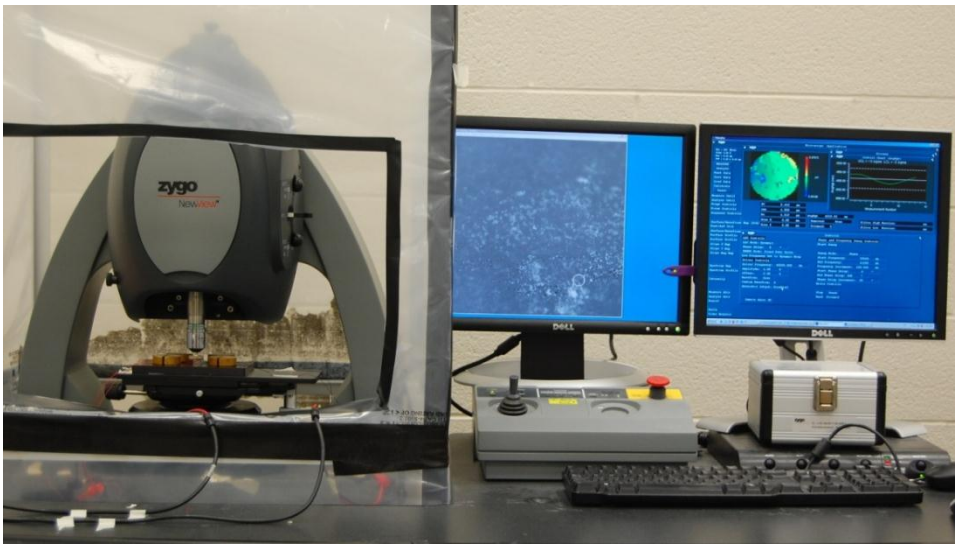

Figure 4.2 - Dynamic 3D optical profiler for measuring the standing/traveling waves.

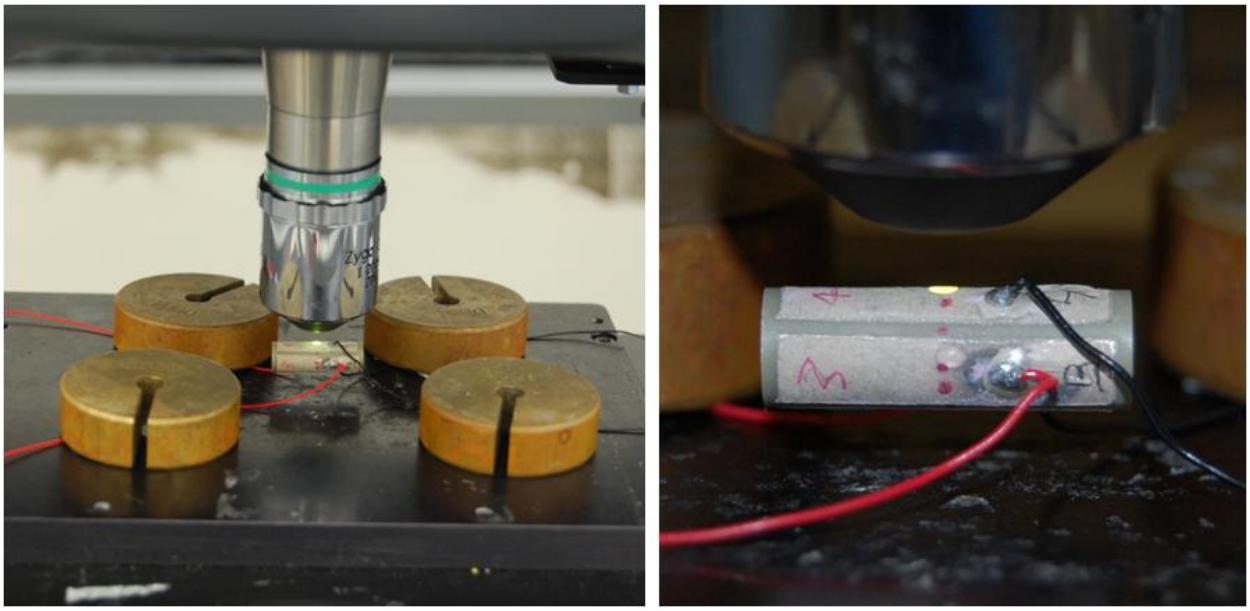

Figure 4.3 - The PZT tube is fixed with approximately free boundary condition through the fours wires soldered on the outside wall of the PZT tube.

4.2.2 Standing wave test

The PZT tube is driven with a single source of electrical signal to the paired electrodes of the outer surface. A sinusoidal wave of $25\sin(40200\cdot 2\pi\cdot t)$ V is applied to the electrode A and B simultaneously while the electrodes C and D are grounded. The out-of-displacements of the selected 12 points are shown in Figure 4.4. The displacements are detected for every $30\,°$ of phase for one period of sinusoidal wave and plotted. It is clearly shown that the plot of displacements are symmetrically opposite with respect to the points 1 and 7. The displacements are maximum at points 4 and 10 while minimum at points 1 and 7. This shows that the tube is vibrating in a standing waveform.

4.2.3 Travelling wave test

The PZT tube is driven with two sources of electrical signal with a phase difference of $90\,°$ to two adjecent electrodes of the outer surface. A sinusoidal wave of $25\sin(40200\cdot 2\pi\cdot t)$ V is applied to the electrode A and $25\sin(40200\cdot 2\pi\cdot t+\frac{\pi}{2})$ V is applied to the electrode B while the electrodes C and D are grounded. Same as the standing wave test, the out-of-plane displacements of the selected 12 points are recorded for every $30\,°$ of phase for one period of sinusoidal wave and plotted, as shown in Figure 4.5. Symmetry of waveform discovered in the previous figure is not found but rather a propagating sinusoidal waveform is detected. The displacements are constant throughout all 12 points without a clear maximum or minimum which was observed with standing wave test. Also, it is clear that the waveforms on the opposite sides are $180\,°$ reversed. Therefore, it can be concluded that the tube is vibrating in a traveling waveform.

Driving: **AB** - $25\sin(40200 \cdot 2\pi \cdot t)$ Volt **CD** – GND

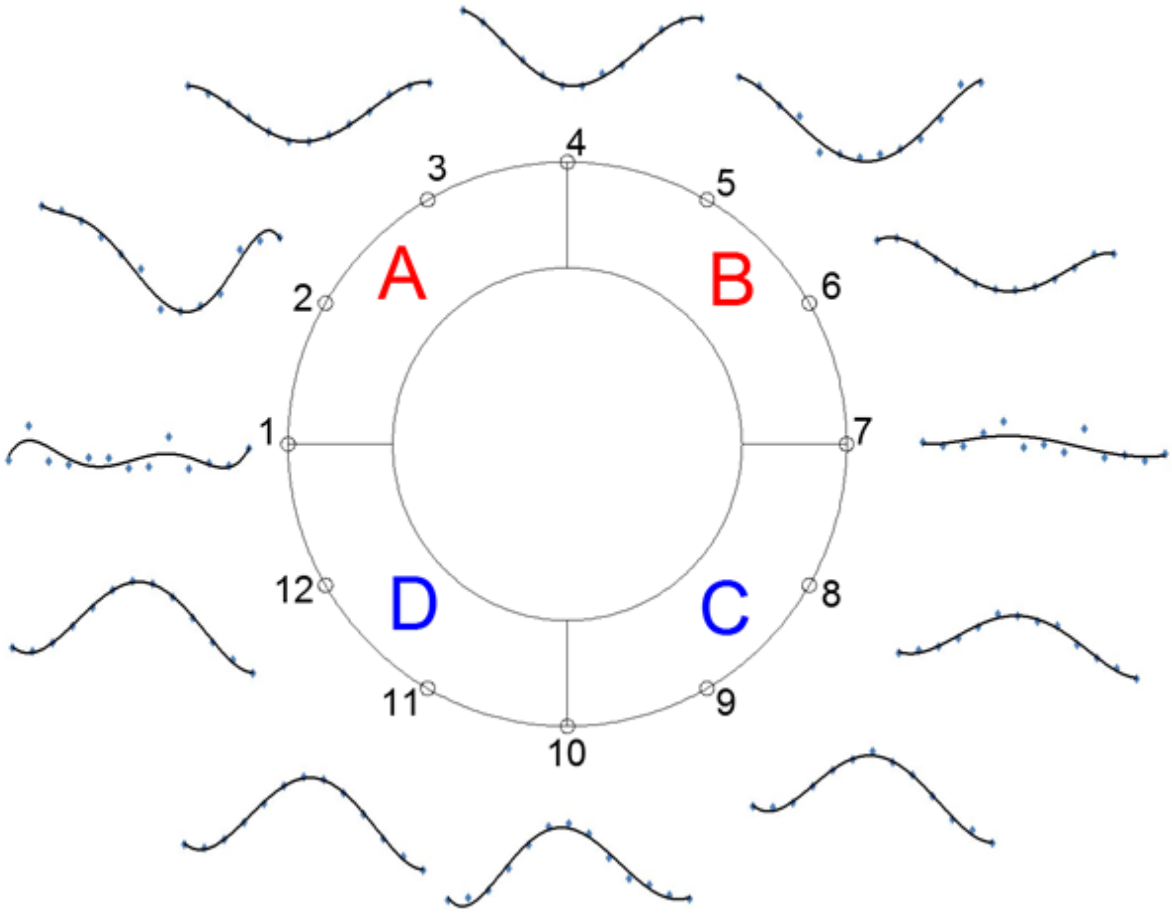

Figure 4.4 - Out-of-plane displacements measurements on 12 selected points for standing wave.

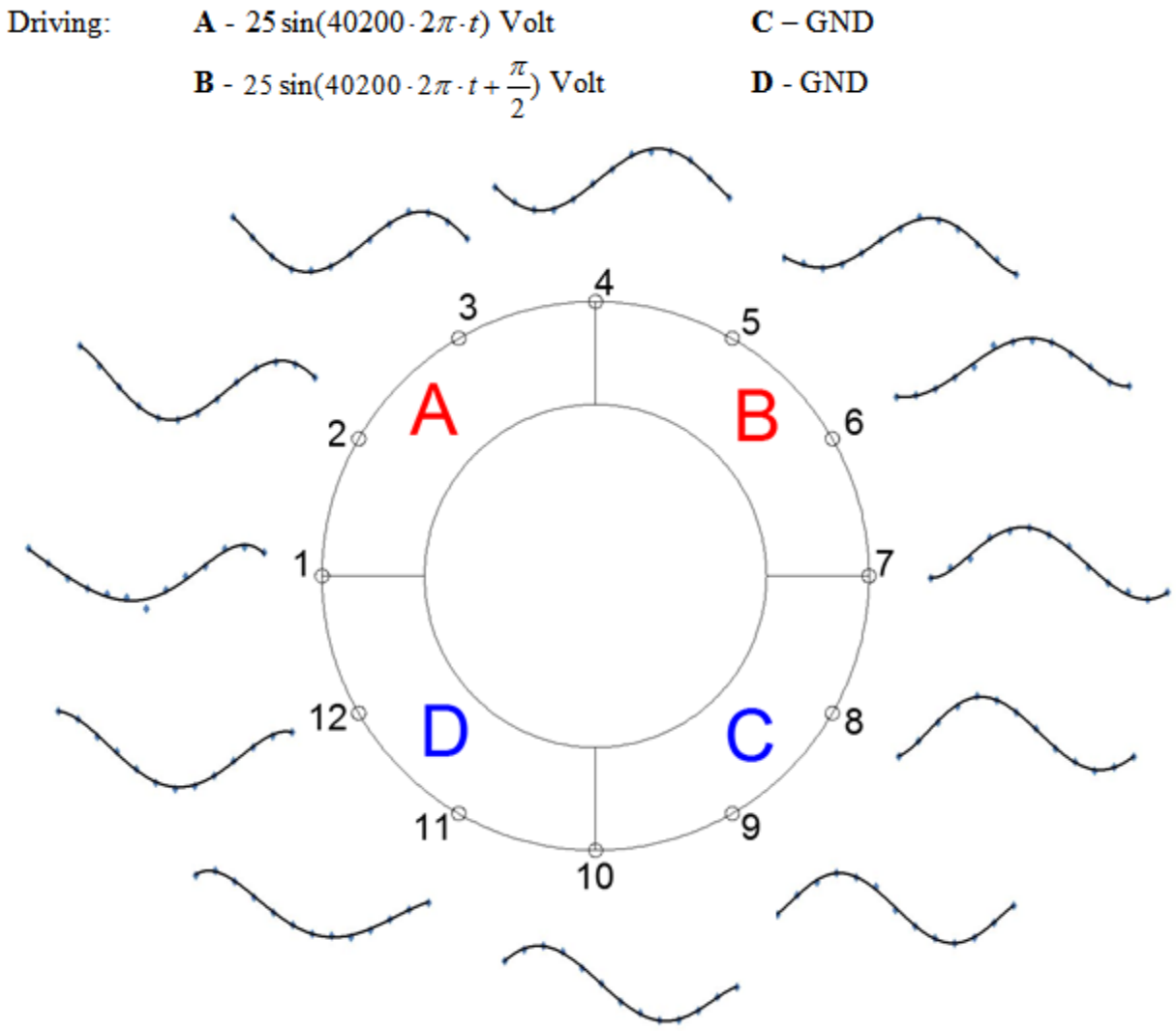

Figure 4.5 - Out-of-plane displacements measurements on 12 selected points for travelling wave.

4.3 Waveform measurement of PZT teeth motor

A dynamic 3D optical profiler, ZYGO NewView 6300 with DMEMS is used for verifying the vibration waveform of the PZT teeth motor. Along the outer surface of the PZT tube, the phases of out-of-plane displacements of 17 selected points, as shown in Figure 4.6, are

measured while exciting the motor at its working frequency of 27.6 KHz and at a driving voltage of ±25 V. Figure 4.7 (a), (b) show the setup of the piezoelectric ultrasonic motor on the optical profiler for the measurements. For accurate measurements, the points are selected as close as to the middle section of the tube where the displacement is at maximum in length direction of the tube. The shaft is clamped while the suspended motor vibrates at working frequency. Since the applied voltage is low, the driving force is not strong enough to rotate the rotor. The phase versus out-of-plane displacement is measured for one period of driving signal with an interval of 30 °.

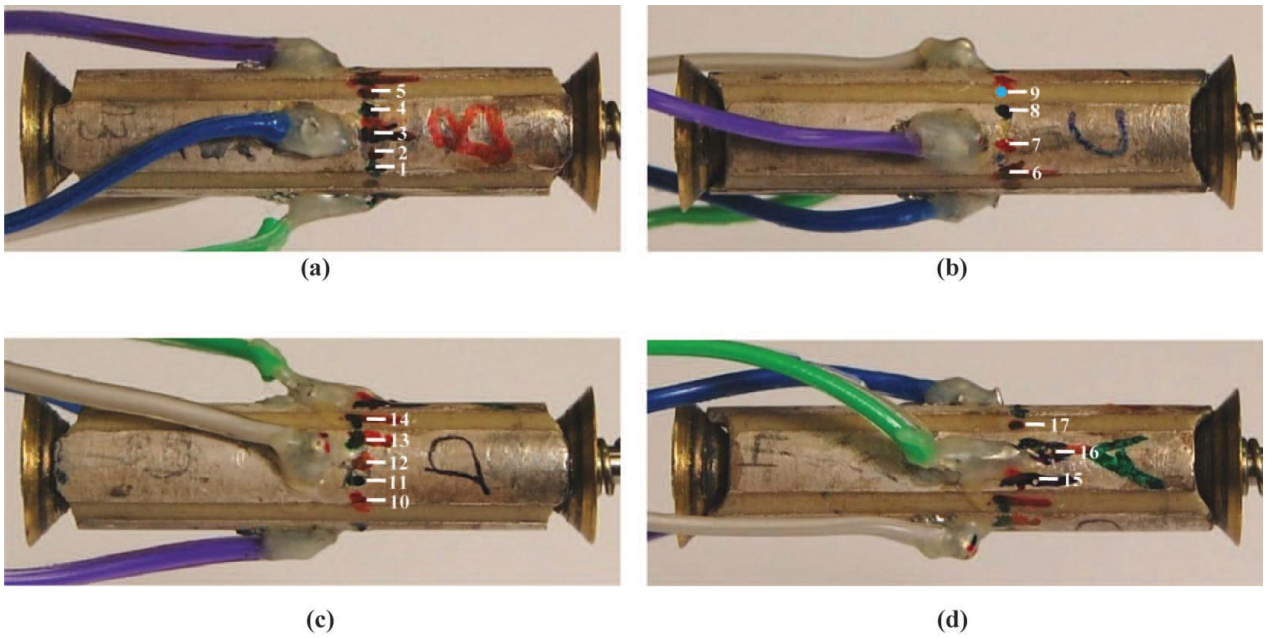

Figure 4.6 - Points selected for out-of-plane displacement measurements [41].

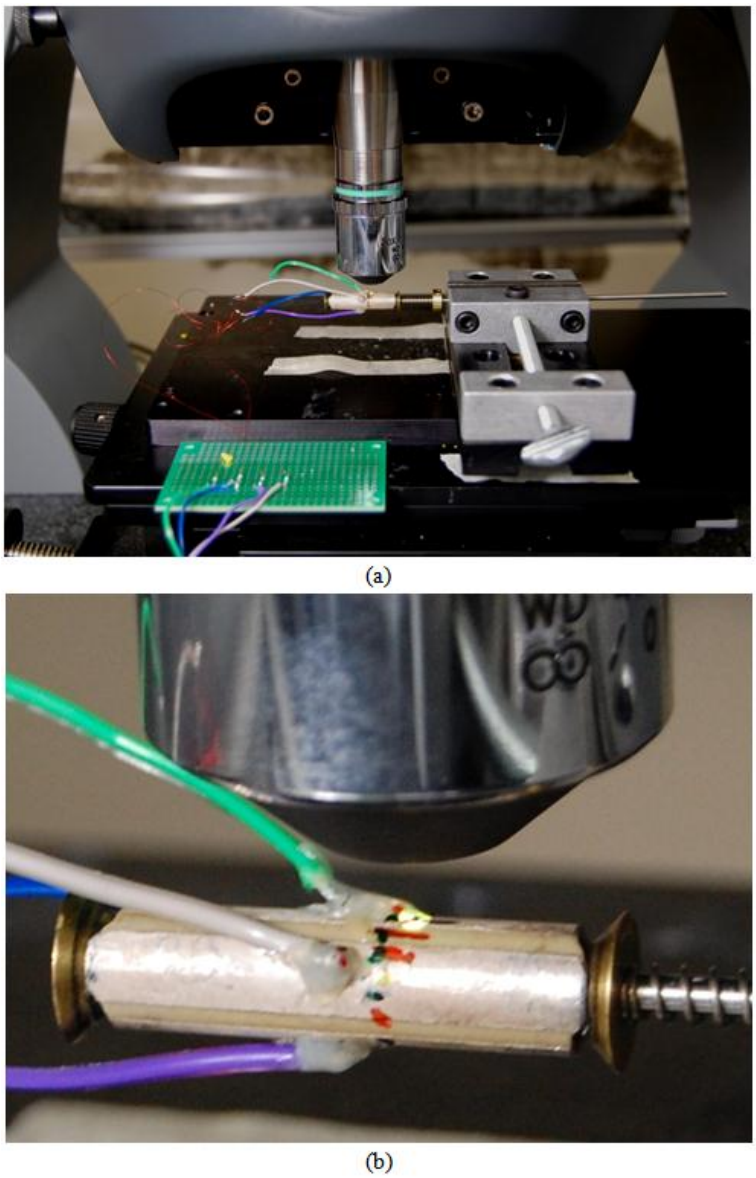

Figure 4.7 - Optical profiler measurement of vibration mode. (a) Setup for the measurements. (b) Selected points are marked [41].

The measured results are shown in Figure 4.8 for when electrodes AB and CD are paired and in Figure 4.9 for when electrodes AD and BC are paired. The plot on each selected points display the displacements in the same scale. It is evident that the displacement is out-of-phase

by 180 ° on each half of the tube as there is a sudden reverse of phase, between points 5 and 14 for Figure 4.8 and points 1 and 10 for Figure 4.9. This represents the bending axis of Y-axis and X-axis. The minimum displacements are detected at along the same axis which verifies that the bending mode is along the non-principle axes. This confirms the operating principle of the motor discussed in Chapter 3.

The standing waveform is also verified from the figures when electrodes are paired AB and CD, or AD and BC. The sudden reverse of phase by 180 ° along the bending axes can only be shown in a standing waveform. A gradual change in phase would be detected if a traveling wave is generated.

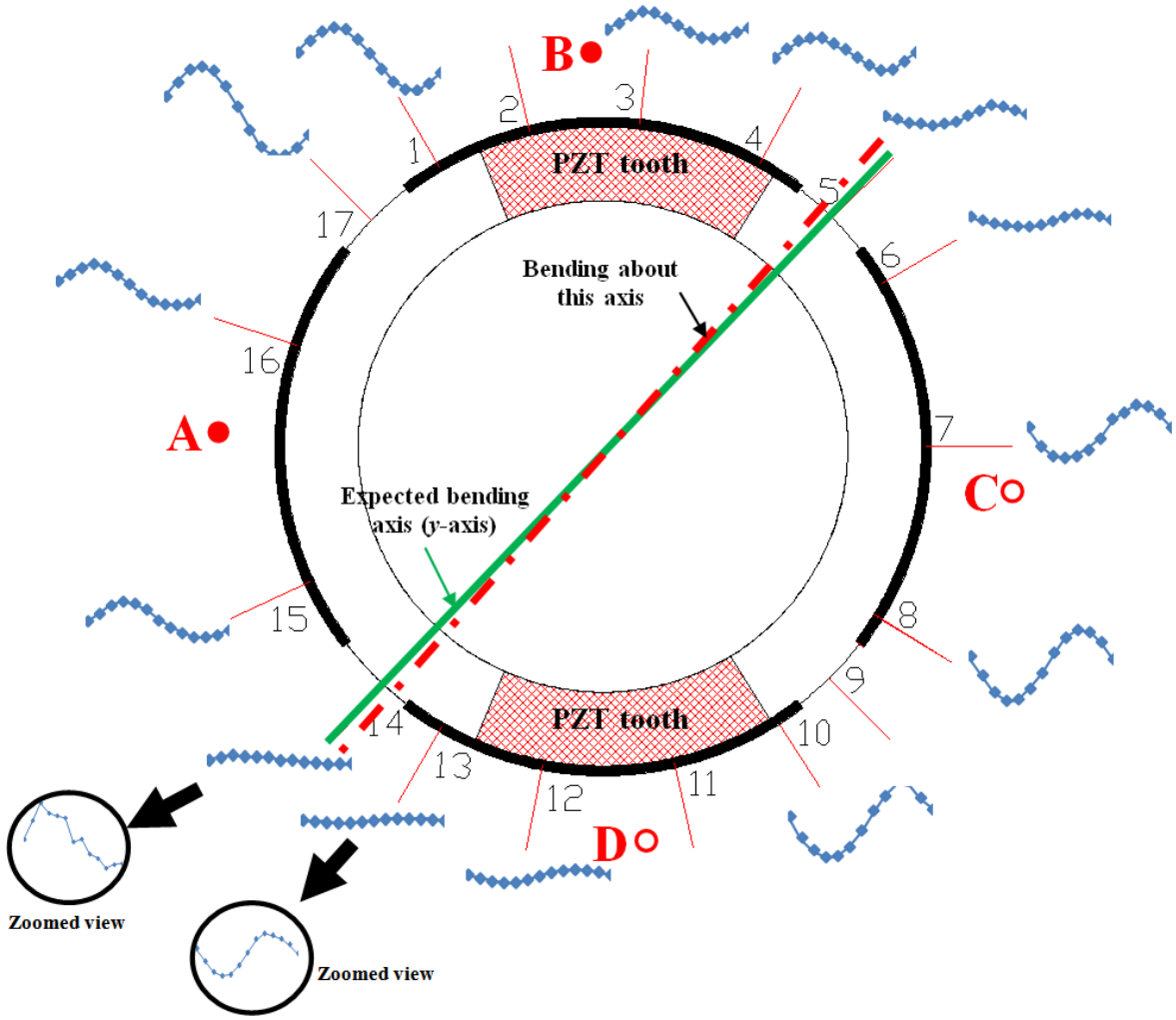

Figure 4.8 - PZT teeth motor vibration waveform test with electrodes paired AB & CD [41].

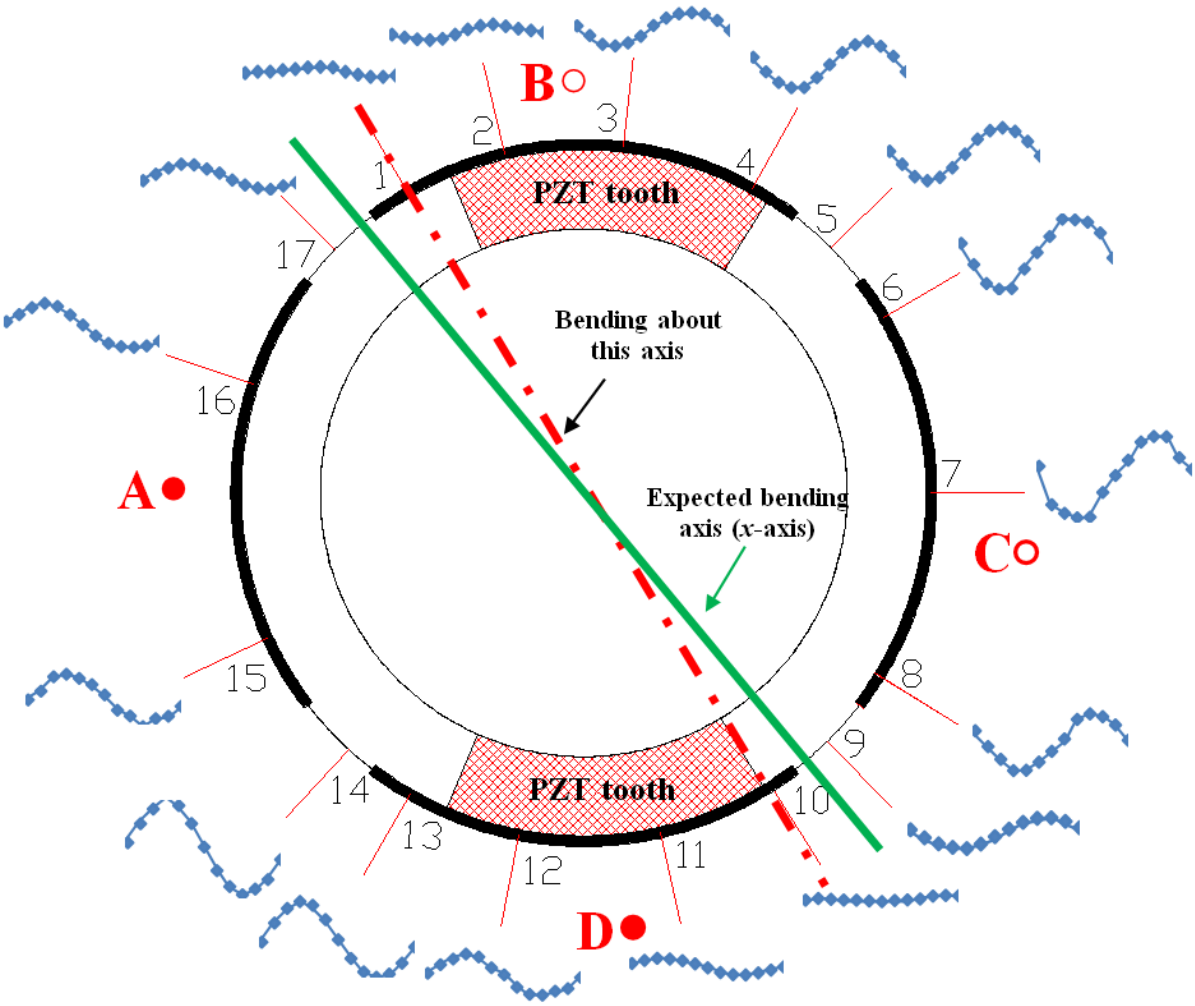

Figure 4.9 - PZT teeth motor vibration waveform test with electrodes paired AD & BC [41].

4.4 Waveform measurement of metal teeth motor

Same test has been done on the metal teeth motor to verify the waveform of the vibration. The measured results are shown in Figure 4.10 for when electrodes AB and CD are paired and in Figure 4.11 for when electrodes AD and BC are paired. The plot on each selected points display the displacements in the same scale. Same as for PZT teeth motor, it is evident that the displacement is out-of-phase by 180 ° on each half of the tube as there is a sudden reverse of

phase, between points 7 and 16 for Figure 4.10 and points 6 and 14 for Figure 4.11. This represents the bending axis of Y-axis and X-axis. The minimum displacements are detected at along the same axis which verifies that the bending mode is along the non-principle axes. This confirms the operating principle of the motor discussed in Chapter 3.

The standing waveform is also verified from the figures when electrodes are paired AB and CD, or AD and BC. The sudden reverse of phase by 180 ° along the bending axes can only be shown in a standing waveform. A gradual change in phase would be detected if a traveling wave is generated.

A shift in the bending axes from expected locations is discovered. There are multiple reasons why this has occurred. First cause is the added mass and moment of inertia of metal teeth which increases the tendency to vibrate along the principle axes. Second is the misalignment of the metal teeth during assembly which can contribute to the shifting of the bending axes. Even after considering all the causes, the motor still vibrates in standing waveform at a slightly shifter bending axes which has a minor effect on the performance of the motor.

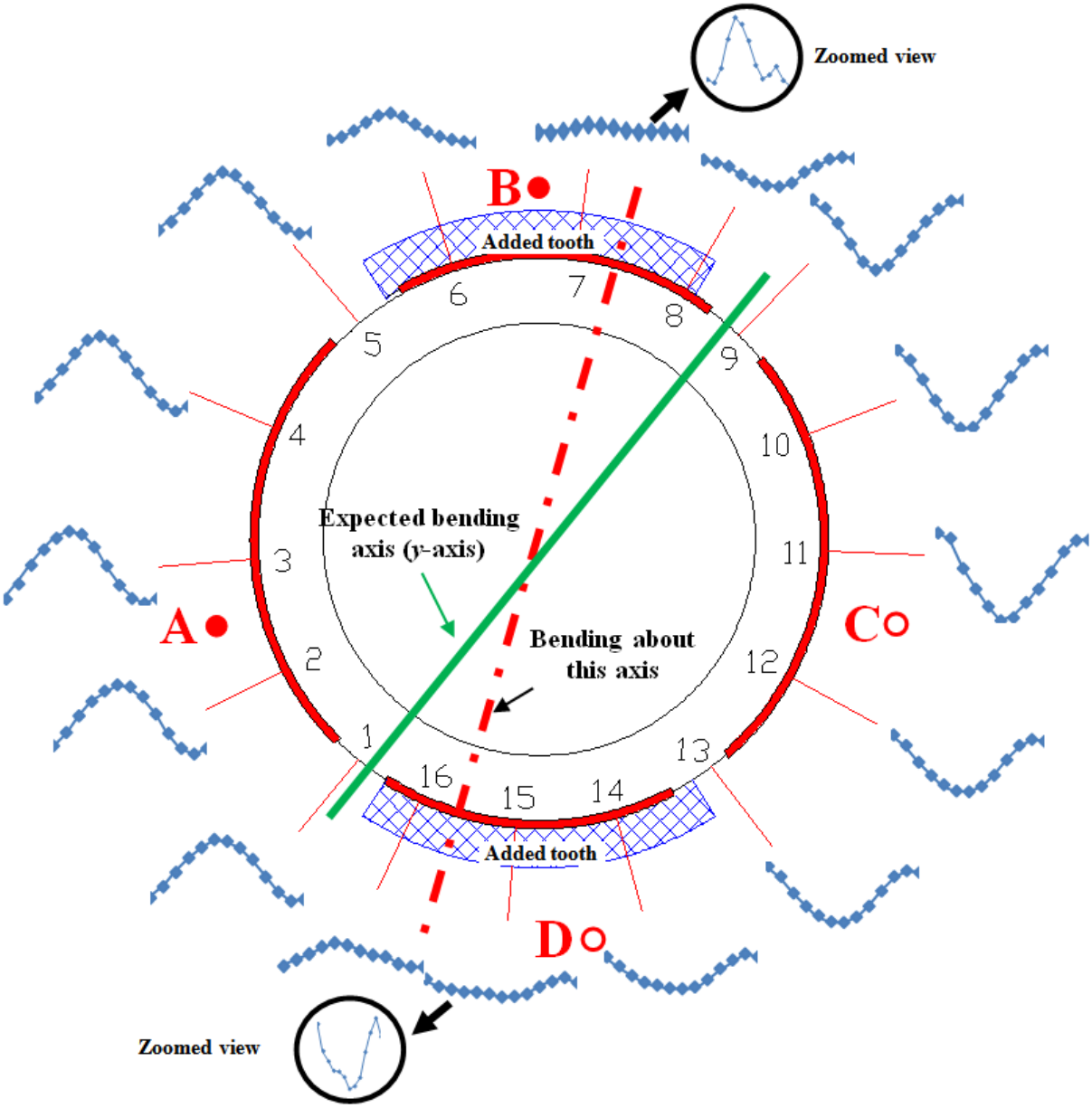

Figure 4.10 - Metal teeth motor vibration waveform test with electrodes paired AB & CD [41].

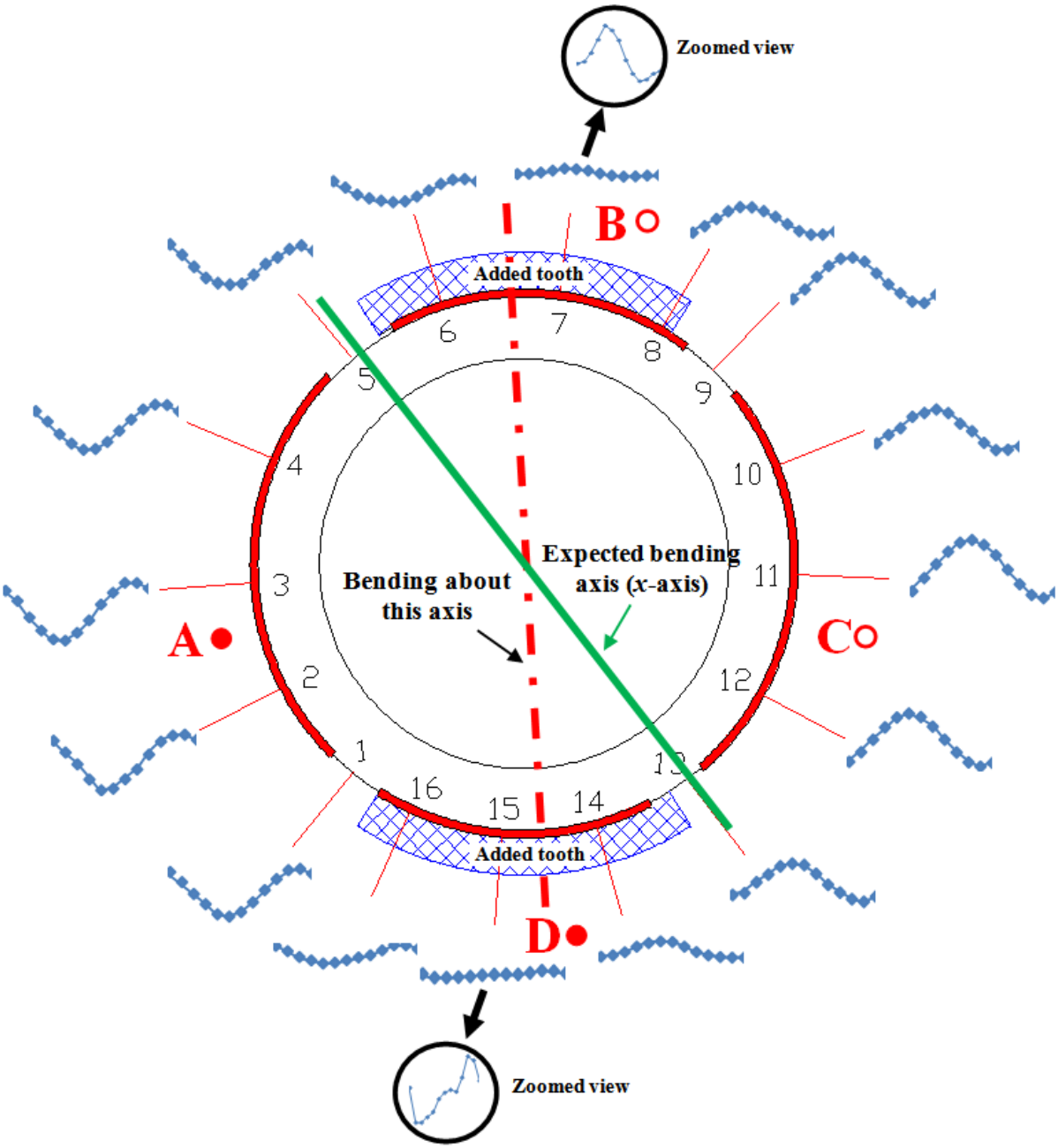

Figure 4.11 - Metal teeth motor vibration waveform test with electrodes paired AD & BC [41].

4.4 Waveform measurement of brass tube motor

The standing wave operating principle of the brass tube motor is also verified with ZYGO profiler measurements. According to the principle, the stator consisting of the brass square tube and four PZT plates would vibrate in bending mode only in the direction of the actuation. If the PZT plates in X axis are actuated with sinusoidal signal, only the faces on X axis would vibrate in sinusoidal form while the faces on Y axis would not. It would be the same on Y axis as well if they were to be actuated. As shown in Figure 4.12, three positions on each side of the PZT plates are selected for out of plane displacement measurements.

The phases of vibration for each four sides are measured on Position 2 of each PZT plates. Sinusoidal signal is applied on only the red wires to cause a bending vibration along Y axis direction only. From the results, sinusoidal phases are observed from the PZT plates on the Y axis with 180 ° differences while no vibration is observed from the PZT plates on the X axis as shown in Figure 4.13. If travelling wave is generated, the faces on X axis would show sinusoidal vibration phase. This confirms that the ultrasonic motor design vibrates in a standing wave form rather than a traveling wave form.

During the first bending vibration mode of the tube, the phase of position 1 is the same as the phase of position 3 while the phase of position 2 is shifted by 180 °. This is confirmed by ZYGO profiler measurement and the result is shown in Figure 4.14.

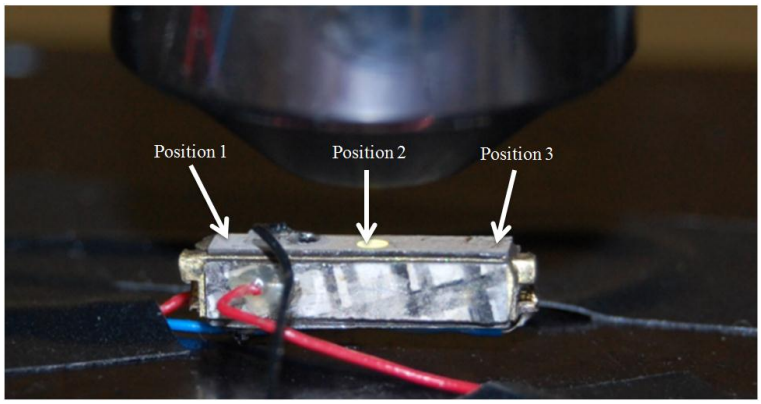

Figure 4.12 - Three positions selected on PZT plates for measurements.

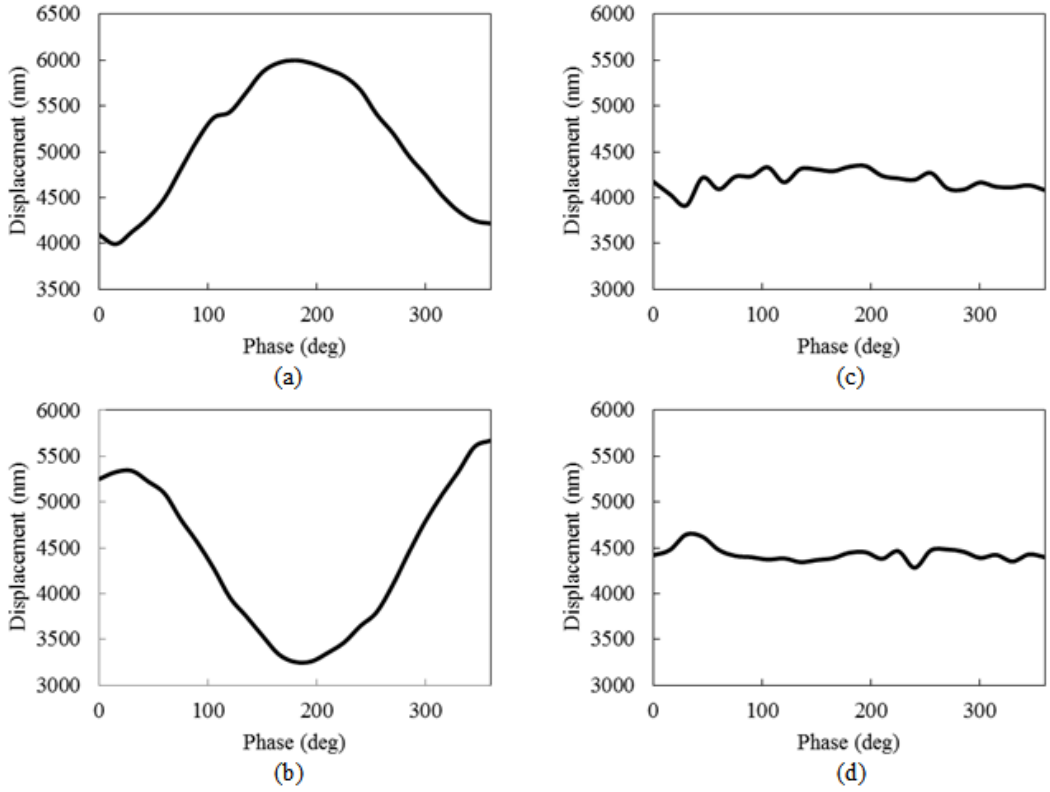

Figure 4.13 - Displacement vs. Phase along actuated direction and non-actuated direction. (a) Actuated direction side 1. (b) Actuated direction side 2. (c) Non-actuated direction side 1. (d) Non-actuated direction side 2.

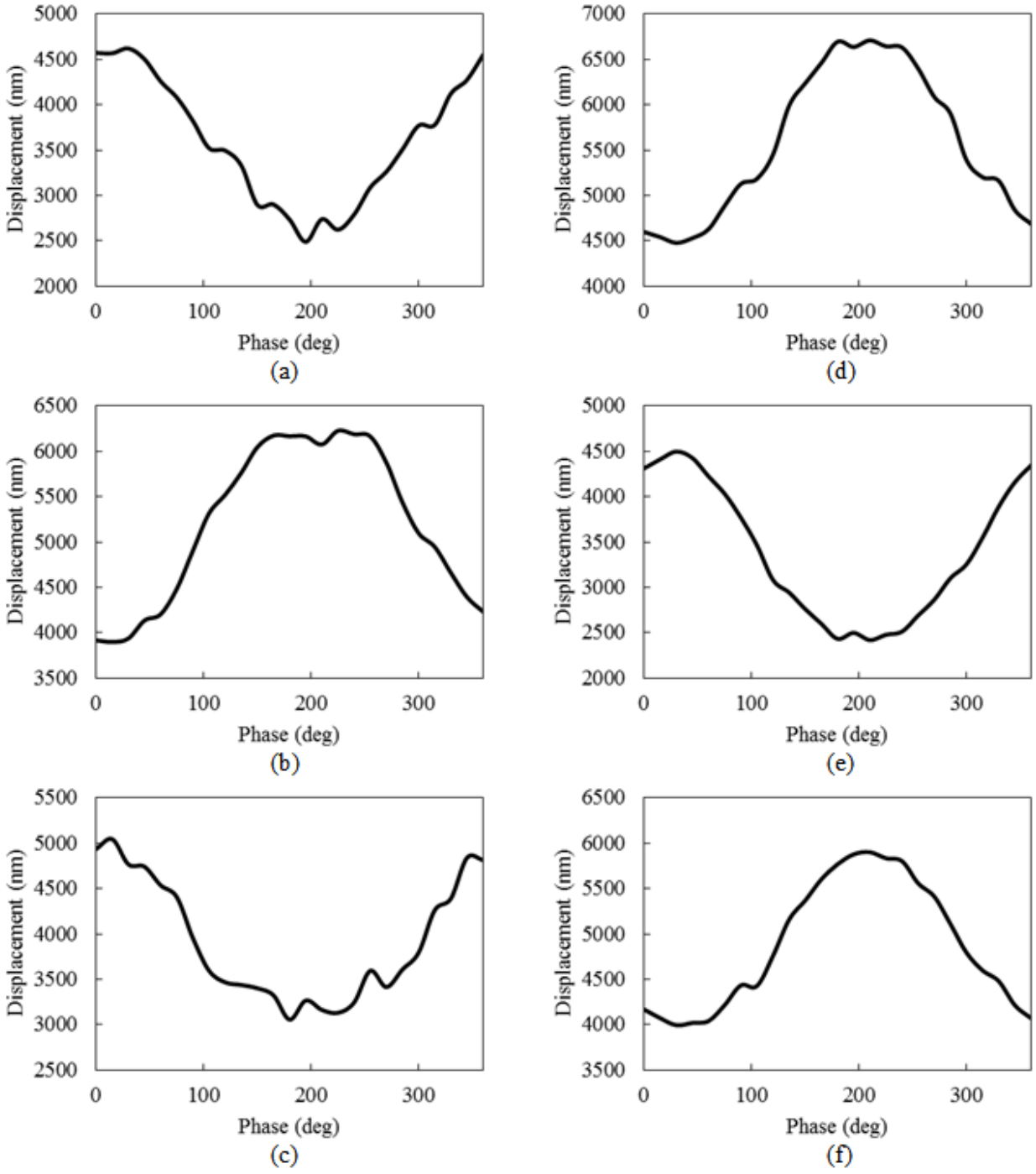

Figure 4.14 - Displacement vs. Phase at three selected positions for bending along X axis and Y axis. (a) Position 1 on X axis. (b) Position 2 on X axis. (c) Position 3 on X axis. (d) Position 1 on Y axis. (e) Position 2 on Y axis. (f) Position 3 on Y axis.

Chapter 5. Applications of ultrasonic motors

5.1 Chapter introduction

This chapter discusses the applications for the piezoelectric ultrasonic motors. There are many literatures showing examples of where the piezoelectric ultrasonic motors have already been placed in for industrial applications such as patents and commercial publications. Also, there are other literatures that introduce a concept of how the motors can be used in the future. Applications such as motors for watch or camera lens actuation have already been adapted and widely being used. Other possible applications include usage in mobile micro lens actuation, viscosity sensor, mobile car window operation, fibre optics positioning, micro robot hand actuation, or biomedical applications.

5.2 Application in watches

Iino et al. discuss the application of a self-oscillating ultrasonic motor to a watch [48]. An 8 mm diameter self-oscillating micro-motor is put on a watch for a vibration alarm. At a previously set time, the watch vibrates just as a mobile cell phone to alarm the user. Another application in a watch is using a 4.5 mm diameter ultrasonic motor for a calendar mechanism driving source. The application is shown in Figure 5.1.

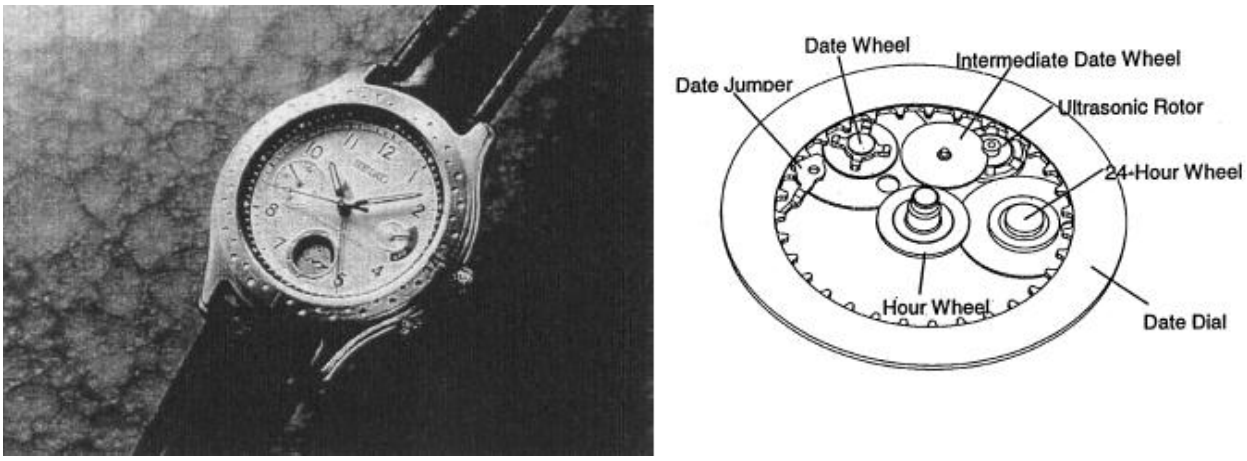

Figure 5.1 - Ultrasonic motor application in watches [48].

5.3 Application in camera lens

There are numerous patents for piezoelectric ultrasonic motors in use of camera lens movements [49 ~ 51]. Camera companies such as Canon and Nikon have adapted the piezoelectric ultrasonic motors for providing automatic focus control by providing an accurate movement to the lens barrel. Petit and Gonnard discuss the design phases of an ultrasonic motor industrialization which has led to the development of Traveling Wave Induced by Longitudinal Actuators (TWILA) structure [52]. Figure 5.2 shows the patent from Canon, Figure 5.3 shows the patent from Nikon, and Figure 5.4 shows the TWILA motor.

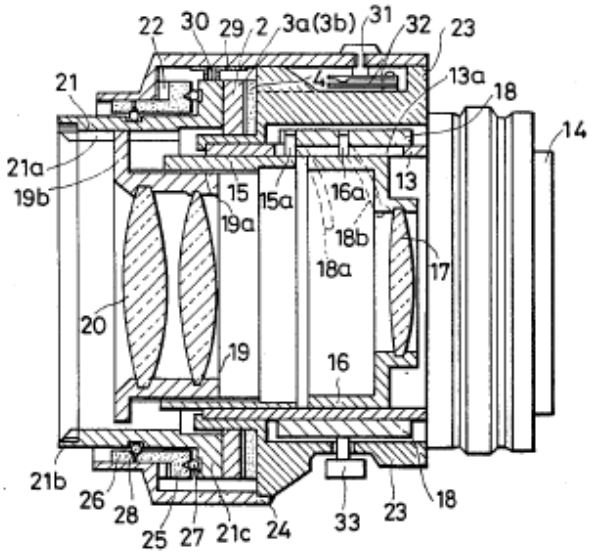

Figure 5.2 - Construction drawing of an ultrasonic motor from U.S. Patent filed by Canon [49].

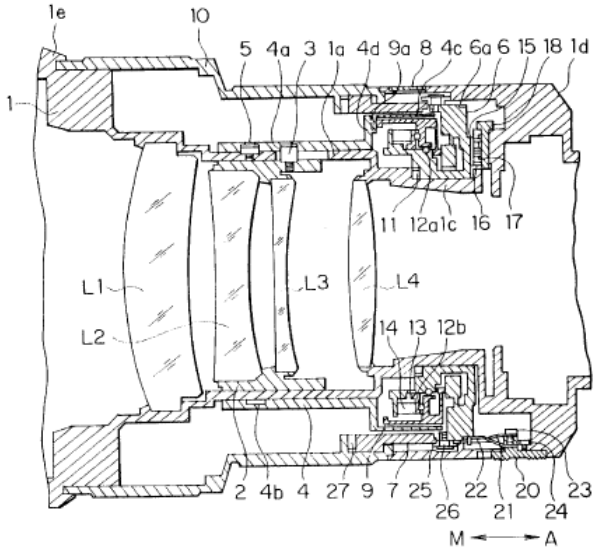

Figure 5.3 - Cross section view of the lens barrel with a built-in ultrasonic motor from U.S. Patent filed by Nikon [50].

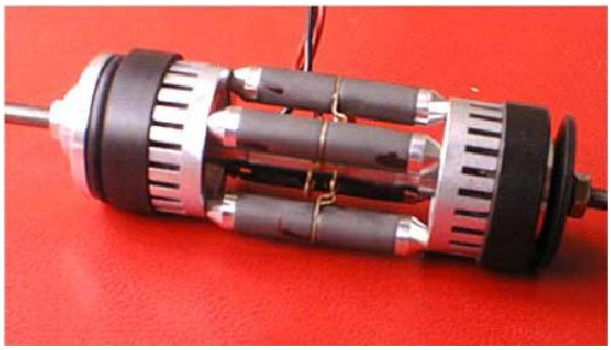

Figure 5.4 - The TWILA motor [52].

5.4 Application in mobile camera lens

New Scale Technologies, Inc. has developed a linear ultrasonic motor called SQUIGGLE motor [53, 54]. This motor uses a rectangular tube motor with four pieces of PZT plates which are actuated with two sources of sinusoidal signals with a phase difference of 90 ° to generate a linear motion of the threaded rod. The motor can be used for a possible application for actuation of lens for mobile camera where the size of the driving mechanism is critical. Figure 5.5 shows the motor design and its application.

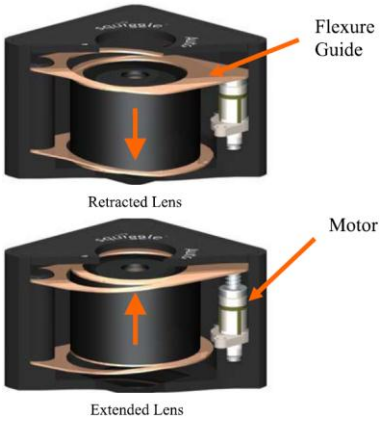

Figure 5.5 - SQUIGGLE motor for application in mobile camera lens actuation [53].

5.5 Application in mobile car window

Chen et al. report a disk type travelling wave ultrasonic motor with a high torque [55]. A 100 mm diameter prototype is designed which enables a close contact between the rotor and the stator with pre-pressure in order to reduce the relative vibration between the rotor and the stator. This enables the motor to generate a high torque of greater than 4 Nm when the pre pressure of 400 N is applied with an applied voltage of 370 V at a frequency of 25 kHz. This high torque motor meets the requirement of lifting a car window. The configuration of the travelling wave motor is shown in Figure 5.6.

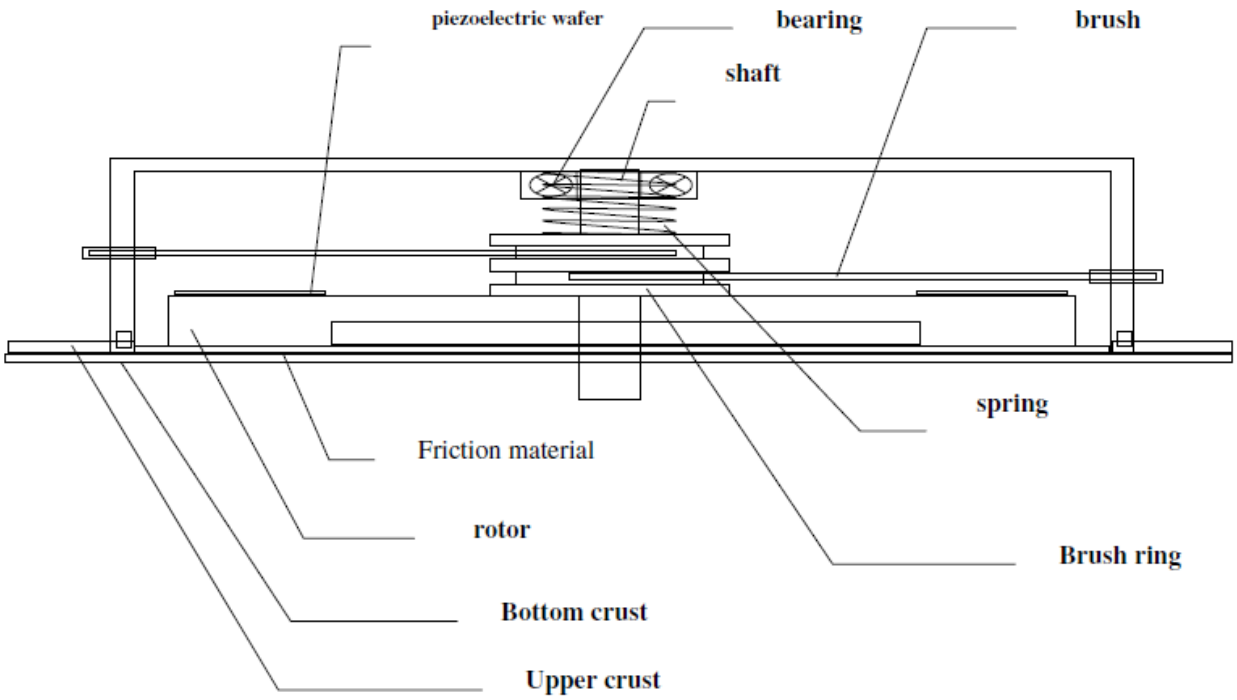

Figure 5.6 - High torque motor design by Chen [55].

5.6 Application in viscosity sensor

Thalhammer et al. report a quartz crystal sensor which is used for measuring the density-viscosity product of Newtonian liquids consisting of shear mode piezoelectric resonator [56]. Two plano-convex AT-cut quartz crystals vibrate in a thickness-shear mode with the measuring liquid sample in between. The disturbing resonance in the liquid layer is suppressed in this setup. The resonator is shown in Figure 5.7.

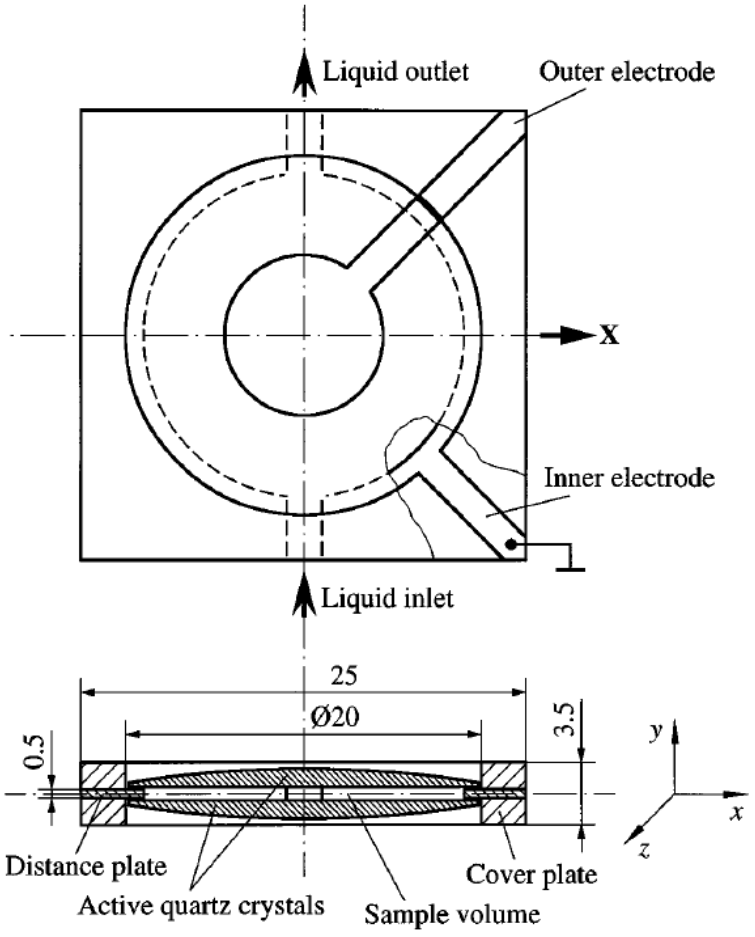

Figure 5.7 - Viscosity sensor using shear mode piezoelectric resonator [56].

5.6 Application in fibre optics positioning

Fisher et al. report a Wide-Field Multi Object Spectrometer using an array of 2400 Cobra optic fiber positioners made of piezoelectric actuators [57]. The optical fiber positioner Cobra is a two degree-of-freedom actuator that can position the optical fiber to a precision of 5 um. A tube type rotary piezoelectric motor with a travelling wave actuated is used for Cobra model. Benefits or using piezoelectric actuators are excellent responsiveness and high electrical to mechanical energy conversion efficiency. Cobra positioner is shown in Figure 5.8.

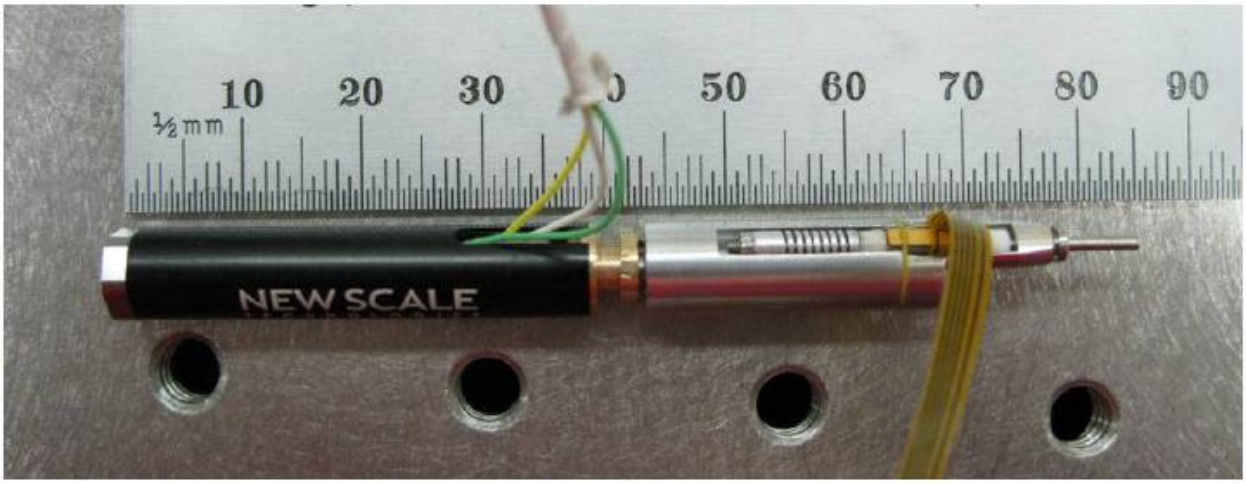

Figure 5.8 - Cobra positioner using piezoelectric motor [57].

5.7 Application in micro robot hand actuation

Morita et al. report a piezoelectric motor application in a micro-hand of a robot [58]. A cylindrical tube type ultrasonic motor with travelling wave excitation mode is fabricated with an outer diameter of 2.4 mm, inner diameter of 1.4 mm, and length of 10 mm. Two sinusoidal signals with a phase difference of 90 ° are applied to the outer electrodes of the tube which are

divided into four segments for exciting a travelling wave on the surface. A driving frequency of 85 kHz with amplitude of 100 V is applied to the motor which performs at a no-load speed of 650 RPM and a maximum torque of 0.22 mNm. Two motor units are constructed for two axes micro-hand robot. Using the two motors, a weight of 10 g load could be driven. The robot assembly is shown in Figure 5.9.

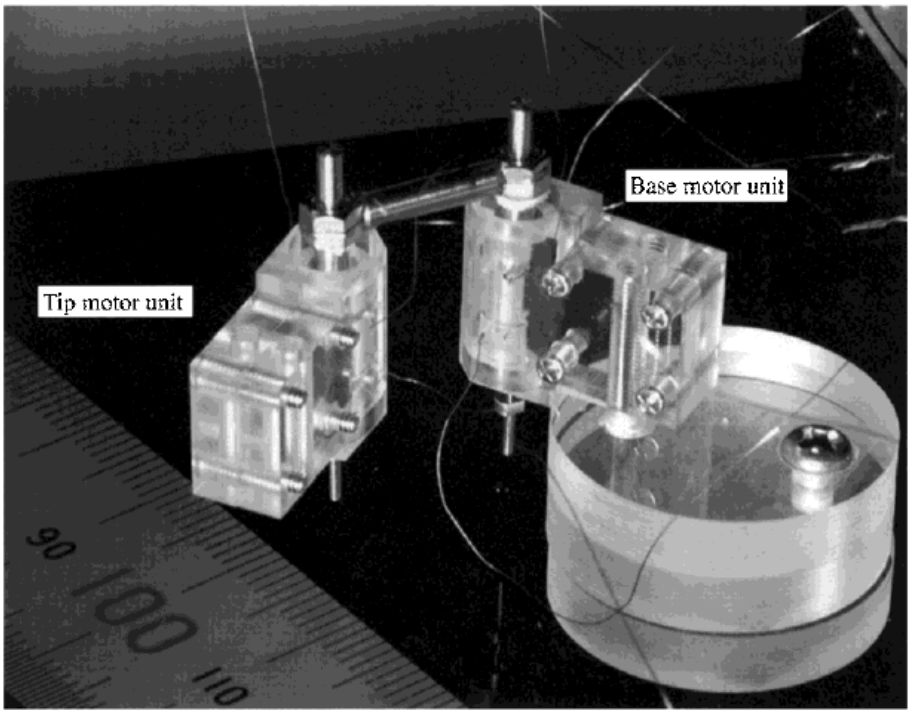

Figure 5.9 - Micro-hand robot using two piezoelectric motors [58].

5.8 Application in biomedical application

There are numerous literatures on applications of piezoelectric ultrasonic motors in biomedical applications [59, 60]. Features of ultrasonic motors such as larger output torque, larger output power density, smaller size, faster response time, higher positioning accuracy, no electromagnetic interference, higher self-holding force compared to electromagnetic motor make

ultrasonic motors more suitable for biomedical applications. Tieying et al. report a 1 mm diameter cylindrical rod type ultrasonic motor development and its application in endoscopic OCT. [59] At a resonant frequency of 32 kHz with amplitude of 350 V, the motor has a no-load speed of 1800 RPM and a stall torque of 4 μNm. The motor application in endoscopic OCT is shown in Figure 5.10. Allen et al. report a miniature ultrasonic piezoelectric motor development and its application in minimally invasive cardiac therapy [60]. SQUIGGLE motor from New Scale Technologies, which is a small size linear motor with a dimension of 7.0 mm x 3.4 mm x 3.4 mm, is used for the application. The HeartLander ONMI model which uses two ultrasonic piezoelectric motors is shown in Figure 5.11.

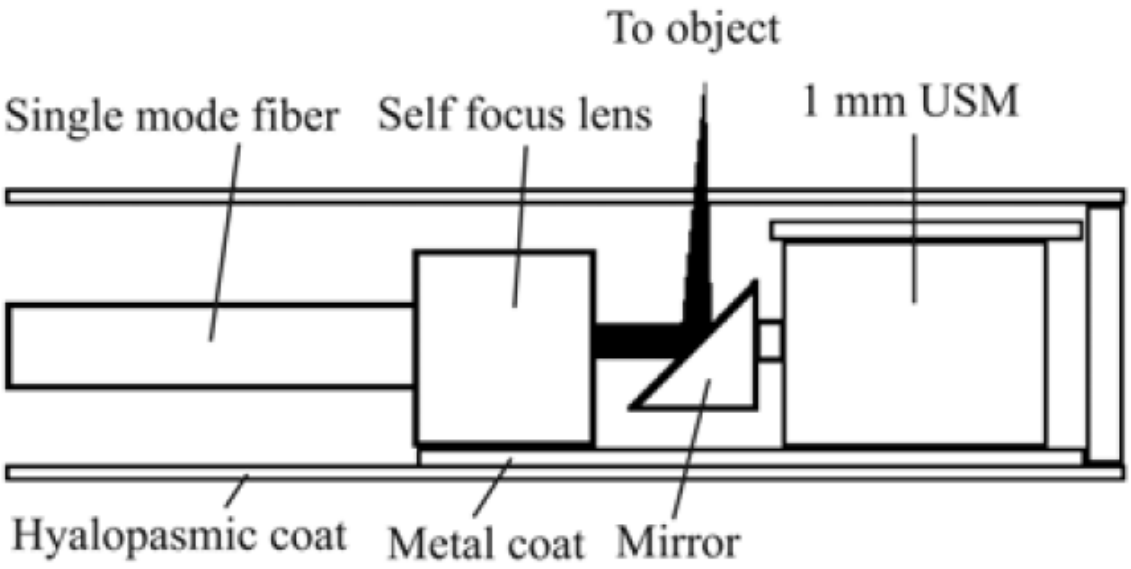

Figure 5.10 - Endoscopic OCT application of piezoelectric ultrasonic motor [59].

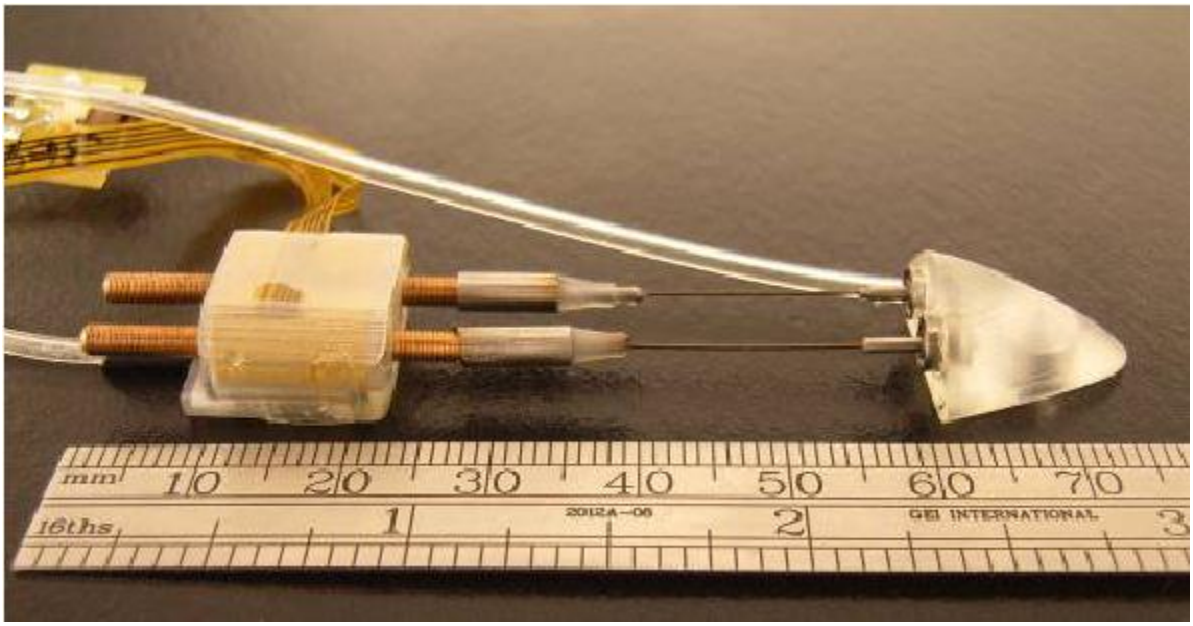

Figure 5.11 - HeartLander OMNI design using two piezoelectric ultrasonic motors [60].

Chapter 6. Summary

6.1 Conclusions

The objective of this thesis is to design and fabricate novel single vibration mode standing wave tubular piezoelectric ultrasonic motor. The background information and history of piezoelectric ultrasonic motors are introduced with literature reviews on different types of motors reported. Three designs of the piezoelectric ultrasonic motors are fabricated into prototypes. Two prototypes are fabricated as a result of the first iteration of the prototyping using PZT cylindrical tubes as stator structure. One prototype is the PZT teeth motor prototype which is designed with PZT teeth by cutting notches on both ends of the cylindrical PZT tube. The PZT teeth motor performs at a no-load speed of 486 RPM and a maximum torque of 296.0 μNm. Another prototype is the metal teeth motor prototype which is designed with added metal teeth by attaching four pieces of brass teeth on both ends of the cylindrical PZT tube. The metal teeth motor performs at a no-load speed of 420 RPM and a maximum torque of 296.0 μNm. From the second iteration of prototyping, brass tube motor which is an improved design of piezoelectric ultrasonic motor using a rectangular brass tube with four pieces of PZT plates attached on each side is fabricated. The brass tube motor performs at a no-load speed of 1042 RPM and a maximum torque of 317.1 μNm. A novel method of identifying waveform generated on the stator tube is introduced. The standing wave principle of operation is verified with the waveform measured from the ZYGO optical profiler. Reported applications where piezoelectric ultrasonic motors can be used are introduced.

6.2 Contributions

The author's contributions are the followings

- Develop a novel standing wave type tubular piezoelectric ultrasonic motor driven with a single source of sinusoidal signal and a single vibration in bending mode
- A single source of sinusoidal signal driven therefore the direction of applied signal determines the rotation direction
- A single vibration in bending mode driven therefore the vibration mode coupling is not required
- Three prototypes are designed, simulated, fabricated and tested
- PZT teeth motor prototype is fabricated with PZT cylindrical tube with notches cut from the PZT tube
- Metal teeth motor prototype is fabricated with PZT cylindrical tube metal teeth added to the outer surface of the PZT tube
- Brass tube motor prototype is fabricated with brass rectangular tube with PZT pieces bonded and brass notches for the teeth
- A novel method of measuring waveforms for both standing wave and travelling wave on piezoelectric tube using ZYGO 3D optical profiler introduced

6.2 Future works

Further improvements can be made on the design of the motor. The overall size of the motor design can be smaller since the smallest motor design reported is using a 1 mm stator diameter. Teeth and rotor design can be optimized to further increase the speed and torque of the

motor by stabilizing contact between the rotor and the stator and also by increasing the contacted area.

More work is required for the study of durability of the motor. Since the piezoelectric motor is driven by frictional force, the wear of the teeth or the rotor can have a significant impact on the performance of the motor. A cooling method should be introduced as high voltage applied to the PZT can increase the temperature which may have degrading effect on piezoelectric properties.

A converting mechanism can be worked on for converting a rotary motion to a linear motion. This will increase the number of applications where the piezoelectric ultrasonic motor can be used.

References

[1] A. Arnau, Piezoelectric transducers and applications, Springer, New York, 2008.

[2] An Introduction to Piezoelectric Transducer Crystals, http://www.bostonpiezooptics.com/?D=6. Accessed July 23, 2011.

[3] Piezo-University Fundamentals of Piezoelectricity, http://www.physikinstrumente.com/en/products/prdetail.php?sortnr=400600.00 Accessed July 23, 2011

[4] S. Yener, Design and characterization of piezoelectric ultrasonic motors, A Thesis in Materials for Doctor of Philosophy, The Pennsylvania State University, 2004.

[5] T. Sashida, T. Kenjo, Introduction to Ultrasonic motors, Oxford University Press, New York, 1993.

[6] W. Williams, W. J. Brown, Piezoelectric Motor, U.S. Patent 2439499, 1948.

[7] V. Snitka, V. Mizariene, D. Zukauskas, The status of ultrasonic motors in the former Soviet Union, Ultrasonics 34 (1996) 247 – 250.

[8] S. Ueha, Y. Tomikawa, Ultrasonic Motors, Oxford University Press, New York, 1993.

[9] K. Uchino, Piezoelectric ultrasonic motors: overview, Smart Master. Struct. 7 (1998) 273 – 285.

[10] K. Uchino, S. Cagatay, B. Koc, S. Dong, P. Bouchilloux, M. Strauss, Micro piezoelectric ultrasonic motors, Journal of Electroceramics 13 (2004) 393 – 401.

[11] S. Ueha, M. K. Kurosawa, Ultrasonic otors, in: Proceedings of Ultrasonics Symposium, Chicago, IL , USA, 1988, pp. 519 – 522.

[12] S. Ueha, Present status of ultrasonic motors, in: Proceedings of Ultrasonics Symposium, Montreal, Que., Canada, 1989, pp. 749 – 753.

[13] T. Morita, Miniature piezoelectric motors, Sens. Actuators A 103 (2003) 291–300.

[14] T. Takano, Y. Tomikawa, C. Kusakabe, Same phase drive-type ultrasonic motors using two degenerate bending vibration modes of a disk, IEEE Trans. Ultrason. Ferroelectr. Freq. Control 39 (1992) 180 – 186.

[15] T. Takano, Y. Tomikawa, M. Aoyagi, C. Kusakabe, Piezoelectric actuators driven by the saw-tooth-like motion of a stator, Ultrasonics 34 (1996) 279 – 282.

[16] K. Nakamura, M. K. Kurosawa, S. Ueha, Characteristics of a hybrid transducer-type ultrasonic motor, IEEE Trans. Ultrason. Ferroelectr. Freq. Control 38 (1991) 188 – 193.

[17] R. Carotenuto, G. Caliano, A. Iula, M. Pappalardo, Langevin flexural piezoelectric motor based on stator precessional motion, Sens. Actuators A 113 (2004) 189 – 197.

[18] S. Jun, S. Lee, S. Lee, H, Kim, K. Lee, Piezoelectric linear motor with unimorph structure by co-extrusion process, Sens. Actuators A 147 (2008) 300 – 303.

[19] M. K. Kurosawa, S. Ueha, Single-phase drive of a circular ultrasonic motor, J. AcoustS. Soc. Am. 90 (1991) 1723 – 1728.

[20] B. Zhai, S. Lim, K. Lee, A design of an ultrasonic linear motor based on theoretical analysis, Smart Mater. Struct.9 (2000) 774 – 779.

[21] M. Fleischer, D. Stein, H Meixner, Ultrasonic piezomotor with longitudinally oscillating amplitude-transforming resonator, IEEE Trans. Ultrason. Ferroelectr. Freq. Control 36 (1989) 607 – 613.

[22] L. Petit, R. Briot, L. Lebrun, P. Gonnard, A piezomotor using longitudinal actuators, IEEE Trans. Ultrason. Ferroelectr. Freq. Control 45 (1998) 277 – 284.

[23] K. Yao, B. Koc, K. Uchino, Longitudinal-bending mode micromotor using multilayer piezoelectric actuator, IEEE Trans. Ultrason. Ferroelectr. Freq. Control 48 (2001) 1066 – 1071.

[24] K. Nakamura, M. K. Kurosawa, S. Ueha, Design of a hybrid transducer type ultrasonic motor, IEEE Trans. Ultrason. Ferroelectr. Freq. Control 40 (1993) 395 – 401.

[25] Y. Liu, W. Chen, J. Liu, S. Shi, A cylindrical standing wave ultrasonic motor using bending vibration transducer, Ultrasonics 51 (2011) 527 – 531.

[26] M. Aoyagi, T. Suzuki, Y. Tomikawa, Characteristics of a bolt-clamped torsional vibrator using shear-mode piezo-ceramics sandwiched in the axial direction, Ultrasonics 34 (1996) 219 – 222.

[27] A. E. Glazounov, Q. M. Zhang, C. Kim, Torsional actuator based on mechanically amplified shear piezoelectric response, Sens. Actuators A 79 (2009) 22 – 30.

[28] R. Briot, M. Guillemot-Amadei, A. Pelourson, C. Garabedian, Generators for piezoelectric motors, Meas. Sci. Technol. 4 (1993) 938 – 946.

[29] J. Tsujino, M. Takeuchi, H. Koshisako, Ultrasonic rotary motor using a longitudinal-torsional vibration converter, in: Proceedings of Ultrasonics Symposium, Tucson, AZ, USA, 1992, 887 – 892.

[30] O. Ohnishi, O. Myohga, T. Uchikawa, M. Tamegai, T. Inoue, S. Takahashi, Piezoelectric ultrasonic motor using longitudinal-torsional composite resonance vibration, IEEE Trans. Ultrason. Ferroelectr. Freq. Control 40 (1993) 687 – 693.

[31] N. Hagood IV, A. McFarland, Modeling of a piezoelectric rotary ultrasonic motor, IEEE Trans. Ultrason. Ferroelectr. Freq. Control 42 (1995) 210 – 224.

[32] S. Dong, S. Lim, K. Lee, J. Zhang, L. Lim, K. Uchino, Piezoelectric ultrasonic micromotor with 1.5 mm diameter, IEEE Trans. Ultrason. Ferroelectr. Freq. Control 50 (2003) 361–367.

[33] H. Zhang, S. Dong, S. Zhang, T. Wang, Z. Zhang, L. Fan, Ultrasonic micro-motor using miniature piezoelectric tube with diameter of 1.0 mm, Ultrasonics 44 (2006) 603–606.

[34] C. Yin, T. Yu, An ultrasonic motor driven by traveling cylindrical wedge waves, in: Proceedings of IEEE Ultrasonics Symposium, Vancouver, BC, Canada, 2006, pp. 156–159.

[35] T. Morita, M.K. Kurosawa, T. Higuchi, An ultrasonic micromotor using a bending vibration transducer based on PZT thin film, Sens. Actuators A 50 (1995) 75–80.

[36] T. Morita, M.K. Kurosawa, T. Higuchi, A cylindrical micro ultrasonic motor using PZT thin film deposited by single process hydrothermal method (diameter 2.4mm, L10 mm stator transducer), IEEE Trans. Ultrason. Ferroelectr. Freq. Control 45 (1998) 1178 – 1187.

[37] B. Koc, S. Cagatay, K. Uchino, A piezoelectric motor using two orthogonal bending modes of a hollow cylinder, IEEE Trans. Ultrason. Ferroelectr. Freq. Control. 49 (2002) 495–500.

[38] S. Dong, S. Cagatay, K. Uchino, D. Viehland, A 'Center-wobbling' ultrasonic rotary motor using a metal tube-piezoelectric plate composite stator, J. Intell. Mater. Syst. Struct. (2002) 749–755.

[39] S. Cagatay, B. Koc, K. Uchino, A 1.6-mm, metal tube ultrasonic motor, IEEE Trans. Ultrason. Ferroelectr. Freq. Control. 50 (2003) 782–286.

[40] H. Zhu, L. Luo, C. Chen, C. Zhao, Modeling of a cylindrical ultrasonic motor based on the single crystals, J. Electroceram (2008) 243 – 249.

[41] S. He. P. Chiarot, S. Park, A single vibration mode tubular piezoelectric ultrasonic motor, IEEE Trans. Ultrason. Ferroelectr. Freq. Control 58 (2011) 1049–1061.

[42] O. Zharii, Modeling of a mode conversion ultrasonic motor in the regime of slip, IEEE Trans. Ultrason. Ferroelectr. Freq. Control 40 (1993) 411 – 417.

[43] K. Spanner, Survey of the various operating principles of ultrasonic piezomotors, in: Proceedings of Actuators 2006, Bremen, Germany, 2006, pp. 1–8.

[44] S. He, W. Chen, X. Tao, Z. Chen, Standing wave bi-directional linearly moving ultrasonic motor, IEEE Trans. Ultrason. Ferroelectr. Freq. Control 45 (1998) 1133–1139.

[45] Y. Ma, Z. Feng, C. Pan, F. Kong, Static and dynamic analysis of a four-tube piezoelectric actuator, Rev. Sci. Instrum. 80 (2009) 065101-1 – 065101-10.

[46] S. Yang, W. Huang, Three-dimensional displacements of a piezoelectric tube scanner, Rev. Sci. Instrum. 69 (1998) 226 – 229.

[47] P. Lu, K. Lee, S. Lim, W. Lin, A kinematic analysis of cylindrical ultrasonic micromotors, Sens. Actuators A 87 (2001) 194 – 197.

[48] A. Iino, K. Suzuki, M. Kasuga, M. Suzuki, T. Yamanaka, Development of a self-oscillating ultrasonic micro-motor and its application to a watch, Ultrasonics 38 (2000) 54-59.

[49] M. Katsuma, H. Murakami, A. Hiramatsu, Drive system for a vibration wave motor for lens control, U.S. Patent 4560263, 1985.

[50] K. Fukino, Lens barrel with built-in ultrasonic motor, U.S. Patent 5898528, 1999.

[51] K. Yoshibe, I. Soshi, Lens barrel comprising an ultrasonic motor, U.S. Patent 5898526, 1999.

[52] L. Petit, P. Gonnard, Industrial design of a centimetric "TWILA" ultrasonic motor, Sens. Actuators A 120 (2005) 211–224.

[53] D. Henderson, Simple ceramic motor… inspiring smaller products, in: Proceedings of Actuators, Bremen, Germany, 2006, pp. 1–4.

[54] B. Kennedy, Power packed piezoelectric motors: big power, small package, MICROmanufacturing (2008) 23 – 26.

[55] Y. Chen, Q. Lie, T. Zhou, A traveling wave ultrasonic motor of high torque, Ultrasonics 44 (2006) 581–584.

[56] R. Thalhammer, S. Braun, B. Devic-Kuhar, M. Grőschl, F. Trampler, E. Benes, H. Nowotny, M. Kostal, Viscosity sensor utilizing a piezoelectric thickness shear sandwich resonator, IEEE Trans. Ultrason. Ferroelectr. Freq. Control 45 (1998) 1331 – 1340.

[57] C. Fisher, D. Braun, J. Kaluzny, T. Haran, Cobra—A two degree of freedom fiber optic positioning mechanism, in: Proceedings of IEEE Aerospace Conference, Big Sky, MT, USA, 2009, pp. 1–11.

[58] T. Morita, M. K. Kurosawa, T. Higuchi, Cylindrical micro ultrasonic motor utilizing bulk lead zirconate titanate (PZT), Jpn. J. Appl. Phys. 38 (1999) 3347 – 3350.

[59] Z. Tieying, Z. Kai, C. Yu, W. Huan, W. Jigang, J. Kaili, X. Ping, A cylindrical rod ultrasonic motor with 1 mm diameter and its application in endoscopic OCT, Chinese Science Bulletin 50 (2005) 826 – 830.

[60] P. Allen, N. Patronik, M. Zenati, C. Riviere, A mobile robot driven by miniature onboard motors for cardiac intervention, in: Proceedings of 34th Annual Northeast Bioengineering Conference, Troy, NY, USA, 2009, pp. 9-10.